Fall 1-31-2004

Multi-spectral light interaction modeling and imaging of skin lesions

Sachin Vidyanand Patwardhan
New Jersey Institute of Technology

ABSTRACT

MULTI-SPECTRAL LIGHT INTERACTION MODELING AND IMAGING OF SKIN LESIONS

by
Sachin Vidyanand Patwardhan

Nevoscope as a diagnostic tool for melanoma was evaluated using a white light source with promising results. Information about the lesion depth and its structure will further improve the sensitivity and specificity of melanoma diagnosis. Wavelength-dependent variable penetration power of monochromatic light in the trans-illumination imaging using the Nevoscope can be used to obtain this information. Optimal selection of wavelengths for multi-spectral imaging requires light-tissue interaction modeling. For this, three-dimensional wavelength dependent voxel-based models of skin lesions with different depths are proposed. A Monte Carlo simulation algorithm (MCSVL) is developed in MATLAB and the tissue models are simulated using the Nevoscope optical geometry. 350-700nm optical wavelengths with an interval of 5nm are used in the study. A correlation analysis between the lesion depth and the diffuse reflectance is then used to obtain wavelengths that will produce diffuse reflectance suitable for imaging and give information related to the nevus depth and structure. Using the selected wavelengths, multi-spectral trans-illumination images of the skin lesions are collected and analyzed.

An adaptive wavelet transform based tree-structure classification method (ADWAT) is proposed to classify epi-illuminance images of the skin lesions obtained using a white light source into melanoma and dysplastic nevus images classes. In this method, tree-structure models of melanoma and dysplastic nevus are developed and semantically compared with the tree-structure of the unknown image for classification.

Development of the tree-structure is dependent on threshold selections obtained from a statistical analysis of the feature set. This makes the classification method adaptive. The true positive value obtained for this classifier is 90% with a false positive of 10%. The Extended ADWAT method and Fuzzy Membership Functions method using combined features from the epi-illuminance and multi-spectral images further improve the sensitivity and specificity of melanoma diagnosis. The combined feature set with the Extended-ADWAT method gives a true positive of 93.33% with a false positive of 8.88%. The Gaussian Membership Functions give a true positive of 100% with a false positive of 17.77% while the Bell Membership Functions give a true positive of 100% with a false positive of 4.44%.

MULTI-SPECTRAL LIGHT INTERACTION MODELING AND IMAGING OF SKIN LESIONS

by
Sachin Vidyanand Patwardhan

A Dissertation
Submitted to the Faculty of
New Jersey Institute of Technology
In Partial Fulfillment of the Requirements for the Degree of
Doctor of Philosophy in Electrical Engineering

Department of Electrical and Computer Engineering

January 2004

APPROVAL PAGE

MULTI-SPECTRAL LIGHT INTERACTION MODELING AND IMAGING OF SKIN LESIONS

Sachin Vidyanand Patwardhan

Dr. Atam P. Dhawan, Dissertation Advisor Professor of Electrical and Computer Engineering, NJIT	Date
Dr. Nirwan Ansari, Committee Member Professor of Electrical and Computer Engineering, NJIT	Date
Dr. Timothy Chang, Committee Member Associate Professor of Electrical and Computer Engineering, NJIT	Date
Dr. John F. Federici, Committee Member Professor of Physics, NJIT	Date
Dr. Stanley Reisman, Committee Member Professor of Biomedical Engineering, NJIT	Date

BIOGRAPHICAL SKETCH

Author: Sachin Vidyanand Patwardhan

Degree: Doctor of Philosophy

Date: January 2004

Undergraduate and Graduate Education:

- Doctor of Philosophy in Electrical Engineering
  New Jersey Institute of Technology, Newark, NJ, 2004.
- Master of Technology in Biomedical Engineering
  Indian Institute of Technology, Mumbai, India, 1993.
- Bachelor of Engineering in Electrical Engineering
  Government College of Engineering, Pune, India, 1990.

Major: Electrical Engineering

Presentations and Publications:

Sachin V. Patwardhan, Atam P. Dhawan and Patricia A. Relue, Tree-structured Wavelet Transform Signature for Classification of Melanoma, Proc. SPIE Medical Imaging: Image Processing, Vol. 4684, p. 1085-1091, 2002.

Amit Nimunkar, Atam P. Dhawan, Patricia A. Relue and Sachin V. Patwardhan, Wavelet and Statistical Analysis for Melanoma Classification, Proc. SPIE Medical Imaging: Image Processing, Vol. 4684, p. 1346-1353, 2002.

Sachin V. Patwardhan, Atam P. Dhawan and Patricia A. Relue, Classification of Melanoma Using Tree-Structured Wavelet Transforms, Computer Methods and Programs in Biomedicine, Vol. 72, p. 223-239, 2003.

Sachin V. Patwardhan, Atam P. Dhawan and Patricia A. Relue, Wavelength Selection for Multi-Spectral Imaging of Skin Lesions, Proc. IEEE 29th Annual Northeast Bioengineering Conference, p. 327-328, 2003.

Sachin V. Patwardhan, Atam P. Dhawan and Patricia A. Relue, Monte Carlo Simulation of Light-Tissue Interaction – Part I: Three-Dimensional Voxel Based Simulation for Optical Imaging, IEEE Transactions on Biomedical Engineering, under revision, 2003.

Sachin V. Patwardhan, Atam P. Dhawan and Patricia A. Relue, Monte Carlo Simulation of Light-Tissue Interaction – Part II: Three-Dimensional Simulation for Trans-illumination based Imaging of Skin Lesions, IEEE Transactions on Biomedical Engineering, under revision, 2003.

Atam P. Dhawan, Sachin V. Patwardhan and Patricia A. Relue, Multi-Spectral Light Tissue Interaction Modeling For Skin Lesion Imaging, 25th Annual International Conference of the IEEE Engineering in Medicine and Biology Society, submitted, 2003.

Ketan Patel, Ronn Walvick, Sachin V. Patwardhan and Atam P. Dhawan, Classification of Melanoma using Wavelet Transform-based Optimal Fearure Set, SPIE International Symposium: Medical Imaging, submitted, 2004.

Sachin V. Patwardhan, Shuangshuang Dai and Atam P. Dhawan, Multi-spectral Image Analysis and Classification of Melanoma Using Crisp and Fuzzy Partitions, Computerized Medical Imaging and Graphics, submitted, 2003

IN THE MEMORIES OF MY GRANDFATHERS

VINAYAK D. PATWARDHAN AND CHANTIMANI P. DAMLE

WHOSE BLESSINGS WILL ALWAYS GIVE ME STRENGTH

AND SHOW ME THE RIGHT PATH

ACKNOWLEDGEMENT

It is with great pleasure; I express my indebtness and gratitude to Dr. Atam P. Dhawan for his guidance, suggestions and supervision of my dissertation work. Without his support, encouragement and reassurance completion of this work was not possible. I am also thankful to Dr. Patricia A. Relue for her advice and suggestions as my unofficial co-advisor. Special thanks are also given to Dr. Stanley Reisman, Dr. Nirwan Ansari and Dr. Timothy Chang and Dr. John Federici for actively participating in my committee.

I would like to thank the Whitaker Foundation for providing partial funding for this research under the Whitaker Foundation Research Grant RG-99-0127 and to all the patients whose data was used in this study, The Medical College of Ohio, Toledo and Dr. Prabir Chaudhari for his contribution in the data collection. I am also thankful H. Zeng, C. MacAulay, B. Palcic and D. McLean for sharing their data of diffuse reflectance measurements using the spectroanalyser system.

Many of my fellow graduate students and friends in the Signal and Image Processing Laboratory deserve recognition for their support and valuable inputs. Thanks are given to Shuangshuang, Amit, Denver, Yash, and Kristin.

I would like to thank my parents Vidyanand and Vinita and my wife's parents Jayant and Jyoti for supporting and encouraging me during my Ph.D. work. This work was possible only because my wife Swati encouraged me to pursue my dreams and took care of our daughter Sneha and me while I was busy with my studies and research work. Special thanks are due to Swati and Sneha for being supportive and understanding and bearing the hardship of student life with me.

TABLE OF CONTENTS

TABLE OF CONTENTS
(Continued)

LIST OF TABLES

LIST OF FIGURES

CHAPTER 1

INTRODUCTION

1.1 Motivation

The rising rate of skin cancer is a growing concern worldwide [1]. Skin cancer is the most common form of cancer in the human population [2]. Mass screening for melanoma and other cutaneous malignancies has been advocated for early detection and effective treatment [3]. Dermatologists use the ABCD rule (Asymmetry, Border, Colors, and Dermoscopic structures) to characterize skin lesions [4-7]. To calculate the ABCD score, the criteria are assessed semi-quantitatively. Each of the criteria is then multiplied by a given weight factor to yield a total dermoscopy score [8]. The ABCD rule works well with thin melanocytic lesions. The sensitivity of the ABCD rule is reported to vary from 59% to 88% [9-10]. The features used in the ABCD rule suggest that changes in the surface characteristics of the nevus occur as it progresses towards melanoma. In the early stages of melanoma the features used in visual examination are hardly visible and may lead to a false diagnosis. However, if images of skin lesions can be collected that contain spatial/frequency and texture information, then a non-invasive method of lesion classification based on these surface characteristics may be developed. The lesion for biopsy can then be selected utilizing computer-aided analysis for improving the sensitivity and specificity of skin cancer detection. Thus, the development of a non-invasive imaging and analysis method could be beneficial in the early detection of cutaneous melanoma.

Malignant melanoma is the most lethal skin cancer in which melanocytes in the epidermis undergo malignant transformation. The two phases in the growth of melanoma are the superficial spreading phase, during which the lesion increases in size within the epidermis, and the vertical growth phase when the cells begin to move into the dermis [11-12]. The level of the spread of melanoma within the epidermis and then the dermis is determined as the Clark level, which indicates the stage (i.e. the severity) of the spread of melanoma. The best prognostic factor is the vertical thickness of the suspected nevus [12-13]. But due to lack of non-invasive diagnostic techniques, excision and histological sectioning of the suspected nevus is the only method used for the vertical thickness measurement. Lesion excision could be painful and people with a false diagnosis unnecessarily suffer and get a scar in place of the excised lesion. A non-invasive technique that can characterize the lesion depth information will increase the diagnostic sensitivity and also save the patients from pain and unnecessary scars.

1.2 Problem Statement and Objectives

Dhawan [14-15] introduced the concept of Nevoscope; a noninvasive trans-illumination based imaging modality for analysis and diagnosis of melanoma. The Nevoscope is being evaluated as a dermatological tool for improving visual examination of suspected lesions. It has shown promising results using image analysis techniques such as 3D reconstruction [15-16], segmentation [17-18] and texture and spatial-frequency information [14, 19-20] for quantitative analysis of diagnostic parameters.

Visible light introduced onto the skin area surrounding a lesion by the ring light source of the Nevoscope [14-15] penetrates the skin and undergoes scattering and

absorption within the various skin layers. A significant part of the unabsorbed multiply scattered light re-emerges from the skin's surface as diffuse reflectance. This reflectance forms an image of the trans-illuminated lesion when viewed from above. Although the trans-illumination images give information from within the skin, it is hard to quantify the depth from where this information is obtained. So far, Nevoscope as a diagnostic tool for melanoma was evaluated using a white light source, but it can be easily adapted to a monochromatic light source of a specific wavelength. The depth of penetration of monochromatic light in the skin depends on its wavelength, with higher wavelengths having more depth of penetration. This wavelength-dependent variable penetration power of monochromatic light in the trans-illumination imaging using the Nevoscope can be used to obtain information for characterizing the skin lesion depth.

The objectives of this study are

- To analyze the epi-illuminance images of the skin lesion, extract features and classify the images into melanoma, dysplastic nevus images classes.
- To find optical wavelengths which when used in the trans-illumination imaging of the Nevoscope could give information for characterizing melanoma.
- To collect multi-spectral images of the skin lesions using the selected optical wavelengths and to analyze them for the diagnosis of melanoma.

1.3 Proposed Approach

The features used in the ABCD rule suggest that changes in the spatial/frequency and textural characteristics can be used for classifying the skin lesions. Among the different methods used for the analysis of spatial/frequency and textural information, the Gaussian Markov random field [21-23] and Gibbs distribution texture models [24-25] characterize the gray levels between nearest neighboring pixels by a certain stochastic relationship.

The weakness in these methods is that they focus on the coupling between image pixels on a single spatial scale and fail to characterize different scales of texture effectively. Wavelet transform [26-29], Gabor transforms [30-33] and Wigner distribution [30-33] are good multi-resolution analytical tools and help to overcome this limitation. Tree-structured wavelet decomposition determines important frequency channels dynamically based on image energy calculations within the different frequency bands and can be viewed as an adaptive multi-channel method [34].

To analyze the epi-illuminance images of the skin lesions and to classify them into melanoma and dysplastic nevus images the wavelet transform analysis is used. An adaptive wavelet transform based tree-structure classification method (ADWAT) is proposed. In this method tree-structure models of the different image classes are developed using a known set of images. The tree-structure models of melanoma and dysplastic nevus are then semantically compared with the tree-structure of the unknown skin lesion image for classification. Development of the tree-structure is dependent on threshold selections obtained from a statistical analysis of the feature set. This makes the classification method adaptive.

To select optimal wavelengths for multi-spectral imaging, study and understanding of light-tissue interaction is necessary. For modeling the light-tissue interaction, Kubelka-Munk, radiative transport theory and Monte Carlo methods are the three most common methods used [35]. The Kubelka-Munk description is applicable to one-dimensional geometries and accounts for propagation of diffuse fluxes only [36]. Hence, the results are not valid for measurement systems employing collimated or finite aperture light sources. Also, it is difficult to incorporate effects of diffuse reflectance at

the medium boundaries into models based on Kubelka-Munk theory. Exact analytical solutions of the radiative transport equations have been found only for a few special cases [37]. The numerical computation of the right equation with discrete ordinate method is a formidable task even for simple geometries. Techniques such as diffusion approximation [38-40] and Beer's law [41] have been used, which are valid for highly scattering and non-scattering materials. Photon interaction with matter is stochastic in nature and can be described using computer simulation with appropriately weighted random absorption and scattering events. Monte Carlo simulation is a statistical technique for simulating light-tissue interaction under a wide variety of situations [42-44].

To find optical wavelengths in the visible range, which when used with the Nevoscope can discriminate skin lesions based on their depths, the Monte Carlo simulation technique is used. Three-dimensional voxel based models of skin lesions with different depths and models of different skin types based on their epidermal melanin concentration are proposed. A voxel library is compiled using the wavelength dependent optical properties of tissue reported by various research groups. Voxels from the voxel library are used in the development of the tissue models. The optical properties of the voxels used in the models change according to the wavelength of the monochromatic light source used in the simulation. This makes the models wavelength dependent. A Monte Carlo simulation algorithm (MCSVL) for models generated using the voxel library is developed. The tissue models are simulated for diffuse reflectance measurements with an interval of 5 nm over the optical wavelength range of 350-700 nm. A correlation analysis between the lesion depth and the diffuse reflectance is then used to obtain wavelengths that produce high correlation coefficient values.

Multi-spectral skin lesion images using the selected wavelengths are collected. Using an analysis similar to the ADWAT method, wavelet transform based features are extracted from the multi-spectral trans-illumination images of the skin lesion. These features are combined with those obtained from the epi-illuminance images of the skin lesion using a white light source. The ADWAT classification method is extended to handle this combined feature set for improving the sensitivity and specificity of melanoma diagnosis. Most of the features used in the ADWAT classification method have a bimodal distribution with overlapping feature values between the image classes. Hence, fuzzy membership functions based method is also used to compare the classification results.

1.4 Organization of the Report

The report is divided in to five main parts: (1) Introduction and problem statement, (2) Background and literature review, (3) Methodology and implementation, (4) Results and discussion and (5) Conclusion and future work. Chapter 2 presents a brief review of the literature. In Section 2.1 the various approaches used in the analysis of spatial/frequency information and textural information are discussed. Section 2.2 describes the various methods used for modeling light-tissue interaction. The advantages and disadvantages of the methods described in Chapter 2, leads into the methods proposed in this study.

The implementations of the proposed methods are described in Chapter 3. Section 3.1 describes the ADWAT classification method while Section 3.2 describes the MCSVL algorithm, the concept of voxel library, the tissue models and the correlation analysis for optimal wavelength selection. In section 3.3 the multi-spectral images of the

skin lesion collected using the selected optimal wavelengths are analyzed. Wavelet transform based feature extraction and their significance is discussed in this section. The combined feature set obtained from the epi-illuminance and trans-illumination images is used for improving the classification of the melanoma. An Extended-ADWAT classification method and Fuzzy Membership Functions based method are employed for this purpose and the classification results are compared.

The results obtained are presented and analyzed in Chapter 4. Classification results of epi-illuminance images of skin lesions obtained using the ADWAT method are discussed in Section 4.1. Estimates of the diffuse reflectance obtained for the tissue models proposed and the results of the correlation analysis between lesion depth and diffuse reflectance are presented in Section 4.2. Section 4.3 presents the classification results obtained using the combined features from multi-spectral trans-illumination images and epi-illuminance images of the skin lesion. In Chapter 5, conclusions drawn from the work done so far towards development of the Nevoscope and improving the sensitivity and specificity of melanoma diagnosis are presented. Methods for further improving the Nevoscope capabilities as a diagnostic tool for melanoma are suggested based on these conclusions.

CHAPTER 2

LITERATURE REVIEW

2.1 Spatial/Frequency And Texture Analysis

It is very difficult to give the precise definition of texture that could be used in image analysis. It should describe local neighborhood properties of the gray levels, but also include some intuitive properties like roughness, granularity and regularity. Texture is defined in [45] as the feature, which describes spatial ordering of pixel intensities in a region. According to Jain [46], the term texture generally refers to repetition of basic texture elements called texels. Their placement can be periodic, quasi-periodic or random. Texture can be characterized using statistical properties of the region in an image that has a set of local statistics, or other local properties that are constant, slowly varying or approximately periodic [47-48].

The application of wavelet orthogonal representation to texture discrimination and fractal analysis has been discussed by Mallat [49]. Feature extraction for texture analysis and segmentation using wavelet transforms has been applied by Chang and Kuo [34], Laine and Fan [50], Unser [51], and Porter and Canagarajah [52]. The tree-structured wavelet transform decomposes a signal into a set of frequency channels that have narrower bandwidths in the lower frequency region. Decomposition of just the lower frequency region, as is performed in conventional wavelet transforms, may not be effective for image classification [30], [53-54]. This is suitable for signals consisting primarily of smooth components with information concentrated in the low frequency regions, but is not suitable for quasi-periodic signals whose dominant frequency channels

are located in the mid-frequency region. The most significant spatial and frequency information that characterizes an image often appears in the mid-frequency region. Thus, to analyze these types of signals wavelet packets are used [34]. In the wavelet packet analysis the decomposition is no longer applied to the low frequency channels recursively, but can be applied to the output of any channel.

Chang and Kuo [34] proposed a method for the development of wavelet transform-based tree structure decomposition. In this method, a set of known images used during the learning phase is decomposed using a two-dimensional wavelet transform to obtain the energy map and the dominant frequency channels. Decomposition of a channel is determined based on the ratio of the average energy of that channel to the highest average energy of a channel at the same level of decomposition. If the energy ratio exceeds a pre-determined threshold value, the channel is decomposed. The dominant frequency channels are then used as features for classification. Chang and Kuo [34] have suggested that the filter selection dose not have much influence on the texture classification. On the other hand experiments preformed by Unser [51] imply that the choice of a filter bank in the wavelet texture characterization could be an important issue. DeBrunner and Kadiyala [55] and Mojsilovic, Popovic and Rackov [56] have studied the effect of wavelet bases in texture classification using the method suggested by Chang and Kuo [34] and agree with the results obtained by Unser [51].

The tree structure method suggested by Chang and Kuo [34] has several major limitations, mainly, the selection of the threshold value used for subsequent decomposition and the assumption that high average energy is a good discrimination criterion. To overcome these limitations, an adaptive wavelet-based tree-structure

(ADWAT) analysis method is proposed. In the adaptive method, the channels that are decomposed are selected based on a statistical analysis of the feature data. The threshold is selected to give the best separation of features for channels that contain information useful for discrimination. Based on these thresholds the tree structure models for each of the image classes is obtained. In this study, the ADWAT method is used for a model-based classification of epi-illuminance images of skin lesions. The tree structure models of melanoma and dysplastic nevus are developed and are semantically compared with the tree structure of the unknown skin lesion image for classification. This method is compared with the one suggested by Chang and Kuo [34]. The ADWAT classification method is further extended to analyze and classify the multi-spectral trans-illumination image data.

2.2 Modeling Of Light-Tissue Interaction

Light-tissue interaction has many applications in medical diagnostics and therapeutic procedures such as photodynamic therapy [57], laser surgery [58], laser Doppler velocimetry [59] and pulse oximetry [60]. Controlled experimental studies to understand light interaction with tissue and measurements of optical properties are difficult to perform. Mathematical models of light propagation in tissue have been developed and studied over decades for this purpose. The exact assessment of light propagation in tissue would require a model that characterizes the spatial distribution and the size distribution of tissue structures, their absorbing properties and their refractive indices. However for real tissue, such as skin, the task of creating a precise representation either as a phantom or as a computer simulation is formidable. Tissue is mostly represented as an absorbing

bulk material with scatterers randomly distributed over the volume. The material is assumed isotropic and homogeneous, even though this is not a true representation of tissue.

Light entering the tissue is subjected to scattering and absorption. A small portion of the light is reflected at the surface and the remaining light is attenuated in the tissue by absorption and scattering according to Beer's law [61]

$$E(z) = E_0(1 - r_{sc})e^{-(\mu_a + \mu_s)z} \tag{2.1}$$

where E(z) is the fluence rate at position z, E_0 is the irradiance, r_{sc} is the specular reflection, μ_a is the absorption coefficient and μ_s is the scattering coefficient. Beer's law is only applicable when the tissue absorption dominates over the scattering. Between 300 and 1000 nm tissues have scattering dominating over absorption [62].

Radiative transfer was introduced by Chandrasekhar [37] to explain light propagation in stellar atmospheres, and has been extended to thermal diffusion of neutrons, radar back scattering and tissue optics. Radiative transfer abandons the wave nature of light. Light propagation is instead described by motion of photons in a medium containing discrete scattering and absorbing centers. Transport equation is an effective approach that describes transfer of energy through a turbid medium. It relates the gradient of radiance L at position r in direction s to losses owing to absorption and scattering and to gain owing to light scattered from all other directions s' in to direction s. The equation has the form

$$\frac{dL(r,s)}{ds} = -\mu_a L(r,s) - \mu_s L(r,s) + \mu_s \int_{4\pi} p(s,s')L(r,s')d\omega' + S(r,s) \tag{2.2}$$

where p is the phase function and S is the source of power generated at r in direction s [63]. The transport theory is often used in the diffusion approximation [64], i.e., at every point outside the incident beam radiative transfer is described only by the photon number density and the net photon flux. This is allowed if the light is scattered many times and as a result has an almost uniform angular distribution. The transport theory in the diffusion approximation or the diffusion theory was used by Reynolds et al. [65] to determine the relative reflectance by a whole blood medium.

Since the light propagation model must accurately simulate samples with arbitrary scattering to absorption ratios, anistropic scattering and boundaries, no analytical and few numerical options exist. Diffusion equation [63] is one of the common approximations. Kubelka-Munk (K-M) [66-68] is another approximation proposed. The K-M model was derived for diffuse incident flux with isotropic scattering and matched boundaries. The interior flux is divided in to two streams: a forward stream of strength I(z) and a backward stream of strength J(z). Each stream is scattered and absorbed according to the linear coefficients S and K respectively. The functions I(z) and J(z) are easily obtained by solving two simultaneous, first order differential equations:

$$\frac{K}{S} = \frac{1+R^2-T^2}{2R} - 1$$

$$S = (1/bd)\coth^{-1}\frac{1+T^2-R^2}{2Rb} \tag{3.3}$$

where d is the depth of the layer, T is the transmission coefficient equal to I(z=d) / I(z=0), R is the reflection coefficient equal to J(z=0) / I(z=0) and $b=\sqrt{[(K/S)(K/S+2)]}$. The K-M model can be extended to stacked layers by a straightforward ray-tracing analysis [63].

For situations where diffusion theory breaks down, the most useful method has been to apply Monte Carlo modeling [63] to simulate photon transport. In this computational technique, the multiple-scattering trajectories of individual photons are traced through the medium, each interaction being governed by the random process of absorption or scattering. Physical quantities of interest are scored within the statistical uncertainties of the finite number of photons simulated. The power of Monte Carlo method lies in its ability to handle virtually any source, detector and tissue boundary conditions, as well as any combination of tissue optical properties. However, it has the fundamental limitation that the physical parameter space is sampled only one point at a time, so that any single Monte Carlo simulation gives little insight into the functional relationships between measurable quantities and the optical properties. It also requires a large computational time.

Laser irradiation of skin using homogeneous [42] and layered geometries [43-44] has been effectively simulated using the Monte Carlo method. Flock, Wilson and Patterson [69] have compared the results of diffusion theory and Monte Carlo models for propagation of light in highly scattering tissue-like media. The Monte Carlo approach provided close agreement with the results of independent radiative transfer calculations [70], while the diffusion models examined [65,74] were inaccurate for predicting some of the characteristics of the light fluence distributions. Treatment of port wine stain combined with simple geometric shapes to approximate skin components have been simulated [42, 72-74]. Lucassen et al. [74] and Smithies et al. [73] have used layers, long cylinders and curved vessels to simulate the microstructure of skin. Wang, Jacques and Zheng [75], Prahl, Keijzer, Jacques and Welch [76] and Gardner and Welch [77] are

among the groups to estimate total diffuse reflectance and total transmittance in a semi-infinite layered medium for different optical conditions using independent Monte Carlo codes. Instead of using the typical layered geometry and cylindrical blood vessels, Pfefer et al [78] have used imaging techniques to define actual tissue geometry. Optical low coherence reflectometry images of rat skin were used to specify a 3D material array, with each entry assigned a label to represent the type of tissue in that particular voxel.

Layered tissue models in which the individual layers are assumed to be homogeneous are most commonly used by researchers. Although simple and easy to implement, a modular representation is more appropriate for modeling geometrically complex non-homogeneous tissue. There are two primary methods to represent an object in a mathematical simulation: a shape-based method [79] and a voxel-based method [80]. The shape-based approach describes the boundaries of each object by mathematical equations. Using this approach it is difficult to describe irregular boundaries. The voxel-based approach represents an object by a union of the voxels. The accuracy with which irregular boundaries can be described using the voxel-based approach depends on the size of the voxels. Once the object description is done, using several physical and probabilistic features such as absorption coefficient, scattering coefficient, anisotropy factor and refractive index, the photon random walk is simulated repeatedly until an acceptable variance is obtained.

The Monte Carlo method takes into account the changes in the value of the refractive index between two tissue layers or tissue components. This is used to establish the boundaries where the photon would be reflected or refracted. The Monte Carlo program needs specific modifications for every model, to take into account the changes in

the medium with respect to the boundaries of the absorbing tissue from one model to another. A concept of voxel library and its use in developing complex homogeneous and non- homogeneous tissue models is presented here. The voxel library offers flexibility of independently changing the physical and optical properties of the voxels. Models developed using the voxel-based method require no alterations in the Monte Carlo program. A Monte Carlo simulation algorithm (MCSVL) for models generated using the voxel library is developed. The simulation results obtained using MCSVL are compared with published data for verification of the algorithm. Skin models of different skin types [81] based on the epidermal melanin concentration are presented. Tissue reflectance spectra for the skin models developed using the voxel library are presented for optical wavelengths with an interval of 5 nm over the range of 350-700 nm. Nevus models of various depths are formed and incorporated into the skin models. These models are simulated using the Nevoscope optical geometry. A correlation analysis is performed between the lesion depths and tissue reflectance to obtain wavelengths with maximum correlation coefficient values.

CHAPTER 3

METHODOLOGY

3.1 Classification of the Epi-illuminance Images

In this section the ADWAT method and the tree structure classification method with constant threshold suggested by Chang and Kuo [34] are described in detail. Also, the epi-illuminance image data and the channel designation used for the wavelet decomposition of an image are described.

3.1.1 Epi-illuminance Image Data

Epi-illuminance images of skin lesions of individuals from various age groups and gender were collected using the Nevoscope [14-15]. A 100W halogen light source was used for illumination. Images were collected with an Agfa digital camera (ePhoto-1280) and were 16-bits, 1024 x 768 pixels in size. The lesion images were collected over a period of one year by imaging suspicious lesions on 173 individuals under the observation of a cancer specialist. From these image data, 25 cases of melanoma were confirmed by biopsy and histological examination. Images were split into two sets for classification. The learning (known) set consisted of 15 images of melanoma and 15 images of dysplastic nevus. The testing (unknown) set used in the classification consisted of 10 images of melanoma and 20 images of dysplastic nevus. The same set of images was used for each classification method. Sample images of melanoma and dysplastic nevus from the data set and an image of normal skin are shown in Figure 3.1.

3.1.2 Image Decomposition

All images were decomposed in Matlab using the Daubechies-3 (db3) wavelet. The channel designation used in this study for the wavelet decomposition of an image and the resulting sub-images is the same for both tree structure methods. The main image is numbered as 0 and its low-low, low-high, high-low and high-high filter channels are numbered 1, 2, 3 and 4, respectively, for the first level of decomposition. The channels for the second level of decomposition of channel 1 are numbered 1.1, 1.2, 1.3 and 1.4, and so on for the other channels and further levels of decomposition. An example of wavelet decomposition of a sample skin lesion image with the corresponding channel designation and tree structure are given in Figure 3.2. According to the method suggested by Chang and Kuo [34], in this figure channels 1.2.1-1.2.4 and 4.1.1-4.1.4 would be considered as dominant frequency channels. After the channels are decomposed their mean energy is calculated as described below to obtain the features for classification.

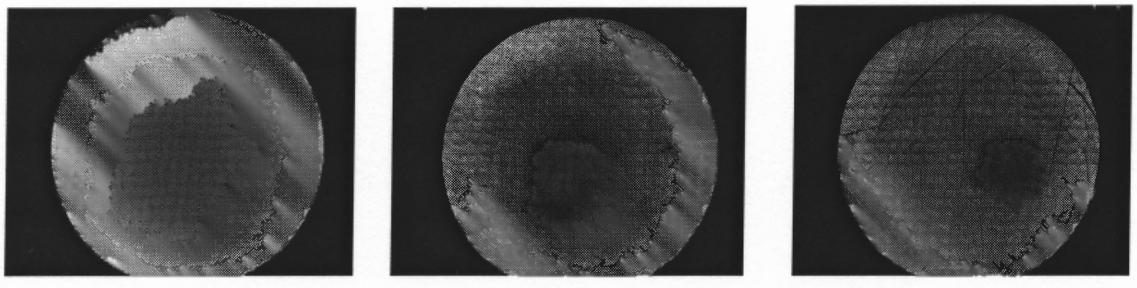

(a) (b) (c)

Figure 3.1 Epi-illuminance images: (a) normal skin, (b) malignant melanoma and (c) dysplastic nevus. The images of melanoma and dysplastic nevus are representative of those included in the data set.

3.1.3 Tree Structure Classification Method

Chang and Kuo [34] suggested a method for the development of a wavelet transform based tree structure and its use in classifying a data set based on the spatial/frequency information contained in the images. This method detects those channels that contain significant information and then selectively decomposes them further. Each image is decomposed into 4 sub-images at each level of decomposition.

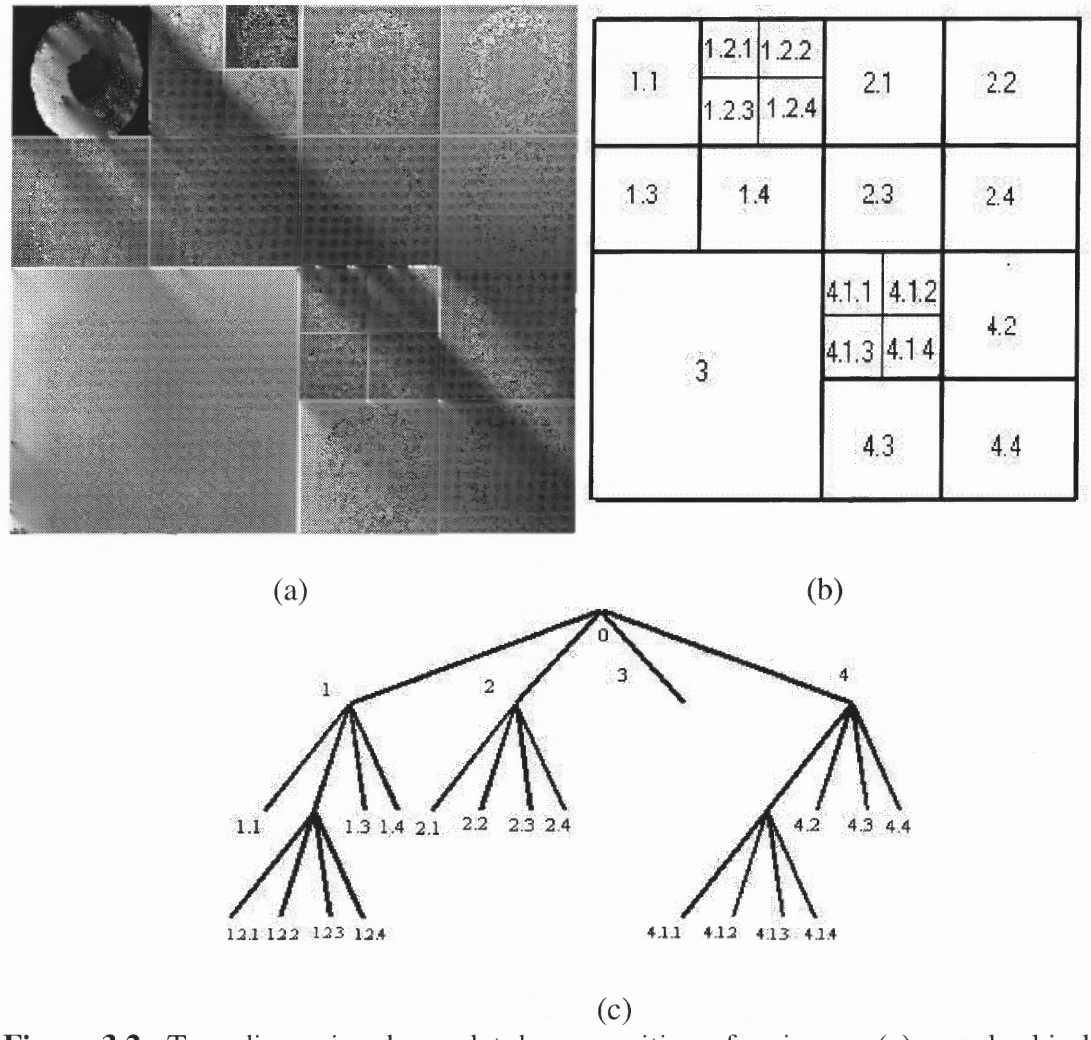

Figure 3.2 Two-dimensional wavelet decomposition of an image: (a) sample skin lesion image decomposed (b) the corresponding channel designation and (c) the corresponding tree structure. For the image illustrated here, channels 1, 2 and 4 undergo second level decomposition and channels 1.2 and 4.1 undergo third level decomposition.

The mean energy, e, of a sub-image, or channel, f (m, n) was then calculated as

$$e = \frac{1}{MN} \sum_{m=1}^{M} \sum_{n=1}^{N} |f(m, n)| \tag{3.1}$$

where M and N are the pixel dimensions of the image f (m, n) in the x and y directions, respectively [34]. Further decomposition of the sub-image was determined by comparing the average energy, e, of the sub-image with the largest average energy value, e_{max}, in the same decomposition level. Decomposition of the sub-image was stopped if $e/e_{max} < C$, where C is a threshold constant; otherwise, the image was decomposed further into its 4 sub-images. The maximum number of decomposition levels used was determined by the resolution of the main image. For our data set 4 levels of decomposition were used. This method was implemented for threshold constant values ranging from 0.05 to 0.018. This range of the threshold constant resulted in selective decomposition from one to four of the first level sub-images. For values below 0.018 all the channels were decomposed and for values above 0.05 only channel 1 was decomposed further. For both of these cases classification is not possible, as identical tree structures would be obtained for melanoma and dysplastic nevus images.

Once the tree structure was developed, the energy in the leaves of the tree defined the energy function in the spatial-frequency domain, or the energy map. The energy map for a particular image class was obtained by averaging the energy maps over all the samples from the same class. This energy map was used in the texture analysis and classification of the unknown images, where each leaf of the tree corresponded to a feature. Each unknown image was decomposed to obtain its tree structure and energy map using the same decomposition algorithm as used for the known images. The distance between the features of an unknown image and the corresponding features of the set of

known images was used to classify the candidate image to either the melanoma or dysplastic lesion class. The Mahanalobis distance [82], D_i, was used as the discrimination function for classification of each unknown image. D_i was calculated for each unknown image as

$$D_i = \sum_{j=1}^{J} \frac{(x_j - m_{ij})^2}{c_{ij}} \tag{3.2}$$

where x_j denotes the mean energy of the j^{th} dominant channel for the unknown image, m_{ij} denotes the corresponding mean energy value of the j^{th} channel for the image class i, and c_{ij} represents the variance of channel j for image class i. The first 8 dominant frequency channels were used in this analysis, so the value of J used was 8. For our data with only two-image classes, melanoma and dysplastic nevus, the value of i was either 1 or 2. An unknown image was assigned to image class 1 if $D_1 < D_2$; otherwise, the image was assigned to image class 2.

3.1.4 Adaptive Wavelet-based Tree-Structure (ADWAT) Classification Method

A new Adaptive Wavelet-Based Tree-Structure (ADWAT) method is presented here to address two major limitations of the tree structure classification method described in Section 3.1.3. First, additional features are selected so that channels are decomposed as a result of their discrimination content and not solely on maximum energy. Porter and N. Canagarajah [87] proposed the ratio of the mean energy in the low-frequency channels to the mean energy in the middle-frequency channels as a criterion for optimal feature selection. These low to middle frequency ratios of channel energies emphasize the spatial/frequency differences in an image. Second, the threshold value used for selecting the decomposition channels is selected adaptively based on a statistical analysis of the

feature data. Thus, various ratios of channel energies or their combination over a given decomposition level are used as additional features and a statistical analysis of the feature data is used to find the threshold values that optimally partitions the image-feature space for classification. The ADWAT method for classification is described below.

3.1.4.1 Feature Set. Features are computed so that channels are decomposed as a result of their discrimination content and not only on maximum energy. For each level of decomposition, four sub-images are created and the average energy of each channel is calculated according to Equation (3.1).

Table 3.1 Feature Calculations at Each Level of Decomposition: Illustrated with decomposition of channel 1. At each level of decomposition, the average energy of each sub-image is calculated with the corresponding energy ratios. These features are used in a statistical analysis to select the optimal feature set for image classification.

Sub-image or Channel	**Features**		
	Average Energy	**Maximum Energy Ratio**	**Fractional Energy Ratio**
1.1	e1.1	e1.1/emax	e1.1/(e1.2+e1.3+e1.4)
1.2	e1.2	e1.2/emax	e1.2/(e1.1+e1.3+e1.4)
1.3	e1.3	e1.3/emax	e1.3/(e1.1+e1.2+e1.4)
1.4	e1.4	e1.4/emax	e1.4/(e1.1+e1.2+e1.3)

1. Of the four average energies calculated, the greatest is designated emax.
2. Since emax is the maximum average energy (either e1.1, e 1.2, e1.3, or e 1.4) only three of the ratios to maximum energy are used as features; the fourth ratio is always 1.

In addition several energy ratios are also calculated and used as features as shown in Table 3.1. The average energies and energy ratios generate 11 features per channel, resulting in 11 features from the first level of decomposition, 44 features from the second level of decomposition, and 176 features from the third level of decomposition.

3.1.4.2 Threshold Selection. The mean, variance and the histogram of the feature values for each of the target classes are used to determine if a feature generated a unimodal distribution or segregated into a bimodal distribution between the image classes. The sample mode (most frequently occurring value) was used as an estimator for the population mode. The descriptive Statistics tool in Microsoft Excel was used for this purpose. This analysis tool generated a report of univariate statistics for the data in the input range, providing information about the central tendency and variability of the data. Based on the histogram of the data values, the number of modes present in the data was estimated and the mean and variance of the data was calculated.

During the learning phase the known set of melanoma and dysplastic nevus images were used. For the classification of skin images, all images were decomposed up to 4 levels using the Daubechies-3 (db3) wavelet. Thresholds for channel decomposition were obtained by performing a statistical analysis on the feature values derived from the average channel energies.

All pooled feature values that generated unimodal distributions were rejected. Out of the total 231 features, 214 features were rejected for this reason. For all features that segregated into bimodal distributions between image classes, thresholds were calculated. If more than one feature within a particular channel were distributed bimodally, then the feature that generated linearly separable pure clusters for the two classes was used in the analysis. For all such features, energy ratio thresholds were calculated by averaging the highest value from the lowest valued class with the lowest value from the highest valued class. According to the minimum distance classifier, taking the average value of the means of the two classes as a threshold would be optimum in the Bayes sense [83]. This

requires that the distance between the means is large compared to the spread or randomness of each class with respect to its mean. Since this is not true for any of the linearly separable features, average of the separation between the two classes was used as a threshold. For all the remaining channels having features with bimodal distribution that did not produce linearly separable pure clusters, the feature with greater separation of the two class means compared to the variance of the two classes was used in the analysis. All such features were assumed to follow a Gaussian distribution with each of the two image classes having the same probability of occurrence equal to 0.5. The optimal energy ratio threshold for these features with the minimal classification error was calculated as the average of the means of the two Gaussian distributions [83].

3.1.4.3 Development of Tree Structure Signatures. Based on the thresholds selected above, the image decomposition algorithm was developed to obtain the tree structure for each of the image classes. Decomposition was stopped for a channel if all of its features for the two classes followed unimodal distributions. Each channel that had at least one feature that was bimodally distributed was decomposed further if its feature value satisfied the corresponding energy ratio threshold. Since the thresholds were selected to optimally partition the two image classes, one of the two image classes was preferentially decomposed. In this analysis, many more dysplastic nevus images were available than melanoma images. Thus, the dysplastic nevus class was used as the reference group and the thresholds were set such that images of this type were not decomposed. The tree structures that resulted from this decomposition form the signatures of the melanoma and dysplastic nevus image classes.

3.1.4.4 Classification Phase. During the classification phase the tree structure of the candidate image obtained using the same decomposition algorithm described previously was semantically compared with the tree structure signatures of melanoma and dysplastic nevus. A classification variable, CV, is used to rate the tree structure of the candidate image. CV is set to a value of 1 when the main image is decomposed. The value of CV is incremented by one for each additional channel decomposition. When the algorithm decomposes a dysplastic nevus image, only one level of decomposition should occur (channel 0). Thus, for values of CV equal to 1, a candidate image was assigned to the dysplastic nevus class. A value of CV greater than 1 indicates further decomposition of the candidate image, and the image was accordingly assigned to the melanoma class.

3.2 Light-Tissue Interaction Modeling

In this section the MCSVL algorithm and the development of tissue models using the concept of voxel library are described. This is followed by the description of the simulation setups used for verification of the algorithm and simulations of the skin lesion models with the Nevoscope optical geometry. Finally, the correlation analysis between the lesion depth and diffuse reflectance is described. Optical wavelengths for multi-spectral imaging of the skin lesions are selected based on the correlation analysis.

3.2.1 Photon Random Walk

The MCSVL algorithm for simulating light-tissue interaction using Monte Carlo techniques is implemented in the MATLAB environment. Figure 3.3 shows the flowchart of the MCSVL algorithm. The flowchart can be divided into four sections: 1. launching the photon, 2. photon movement within the tissue and the photon tissue interaction, 3.

photon hitting a boundary and 4. photon termination. These sections are marked with dotted boxes on the flowchart and are briefly describe below.

The presented method is based on the approach presented by Wang, Jacques and Zheng [75]. Their program, MCML, works with homogeneous layered-tissue models. A boundary between two layers where the refractive index changes occurs only along the depth of the tissue in a homogeneous layered-tissue model. However in the voxel-based approach for non-homogeneous tissue models this boundary can occur between two adjacent voxels. These two voxels with different refractive indices could be side by side or one above the other. The calculations related to the photon hitting the boundary from the MCML program are therefore extended to handle boundaries between adjacent voxels of the voxel-based model in the MCSVL program.

The Cartesian coordinate system with the Z-axis perpendicular to the skin surface and the X-Y plane along the skin surface is used to specify the photon position. Figure 3.4 depicts the axis orientation of the Cartesian coordinate system with respect to the tissue block. The algorithm begins with the launch of a photon with a weight of W equal to 1 at location (0, 0, 0). The initial direction cosines (μ_x, μ_y, μ_z) are specified to represent the angle of incidence with respect to the skin surface. If the photon direction is specified by a unit vector r, the direction cosines (μ_x, μ_y, μ_z) are given by

$$\mu_x = rx \quad , \quad \mu_y = ry \quad \text{and} \quad \mu_z = rz \tag{3.3}$$

where x, y and z are unit vectors along each axis.

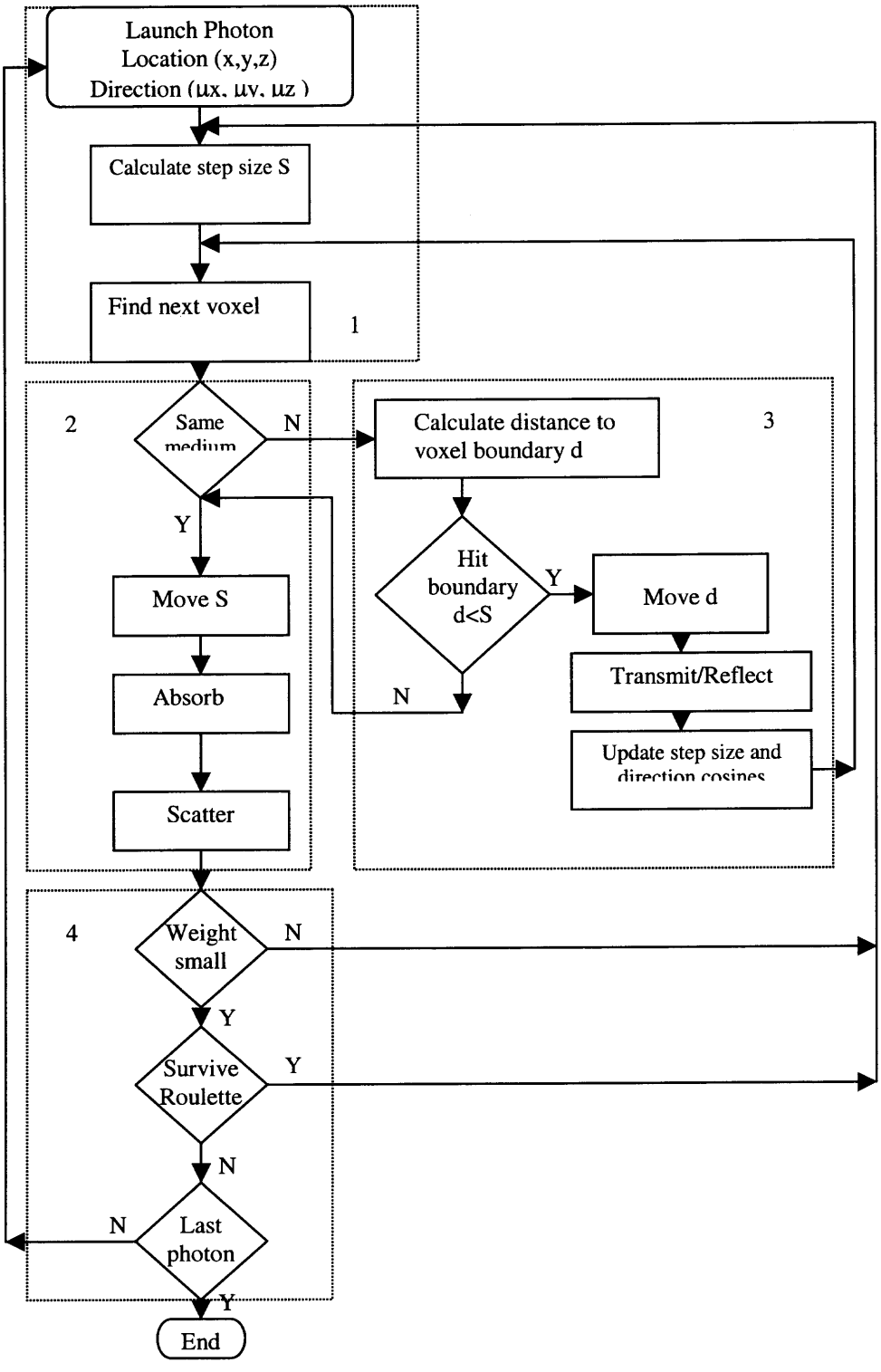

Figure 3.3 Flowchart of the MCSVL algorithm: 1. launching the photon, 2. photon movement within the tissue and the photon tissue interaction, 3. photon hitting a boundary and 4. photon termination.

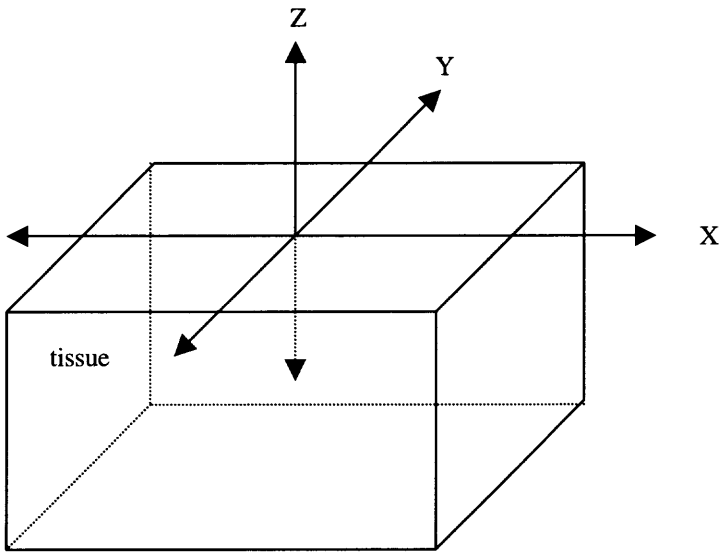

Figure 3.4 Axis orientation of the Cartesian coordinate system.

If a refractive index mismatch occurs between the ambient and the tissue then specular reflection R_s is subtracted from the initial photon weight W. R_s is computed using the Fresnel's equation

$$R(\alpha_i) = \frac{1}{2}\left[\frac{\sin^2(\alpha_i - \alpha_t)}{\sin^2(\alpha_i + \alpha_t)} + \frac{\tan^2(\alpha_i - \alpha_t)}{\tan^2(\alpha_i + \alpha_t)}\right] \tag{3.4}$$

where the refractive index of the ambient is n_1 and that of the tissue is n_2. After accounting for specular reflection, the photon step size S is calculated using

$$S = -\ln(\xi)/(\mu_a + \mu_s) \tag{3.5}$$

where μ_a is the local absorption coefficient, μ_s is the scattering coefficient and ξ is a random number uniformly distributed in the interval [0, 1]. The current photon location (x, y, z), the direction cosines (μ_x, μ_y, μ_z) and the path length S are then used to determine the next potential location of the photon-tissue interaction using

$$x_1 = x + \mu_x S \quad , \quad y_1 = y + \mu_y S \quad , \quad z_1 = z + \mu_z S \tag{3.6}$$

where x_1, y_1 and z_1 are the coordinates of the new location. If the photon is still within the same medium it is moved to this new location and its weight is decreased by an amount ΔW, due to absorption within the tissue. The change in weight is given by

$$\Delta W = (\mu_a / \mu_t)\, W \tag{3.7}$$

where μ_t is the tissue interaction coefficient equal to the sum of the local absorption coefficient μ_a and the scattering coefficient μ_s.

The new direction of the photon is then calculated by random selection of the deflection and azimuthal angles. The deflection angle θ ($0 \leq \theta \leq \pi$) is sampled statistically using the probability distribution of the cosine of the deflection angle, $\cos\theta$, described by the scattering function proposed by Henyey and Greenstein [84]. It is given by

$$p(\cos\theta) = \frac{1 - g^2}{2\left(1 + g^2 - 2g\cos\theta\right)^{3/2}} \tag{3.8}$$

where the anisotropy factor, g, equals $\cos\theta$ and has a value between -1 and 1 and is dependent on the scattering characteristics of the tissue. The anisotropy factor is equal to 0 for isotropic scattering and is equal to 1 for forward directed scattering. The choice for $\cos\theta$ can be expressed as a function of the random number ξ_1 uniformly distributed in the interval [0, 1] as

$$\cos\theta = \frac{1}{2g}\left[1 + g^2 - \left(\frac{1 - g^2}{1 - g + 2g\xi_1}\right)\right] \quad \text{if } g = 0$$

$$\cos\theta = 2\xi_1 - 1 \quad \text{if } g = 0 \tag{3.9}$$

The azimuthal angle φ is independent of the tissue properties and is uniformly distributed over the interval [0, 2π]. It value is obtained using

$$\varphi = 2\pi\xi_2 \tag{3.10}$$

where ξ_2 is a random number uniformly distributed in the interval [0, 1] .

Using the deflection angle θ and the azimuthal angle φ new direction cosines for the photon movement are then calculated using

$$\begin{aligned}
\mu_x' &= \sin\theta\left(\mu_x\mu_z\cos\varphi - \mu_y\sin\varphi\right)\Big/\sqrt{1-\mu_z^2} + \mu_x\cos\theta \\
\mu_y' &= \sin\theta\left(\mu_y\mu_z\cos\varphi - \mu_x\sin\varphi\right)\Big/\sqrt{1-\mu_z^2} + \mu_y\cos\theta \\
\mu_z' &= -\sin\theta\cos\varphi\sqrt{1-\mu_z^2} + \mu_z\cos\theta
\end{aligned} \tag{3.11}$$

The photon is now ready to take another step in the new direction described by the updated direction cosines. This process of photon interaction with the tissue, i.e., absorption and scattering at the end of every step is repeated until the photon weight has been sufficiently reduced and it is terminated or when the photon escapes from the tissue. The process is also interrupted, when the photon hits a boundary between two tissue layers or objects with different values of refractive index, before completing its step movement. The subroutine for photon hitting the boundary is described later in this section. For terminating the photon based on its weight a threshold W_{th} equal to 0.0001 is used and it is compared with the photon weight after every interaction. When the photon weight becomes less than the threshold, further propagation of the photon yields little information. To terminate such photons and also ensure conservation of energy, a technique called Russian roulette [85-86] is used to decide if the photon should be terminated. This technique gives a photon one chance in m of surviving with a weight of

mW_r, were W_r is the present weight of the photon. A value of m equal to ten is used, thus giving a photon one-tenth chance of survival with a weight of $10W_r$. A random number uniformly distributed in the interval [0, 1] is compared with 1/m and the photon survives if the random number is less than or equal to 1/m. This method conserves energy, yet terminates photons in an unbiased manner.

If the photon hits the boundary between two tissue layers or objects with different values of refractive index before completing the step, it may be either internally reflected or transmitted across the boundary. The probability of the photon being internally reflected is calculated. It depends on the angle of incidence, α_i, onto the boundary and the angle of transmission, α_t. The value of α_i is calculated using the cosine inverse of the direction cosine with respect to the axis perpendicular to the plane of incidence. For example if the photon hits a boundary parallel to the X-Y plane then

$$\alpha_i = \cos^{-1}\left(|\mu_z|\right) \tag{3.12}$$

where μ_z is the direction cosine with respect to the Z axis. Next, the angle of transmission, α_t is calculated using the Snell's law

$$n_i \sin\alpha_i = n_t \sin\alpha_t \tag{3.13}$$

where the refractive indices of the media that the photon is incident from and transmitted to are n_i and n_t respectively. Using α_i and α_t, the internal reflectance R (α_i) is calculated using Fresnel's formulas [87-88]

$$R(\alpha_i) = \frac{1}{2}\left[\frac{\sin^2(\alpha_i - \alpha_t)}{\sin^2(\alpha_i + \alpha_t)} + \frac{\tan^2(\alpha_i - \alpha_t)}{\tan^2(\alpha_i + \alpha_t)}\right] \tag{3.14}$$

By generating a random number ξ_3 uniformly distributed in the interval [0,1] and comparing it with the internal reflectance, it is determined whether the photon is internally reflected.

$$\text{If } \xi_3 \leq R(\alpha_i), \text{ the photon is internally reflected}$$
$$\text{If } \xi_3 > R(\alpha_i), \text{ the photon transmitted through the boundary} \tag{3.15}$$

For the photon movement, the distance to the boundary, S1, is calculated and the photon is moved to the boundary. The step size is then updated using

$$s \leftarrow s - s_1 \tag{3.16}$$

where the arrow points to the value being updated. If the photon is internally reflected, then its direction cosines are updated by reversing the sign of the direction cosine used in calculating α_i and keeping the values of the other two direction cosines same. For example if the photon hits a boundary parallel to the X-Y plane then the new direction cosines would be

$$\mu_x \leftarrow \mu_x, \quad \mu_y \leftarrow \mu_y \quad \text{and} \quad \mu_z = -\mu_z \tag{3.17}$$

The photon now continues in the same medium with the remaining step size using the updated direction cosine values.

If the photon is transmitted across the boundary, then the remaining step size obtained using Equation (3.16), is updated for the new tissue medium according to its optical properties using

$$s \leftarrow \frac{s\mu_{t1}}{\mu_{t2}} \tag{3.18}$$

where μ_{t1} is the interaction coefficient of the medium in which the photon is present and μ_{t2} is the interaction coefficient of the medium to which the photon is transmitted. The direction cosines are updated according to the ratio of the two refractive indices across the boundary and the angle of transmission, α_t. For example, if the photon hits a boundary parallel to the X-Y plane then the new direction cosines will be

$$\mu_x \leftarrow \mu_x \frac{n_i}{n_t}, \quad \mu_y \leftarrow \mu_y \frac{n_i}{n_t} \quad \text{and} \quad \mu_z = \cos(\alpha_t) \tag{3.19}$$

where n_i is the refractive index of the medium from where light is incident and n_t is the refractive index of the medium where light is transmitted to. The photon is now ready to move by the updated step size in the direction specified by the updated direction cosines within the new medium.

Besides terminating the photon due to its weight, it is also terminated when it escapes the tissue. This can occur when the photon hits the tissue-ambient interface and a decision of transmission is taken using Equations (3.12) - (3.15). The photon weight is then added to the diffuse reflectance if it is collected by the top detector array or to the transmittance if it is collected by the bottom detector array.

In the voxel-based simulation, the photon is transported voxel-by-voxel within the medium. When the photon starts in one voxel and ends in another voxel, the media that these two voxels and the voxels in between represent need to be checked. If any two adjacent voxels between the starting and end voxel have different values of the refractive index, then the procedure for a photon hitting a boundary needs to be followed, as explained above. The standard procedure for photon movement voxel-by-voxel is to find the neighboring voxel and locate the point, E, where the photon exits the voxel. The

distance, d, between this point and the initial position of the photon is calculated and compared with the step size S. If the step size S is greater than the distance d, the photon is moved to the exit point and S is reduced by an amount d. If the refractive indices of the current voxel and the next voxel are the same then the photon either moves the remaining step size or moves to the boundary of the next voxel depending upon the minimum distance between the two. If the refractive index of the adjacent voxel is different then the photon may be internally reflected within the same voxel or transmitted to the next voxel. The decision of internal reflection or transmission is made using Equations (3.12) – (3.15). If internally reflected the photon can move the remaining step size given by Equation (3.16) in the direction specified by the updated direction cosines obtained using Equation (3.17). If the photon is transmitted through the boundary it can move the updated step size given by Equation (3.18) in the direction specified by the updated direction cosines obtained using Equation (3.19).

Most of the photon movement is within a uniform medium and the neighboring voxels along the photon path have the same refractive index. Checking the boundary conditions at every voxel interface is not required as is done in the voxel-by-voxel calculations explained above. The photon accelerating method suggested by Sato and Ogawa [89] for the photon transport is used in the MCSVL code to improve the simulation efficiency. In this method, the layer or object boundary is checked by comparing the refractive indices of all the voxels within the photon path. If all these voxels have the same refractive index then the photon is free to move and interact with the tissue. On the other hand if the refractive index changes along the photon path, an object boundary is present and its distance from the existing photon location is calculated

and compared with the step size. If the step size is smaller than this distance the photon can take this step, otherwise the photon is moved to the boundary and it is decided whether it will be reflected or refracted. Thus the calculation of the exit point E and its distance d from the initial position is omitted at each and every voxel interface along the path. By using this method, instead of having checkpoints at every voxel interface along the path, only two checkpoints are required before the photon-tissue interaction and this improves the simulation efficiency.

3.2.2 Tissue Models and Voxel Library

The tissue material grid corresponds in size one-to-one with the grid that accumulates the absorbed photon weights. Voxels representing the different tissue media are grouped together to form a three-dimensional tissue block. The position of a particular voxel in this tissue block is dependent on the tissue model. The dimensions of the voxel (Δx, Δy, Δz) and the number of voxels in each direction are used to establish the grid skeleton. The photon location in this three-dimensional array forming the tissue material grid is specified using Cartesian coordinates (x, y, z) or voxel indices (i, j, k). If all the voxels are of the same size and shape a simple routine can be used to convert from Cartesian location to voxel index and vice versa. All the voxels are assigned a voxel type number corresponding to their media type. For example in a three-layer skin model the media types could be stratum corneum, epidermis and dermis and 1, 2 and 3 could be the voxel type numbers assigned to the voxels of these media type respectively. So the three-dimensional material grid array corresponding to this three-layer skin model will have only these three numbers. The MCSVL algorithm, based on the photon location gets the voxel type number and then reads a text file corresponding to this voxel type number to

obtain its physical and optical properties. The physical properties are the size and shape of the voxel and the optical properties are the absorption and scattering coefficients, anisotropy factor and index of refraction. A collection of all these text files is the voxel library. Since the optical properties of a particular medium are wavelength dependent, editing the optical properties in these text files according to the wavelength used in the study is one option. Instead, different text files are formed, one for every wavelength, is containing the optical properties of the medium for a given wavelength. These text files are then assigned to different voxel type numbers, although they all represent the same medium. Now if the wavelength studied is changed one only needs to change the voxel type numbers in the three-dimensional material grid array. The voxel library offers the flexibility of updating the optical properties of the voxel or adding new media types into the library as new experimental results are reported.

All voxels in the library are rectangular in shape. The voxel dimensions (Δx, Δy, Δz) can be selected based on the object to be described and the resolution required in the study. Cubical voxels with all dimensions equal to 10μm are used in this study. Computer memory is an important factor affecting the time required for completing a simulation. In the MCSVL algorithm the three-dimensional material grid array is split into two-dimensional arrays parallel to the skin surface. The processor accesses three of these two-dimensional arrays, one containing the voxel in which the photon is present and one array above and below it at a given time. Thus the computer can read the voxel in which the photon is present and all its 6 neighboring voxels and is free from any unwanted information related to the material grid above and below these arrays. This saves the computer memory and helps to improve the computational speed.

3.2.3 Optical Properties

Based on the experimental and analytical results reported by various researchers, so far 355 types of voxels based on the difference in the medium or the difference in the optical properties of a medium for different wavelengths are compiled.

The values for refractive index for tissue used by various researchers range from the value of refractive index of water to value slightly higher than 1.5. Bolin et al. [90] used fiber optic cladding method to find the refractive index of tissue. Refractive index was measured over the range of 390-700nm. From these experiments it can be concluded that the refractive index of the tissue changes slightly over the visible spectrum and hence can be approximated by a constant value. The values of refractive indices used in this study are 1.45, 1.4 and 1.4 for the stratum corneum, epidermis and dermis respectively. The value of refractive index for air is taken equal to 1. Zeng et al. [91] also used these values in their tissue model.

For the optical properties of the stratum corneum the data reported by Gemert et al. [95] is used. They used collimated and diffuse transmission and diffuse reflection measurements obtained using a 10μm thick sample of 90% pure stratum corneum reported by Everett et al. [92] to analyze the values of μa and μs of the stratum corneum as a function of wavelength. They have published the values for a wavelength range of 250-400nm. These values are extrapolated up to 700nm using least square approximation techniques. For the anisotropy factor the data published by Bruls [93] using goniometer measurements of in- vitro stratum corneum is used.

For the epidermal scattering coefficient the data reported by Gemert et al. [95] is used. They have obtained the wavelength dependent values of μs for epidermis using the

values of g deduced from Brul's [93] experiment and the epidermal diffuse integrating sphere measurements reported by Wan et al. [36].

The absorption coefficients for the epidermis are approximated using the analytical formulas given by Jacques [81]. The absorption coefficient value is given as a function of wavelength and the volume fraction of the epidermis occupied by melanosomes. The epidermal absorption coefficient is a combination of the skin baseline absorption coefficient, $\mu_{Baseline}$, and the absorption coefficient of a single melanosome, $\mu_{melanosome}$. The analytical equation for the skin baseline absorption coefficient (cm^{-1}) is given by

$$\mu_{Baseline} = 0.244 + 85.3\exp(-(\lambda - 154)/66.2) \tag{3.20}$$

The absorption coefficient of a single melanosome (cm^{-1}) is approximated using expression

$$\mu_{melanosome} = \left(6.6x10^{11}\right)\left(\lambda^{-3.33}\right) \tag{3.21}$$

The absorption coefficient for the epidermis (cm^{-1}) combines the skin baseline absorption and the melanosome absorption and is approximated using the following formula

$$\mu_{epidermis} = f_{mel}\mu_{melanosome} + \left(1 - f_{mel}\right)\mu_{Baseline} \tag{3.22}$$

where λ is the wavelength in nm and f_{mel} is the volume fraction of the epidermis occupied by melanosomes. According to Jacques [81] f_{mel} ranges from 1.3-6.3% for white color skin, 11-16% for brown/olive color skin and 18-43% for black color skin. Using the average volume fraction of melanosomes within the tissue color range, the values for epidermal absorption coefficients for 71 wavelengths in the range of 350-700 nm with 5nm interval are calculated using Equations (3.20) – (3.22). The values of the average

volume fraction of melanosomes used are 3.8% for white skin, 13.5% for brown/olive skin and 30.5% for the black skin type.

For the scattering coefficients of the dermis the values reported by Gemert et al. [95] are used. They have used the Kubelka-Munk coefficients of the dermal tissue obtained from integrating sphere measurements reported by Anderson and Parrish [94] along with the values of g given by Jacques et al. [95] to calculate the scattering coefficient values for the dermis as a function of wavelength. The absorption coefficient for the dermis is a combination of the oxy and deoxy-hemoglobin absorption. Cui and Ostrander [96] have reported these values as a function of wavelength based on diffusion theory and experimental results.

The experimental and analytical results mentioned above were used to obtain the optical properties of the voxels in the voxel library. Table 3.2 gives summary of the data source for the optical properties of the tissue used in this study. For the data on which no analytical equations are reported, the measurement and scaling tools in Adobe Photoshop are used to approximate the values from the scanned images of these published results. Values were obtained for 71 different wavelengths, every 5nm in the wavelength range of 350-700nm. Figure 3.5 shows the scatter plots of these optical properties as a function of wavelength.

The values of the absorption coefficient, the scattering coefficient and the anisotropy factor form a set of the optical properties. 71 sets of values each for the optical properties of the skin layers, stratum corneum and dermis, corresponding to the 71 wavelengths used in this study are compiled. The epidermal tissue is classified into the three skin color types using the values of the average volume fraction of melanosomes

Table 3.2 Summary of the Data Source for the Optical Properties

Skin Layer	Optical Property	Data source
Stratum corneum	Scattering Coefficient	Gemert, Jacques, Sterenborg and Star [62] *
	Absorption Coefficient	Gemert, Jacques, Sterenborg and Star [62] *
	Anisotropy factor	Bruls [93]
Epidermis	Scattering Coefficient	Gemert, Jacques, Sterenborg and Star [62] **
	Absorption Coefficient	Jacques [81]
	Anisotropy factor	Bruls [93]
Dermis	Scattering Coefficient	Gemert, Jacques, Sterenborg and Star [62] ***
	Absorption Coefficient	Cui and Ostrander [96]
	Anisotropy factor	Jacques, Alter and Prahl [95]

* Data obtained using the collimated and diffuse transmission and diffuse reflection measurements by Everett, Yeargers, Sayre, and Olsen [92].

** Data obtained using the epidermal diffuse integrating sphere measurements reported by Wan, Anderson and Parrish [36] and the values of g reported by Brul [93].

*** Data obtained using the Kubelka-Munk coefficients of the dermal tissue obtained from integrating sphere measurements reported by Anderson and Parrish [94] along with the values of g given by Jacques, Alter and Prahl [95]

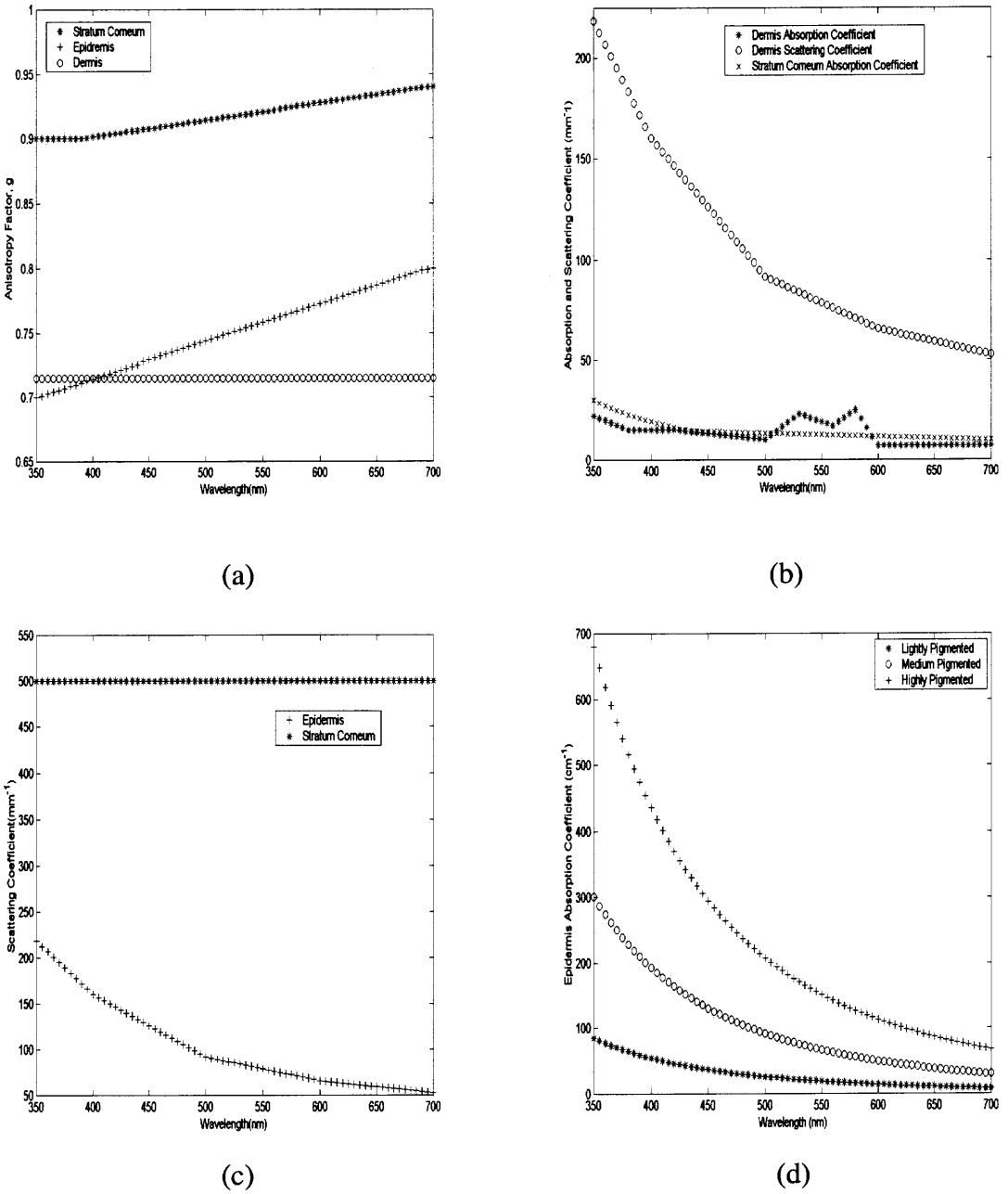

Figure 3.5. Compiled values of the optical properties: (a) anisotropy factor, g, as a function of wavelength for the stratum corneum and epidermis obtained from experimental results reported by Bruls [93] and for dermis obtained from data reported by Jacques, Alter and Prahl [95], (b) absorption coefficient for dermis from data reported by Gemert, Jacques, Sterenborg and Star [62], scattering coefficient for dermis from data reported by Cui and Ostrander [96] and absorption coefficient for stratum corneum from data reported by Gemert, Jacques, Sterenborg and Star [62], (c) scattering coefficient for stratum corneum and epidermis from data reported by Gemert, Jacques, Sterenborg and Star [62], and (d) absorption coefficient for the epidermis as a function of wavelength calculated using equations given by Jacques [81] for lightly pigmented, medium pigmented highly pigmented skin.

given by Jacques [81]. The three skin color types can also be classified as lightly pigmented, medium pigmented and highly pigmented. By combining the epidermal absorption coefficients obtained using Equations (3.20) - (3.22) for these three types of epidermal tissue with the values for the scattering coefficient and the anisotropy factor, 213 sets of values for the epidermal tissue are obtained. A different voxel type number is assigned to all these sets of optical properties. Thus, 71 different types of voxels for the stratum corneum, lightly pigmented, medium pigmented and highly pigmented epidermis and dermis each are formed. All these voxels put together form the voxel library with a total of 355 voxels.

3.2.4. Verification of the Algorithm

The first step in algorithm verification is to verify that the calculations and iterations preformed by the MCSVL code for the photon transport within the tissue and its interaction with the tissue are correct. For this purpose the tissue model and the optical geometry of Gardner [77] and Wang and Jacques [43] is used and simulation results are compared. They both used a three-layer tissue model with a point light source incident perpendicular to the skin surface and measured the total diffuse reflectance and transmittance. Gardner [77] used 100,000 photons in his simulations while Wang and Jacques [43] used 1,000,000 photons to test their Monte Carlo code, MCML. The optical properties and the layer thickness used in this three-layer model are given in Table 3.3. The refractive indices of the top and the bottom ambient media were set to 1.0.

Table 3.3 Optical Properties of the Three-layer Tissue Model

Layer	Refractive* Index n	Absorption Coeff. (cm-1)	Scattering Coeff. (cm-1)	Anisotropy Factor g	Thickness (cm)
1	1.37	1	100	0.9	0.1
2	1.37	1	10	0	0.1
3	1.37	2	10	0.7	0.2

The refractive indices of the top and the bottom ambient media are set to 1.0.

The same three-layer tissue model using voxel-based approach was setup. Cubical voxels with all dimensions equal to 0.01cm are used to generate the tissue material grid. Three types of voxels are used in this model, one for each layer. The optical properties used for these voxels are similar to the layers they represent and are given in Table 3.3. The dimensions of the tissue block simulated are 50cm x 50cm x 0.4cm. The number of voxels used in the x and y direction, i.e., along the surface of the tissue were 5000 each. Along the z direction, layers 1 and 2 have 10 voxels each while layer 3 has 20 voxels. This model was simulated using MCSVL for a point source with 500,000 photons incident perpendicular to the skin surface at the origin of the coordinate system. A detector array is placed at the top and bottom of the tissue block parallel to the tissue surface for collection. Total diffuse reflectance and transmittance are measured by calculating the total flux collected by the top and the bottom detectors respectively and then normalizing these values with the total number of incident photons.

A second simulation was done to check that the MCSVL code produced similar results independent of the voxel dimensions used. For this the voxel dimensions were changed to 0.02cm each side for the same tissue model given in Table 3.3 and it was again simulated it using the point source with 500,000 photons incident perpendicular to

the skin surface. Now the number of voxels used in the x and y direction i.e. along the surface of the tissue are 2500 each. Layers 1 and 2 have 5 voxels each and layer 3 has 10 voxels along the z direction. In order to study the change in the beam profile and the light diffusion within the tissue, for the same tissue model, a third simulation was done. The angle of incidence of the illuminating point source was changed so that it is at 45 degrees with respect to the tissue normal and the X-axis and is at 90 degrees with respect to the Y-axis. 500,000 photons were used in this third simulation also. For all these models contour maps of the energy distribution in the material grid along different horizontal tissue planes and the two vertical planes passing through the point of light incidence were used to check the beam profile and the uniformity of the light diffusion in the tissue.

Zeng et al. [97-98] have published diffuse reflectance data measured on Asian volunteers using their spectroanalyser system. They used two fused silica fibers having 1mm core diameter, one to deliver the illuminating light at 5 degrees and the other to collect the reflected light at 30 degrees with respect to the tissue normal. Diffuse reflectance values were measured over the wavelength range of 400-780nm. The next step of our algorithm verification is to develop a wavelength dependent tissue model using the voxel library and to simulate it using the optical geometry similar to the spectroanalyser system. The diffuse reflectance values were then estimated for various wavelengths and compared them with the experimental results published by Zeng et al.[97-98].

For spectroanalyser system optical geometry setup, a fiber optic cable with 1mm core diameter and a collection angle of 30 degrees with respect to the tissue normal are to be simulated. Light is conducted through an optical fiber only if it flows into the fiber within its acceptance angle θ_a [99]. The acceptance angle θ_a of the fiber is given by

$$\theta_a = \sin^{-1}\left(\frac{1}{n_0}\left(n_1^2 - n_2^2\right)^{1/2}\right) \tag{3.23}$$

where n_0, n_1 and n_2 are the refractive indices of the medium surrounding the fiber, the fiber core and the fiber cladding respectively. With air as the medium surrounding the fiber n_0 would be equal to 1. It was assumed that the fiber has a glass core with n_1 equal to 1.5 and a polymer cladding with n_2 equal to 1.47. This gives an acceptance angle of 17.4 degrees. A circular disc with 1mm diameter is placed on the tissue surface with an angle of 30 degrees between the axis normal to the disc and the tissue normal (Z-axis) to simulate the collecting optical fiber. Any photon escaping the tissue surface and hitting the disc with an angle less than 17.4 degrees with respect to the disc normal will be conducted through the optical fiber. Weight of all such photons is accumulated towards the total diffuse reflectance. A point source incident at an angle of 5 degrees with respect to the tissue normal is simulated by choosing the initial direction cosines μ_x, μ_y and μ_z of the photon beam equal to 0.08716, 0 and 0.9962 respectively. This point source is incident at the origin of the coordinate system, which is also the focus of the collection fiber.

A three-layer tissue model is used with the stratum corneum of 50μm, epidermis of 100μm and dermis of 200μm in thickness. For the epidermis there are three types of voxels in the voxel library according to the level of pigmentation. Out of these lightly pigmented, medium pigmented and highly pigmented epidermal voxels; the medium pigmented type voxels are used in this model. Thus, a medium pigmented or Asian skin type model was formed. By replacing the medium pigmented epidermal voxels in the

Asian skin type model with the lightly pigmented and highly pigmented epidermal voxels, white and black color skin type models were formed respectively.

For all these models, the dimensions of the tissue block used were 5cm x 5cm x 0.035cm. Cubical voxels with each side equal to 10μm were used, forming the material grid array of 5000 voxel x 5000 voxel x 35 voxel. As explained in Section 2.2, for all the three skin layers there are 71 voxel types each in the voxel library corresponding to the 71 different wavelengths in the range of 350-700nm with an interval of 5nm. Let's say for the stratum corneum we have voxel type number 1 corresponding to 350nm wavelength, voxel type number 2 corresponding to 355nm wavelength and so on. When simulating the tissue with a 350nm wavelength, we use voxel type number 1 to form the stratum corneum material grid and change it to voxel type number 2 for a 355nm wavelength. Thus voxels having the optical properties of the tissue at a particular wavelength are used to form the material grid when the tissue model is to be simulated using that particular wavelength. In this way three-layer wavelength dependent tissue models are obtained.

These models were simulated using a point source with 100,000 photons each for all the wavelengths. The total diffuse reflectance was estimated by normalizing the total diffuse flux collected with the total number of photons used in the simulation for every wavelength. The variance of the simulation results can be minimized either by using a large number of photons or by carrying out multiple independent simulations and averaging the results of all these simulations. The latter method for variance reduction is chosen. Results were obtained by taking the average value of diffuse reflectance from three independent runs for each wavelength.

3.2.5 Skin Lesion models

Models of nevus, cylindrical in shape having 5mm and 3mm diameters and depths of 10μm, 20μm, 40μm, 60μm, 80μm and 100μm were developed. Cubical voxels with each side equal to 10μm were used in these models. For the 5mm diameter skin lesions models, a 4mm diameter cylinder was formed using highly pigmented epidermal voxels while the outer ring of 0.5mm was formed by randomly distributing the medium and lightly pigmented epidermal voxels as shown in Figure 3.6. In this figure the highly pigmented epidermal voxels are represented by the black pixels, medium pigmented epidermal voxels by the dark gray pixels and lightly pigmented epidermal voxels by the gray pixels. The 3mm diameter skin lesion models were similarly formed using a 2.4mm diameter the inner cylinder with highly pigmented epidermal voxels and the outer ring of 0.3mm formed by randomly distributing the medium and lightly pigmented epidermal voxels. The ratio of the highly pigmented region diameter (inner cylinder) and the nevus diameter are same for both the models. Using 1, 2, 4, 6, 8 and 10 such voxel layers along the z direction formed the nevus models with different depths. These nevus models were incorporated in the epidermal layer of the lightly pigmented skin type model to form the models of skin lesions with a white color surrounding skin. The skin lesion models were simulated using the optical geometry of the Nevoscope [14-15] to obtain the estimates of the total diffuse reflectance. Diffuse reflectance values were measured for optical wavelengths with an interval of 5nm over the range of 350-700 nm.

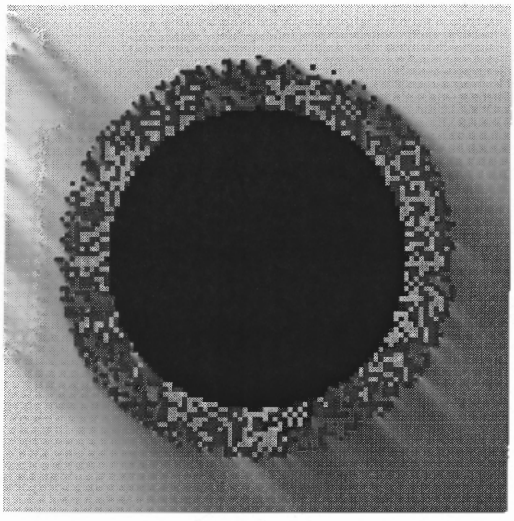

Figure 3.6 Nevus with surrounding white skin: formed using the lightly pigmented, medium pigmented and highly pigmented epidermal voxels.

3.2.6 Nevoscope Optical Geometry

A drawing of the Nevoscope is shown in Figure 3.7. The light source used with the Nevoscope is a halogen lamp with variable intensity control. The light is channeled through the trans-illumination fibers to the light ring in the front of the Nevoscope where it is directed onto the skin at 45 degrees. The surface imaging of the skin is achieved by using the surface illumination fibers. The combination of simultaneous trans-illumination and surface illumination produces epiluminesence imaging of skin lesions. The images are recorded using a digital camera with interchangeable magnification lenses.

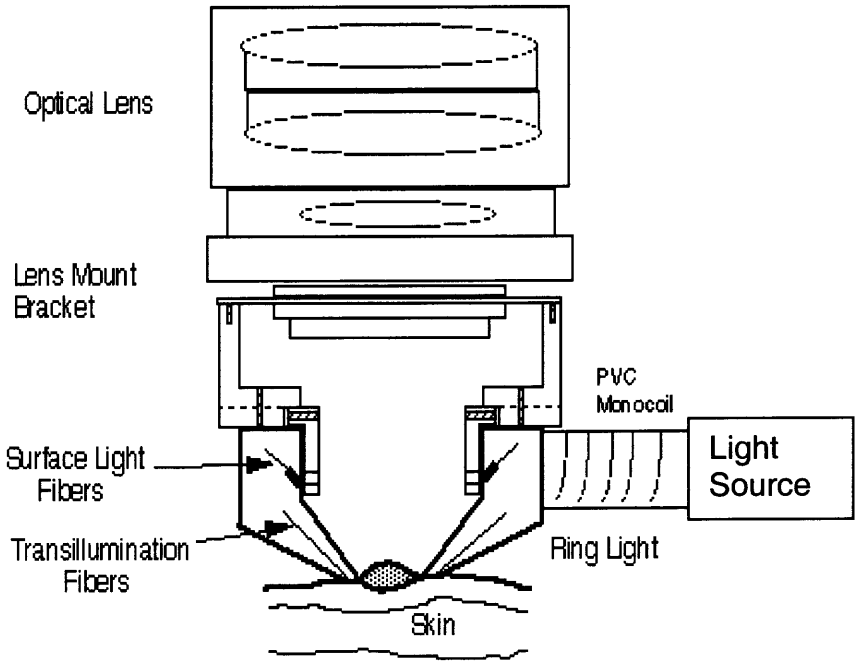

Figure 3.7 Nevoscope

To approximate the ring light of the Nevoscope, 72 point sources located on the circumference of a circle, 5 degrees apart, were used in the simulations. Ring light sources with 2cm and 1.8cm diameters were formed in this manner. All the point sources had an angle of incidence of 45 degrees with respect to the tissue normal, so as to form a cone shaped beam. A 2cm x 2cm detector was placed parallel to the tissue surface and 2cm above it, such that the detector and the ring light axis coincided. This detector represents the CCD array of the digital camera.

The 5mm diameter nevus models were simulated using the 2cm diameter ring light source. To verify the results obtained using the 5mm diameter nevus models, the 3mm diameter nevus models were simulated using the same ring light source. Both the 5mm and 3mm diameter nevus models were also simulated using the 1.8cm diameter ring light source in order to study the effect of varying the source distance from the nevus periphery.

The models of different skin types based on their epidermal melanin concentration described earlier were also simulated using the Nevoscope optical geometry in order to estimate their diffuse reflectance spectra. 125,000 photons per point source of the Nevoscope optical geometry setup were used in all the simulations. The tissue reflectance as a function of wavelength was measured for all the tissue models with an interval of 5nm for the optical range of 350-700nm. The diffused reflectance values were obtained by normalizing the total flux collected by the detector with the total number of photons used in the simulation.

3.2.6.1 Simulations Of Tissue Models. The skin lesion models described above and the models of different skin types based on their epidermal melanin concentration were simulated using the Nevoscope optical geometry. For the Nevoscope, 100,000 photons per point source approximating the Nevoscope optical geometry were used in all the simulations. The skin lesion models were also simulated using the optical geometry of the spectroanalyser system [97-98]. 100,000 photons were used in all the simulations with the spectroanalyser system. For the spectroanalyser system simulations, three independent runs using 100,000 photons each were done. The tissue reflectance as a function of wavelength was measured for all the tissue models with an interval of 5nm for the optical range of 350-700nm. The diffused reflectance values were normalized by dividing the total flux collected by the detectors by the total number of photons used in the simulation. For the spectroanalyser system, results were obtained by taking the average of the diffuse reflectance values obtained from the three independent simulations.

3.2.6.2. Wavelength Selection By Correlation Analysis. For two random variables X and Y the correlation coefficient is defined by

$$\rho_{X,Y} = \frac{COV(X,Y)}{\sigma_X \sigma_Y} = \frac{E\left[\left(X - E[X]\right)\left(Y - E[Y]\right)\right]}{\sigma_X \sigma_Y} \tag{3.24}$$

where COV(X,Y) is the covariance of X and Y, E[.] represents the expected value of the variable and E[X], σx and E[Y], σy are the expected values and standard deviations of X and Y respectively [100]. The correlation coefficient is a number that is at most 1 in magnitude. The extreme values of ρx,y are achieved when X and Y are related linearly i.e. Y=AX + B. ρx,y is equal to 1 if A is greater than zero and is equal to -1 if A is less than zero. ρx,y can be viewed as a statistical measure of the extent to which Y can be predicted by a linear function of X. Variables X and Y are uncorrelated if ρx,y equals zero [100].

Four different sets of simulations were conducted using a combination of skin lesion models and ring light source with different diameters. The different combinations used were: 5mm diameter skin lesion and 2cm diameter ring light, 5mm diameter skin lesion and 1.8cm diameter ring light, 3mm diameter skin lesion and 2cm diameter ring light and 3mm diameter skin lesion and 1.8cm diameter ring light. In each set of simulations lesion models with different depths were simulated using optical wavelengths with an interval of 5nm over the optical range of 350-700nm. Since there are 6 different lesion depths, 6 simulations were performed in each set. The measured diffuse reflectance values from a particular set of simulations were grouped together in to arrays according to the wavelengths used in the simulation. Say for the set of 5mm diameter skin lesion with a 2cm diameter ring light, models with 10, 20, 40, 60, 80 and 100 μm lesion depth

were simulated. Then the array DR1 corresponding to 350nm wavelength will have the diffuse reflectance values corresponding to the 5mm diameter skin lesion models with increasing depth. Since 6 different lesion depths were used, every set will have 6 diffuse reflectance values. 71 such sets were formed for wavelengths with an interval of 5nm over the optical range of 350-700nm. Another set ND was formed containing the values of the nevus depths. Using DRj ($1 \leq j \leq 71$) and ND as the variables, correlation coefficient values Cj ($1 \leq j \leq 71$) were calculated for all the sets of simulations. A correlation coefficient threshold, CT was set equal to 0.7. Wavelengths for which the absolute value of the correlation coefficient was greater than CT were obtained for the 5mm and 3mm diameter nevus models simulated with a 2cm diameter ring light source. Out of these, wavelengths that were common for both the models were selected for the multi-spectral imaging of the skin lesions. The effect of changing the ring light source diameter was studied by comparing the results with those obtained from the 5mm and 3mm diameter nevus models simulated with a 1.8cm diameter ring light source.

3.3 Multi-spectral Image Analyses

Multi-spectral trans-illuminance images of skin lesions of individuals from various age groups and gender were collected using the Nevoscope [14-15]. A 100W halogen light source along with narrow band-pass interference filters of the wavelengths selected from the mathematical modeling of light-tissue interaction were used for illumination. Images were collected with an Agfa digital camera (ePhoto-1280) and were 16-bits, 1024 x 768 pixels in size. The lesion images were collected over a period of two years by imaging suspicious lesions on 250 individuals under the observation of a cancer specialist. From

these image data, 30 cases of melanoma were confirmed by biopsy and histological examination. These cases were split into two sets for classification. The learning (known) set consisted of 15 cases of melanoma and 15 cases of dysplastic nevus. The testing (unknown) set used in the classification consisted of 15 cases of melanoma and 45 cases of dysplastic nevus. For each case the image set consist of three images namely, epi-illuminance image obtained using a white light source, trans-illumination image obtained using 580nm wavelength source and trans-illumination image obtained using 610nm wavelength source. The trans-illumination image obtained using 510nm wavelength source was not used in this study since it produces a non-uniform illumination of the skin lesion thus forming a dark spot at the center of the image. Figure 3.8 shows a sample set of multi-spectral images from the database. The ADWAT classification method was extended to analyze the multi-spectral trans-illuminance images as described below.

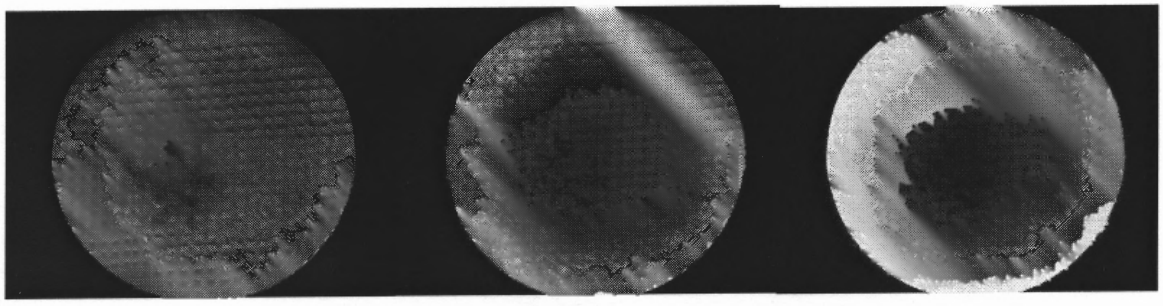

(a) (b) (c)

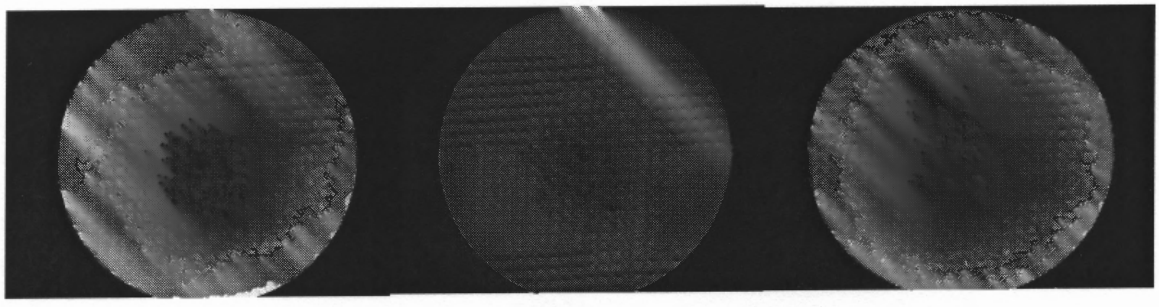

(d) (e) (f)

Figure 3.8 Multi-spectral images: (a) surface image, (b) trans-illumination, (c) 510nm, (d) 580nm, (e) 610nm and (f) normal skin.

3.3.1. Feature Set

Features were derived from the multi-spectral images using similar analysis that was used in the ADWAT classification method. All images of a particular wavelength from the learning set are decomposed up to three levels in Matlab using the Daubechies-3 (db3) wavelet. After the channels are decomposed their mean energy is calculated using Equation (3.1). Channel energies and various ratios of channel energies similar to those given in Table 3.1 are used as features. Statistical analysis is used to reduce the dimensions of the feature space by selecting on those features that produce a bi-modal distribution between the two image classes, namely, melanoma and dysplastic nevus. For all these features energy thresholds were obtained in the same manner as described in Section 3.1.4. All pooled feature values that generated unimodal distributions were rejected. Features were obtained for the 580nm and 610nm wavelength images. These features were combined with the features obtained from the epi-illuminance images to form the feature set.

3.3.2. Classification Using Extended-ADWAT Method

The Extended-ADWAT method is a two-step classification process. In the first step only the epi-illuminance images are used and classification is carried out in the same manner as the ADWAT method described in Section 3.1.4. The only difference between the first step of the Extended-ADWAT method and the ADWAT method is, instead of having only two image classes, the Extended-ADWAT method has three image classes. Images are now classified as melanoma, dysplastic nevus or suspicious lesion. In the ADWAT method all the images that produced a tree structure similar to the tree structure model of the dysplastic nevus were assigned to the dysplastic nevus image class and the rest were

assigned to the melanoma image class. In the Extended-ADWAT method images are classified as melanoma only if the tree structure completely matches the melanoma tree structure model. All the images that produce incomplete tree structures are assigned to the suspicious lesion class. The multi-spectral trans-illuminance images of these skin lesions are then analyzed in the second step of the classification process. The following procedure is involved in classification at this step:

a. Decompose the epi-illuminance image using the threshold-based algorithm.

b. Count the number of channels (CV_1) that satisfied the energy threshold criteria and were decomposed further.

c. If CV1 = 1 then image is assigned to the Dysplastic nevus class.
If $CV_1 = 6$ then image is assigned to the Melanoma class.
If $1 < CV_1 < 6$ then image is assigned to the suspicious lesion class.

d. Suspicious skin lesion images are further analyzed in the second step of the classification process.

In the second step of the classification process multi-spectral trans-illuminance images of the suscipious lesions are analyzed. The following procedure is involved in this setp:

a. The multi-spectral trans-illuminance images of all the skin lesion that are marked as suspicious in the first step of the classification are decomposed up to 3 levels using db3 wavelet.

b. Channel energies or energy ratios are calculated for all the channels for which bimodal distribution was obtained during the learning phase and thresholds were calculated.

c. Total number of channels (CV_2) that satisfy their respective energy threshold criteria from both the multi-spectral images is calculated. If all the energy threshold criteria were satisfied then the value of CV_2 would be equal to the maximum value CV_{max}.

d. Melanoma probability (MP) is calculated as the ratio CV_2 / CV_{max}.

e. For the value of MP greater than or equal to Melanoma Probability Threshold (MPT) the lesion is classified as melanoma otherwise it is classified as a dysplastic nevus.

3.3.3. Classification Using Fuzzy Membership Functions

Conventional classification approaches always assign a new unidentified object into exactly one category by means of classifier constructed from the training data set. Even though they are suitable for various applications and have proven to be an important tool, they do not reflect the nature of human concepts and thoughts, which tend to be abstract and imprecise. In real world, to set a crisp boundary often makes the result intuitively unreasonable. If the selected features have an overlapping distribution among the classes, introduction of fuzzy logic for classification becomes necessary. Another better justification for employing fuzzy logic is to represent via membership functions the extent to which a candidate belongs to the different classes [104].

A fuzzy set is a set without a crisp boundary. If O is a collection of objects denoted generically by X, then a fuzzy set A in O is defined as a set of ordered pairs:

$$A = \{(x, \mu_A(o)) \mid o \in X\} \tag{3.25}$$

where $\mu_A(o)$ is called the membership function (MF) for the fuzzy set A and its value ranges from 0 to 1. In short, a membership function can be viewed as a curve that defines how each point in the input space is mapped to a membership value (or degree of membership) between 0 and 1. The input space, or O in the definition, is sometimes referred to as universe of discourse, which may consist of discrete objects or continuous space. The classes of parameterized functions used to define membership functions include the following: Triangular MF, Trapezoidal MF, Gaussian MF and Bell MF.

Since it was assumed in the ADWAT classification method that the bi-modal features have a gaussian distribution, multi-dimensional Gaussian and Bell membership functions are formulated for each image set class using the same features that were used in the extended ADWAT method. Conclusions are drawn regarding the best choice for the membership function profile by comparing the classification results obtained using the Gaussian membership function with those obtained using the Bell membership function.

A one-dimensional Gaussian MF is defined as

$$Gaussian(x;a,b) = e^{-1/2[(x-a)/b]^2} \tag{3.26}$$

Parameter a decides the center of the Gaussian MF while parameter b decides its spread. Figure 3.9 shows the variation of the Gaussian MF with respect to these parameters.

A one-dimensional Bell MF is defined as

$$Bell(x,a,b,c) = 1/\left(1+\left|[(x-a)/b\right|^{2c}\right) \tag{3.27}$$

As in the Gaussian MF, parameters a and b decide the center and spread of the Bell

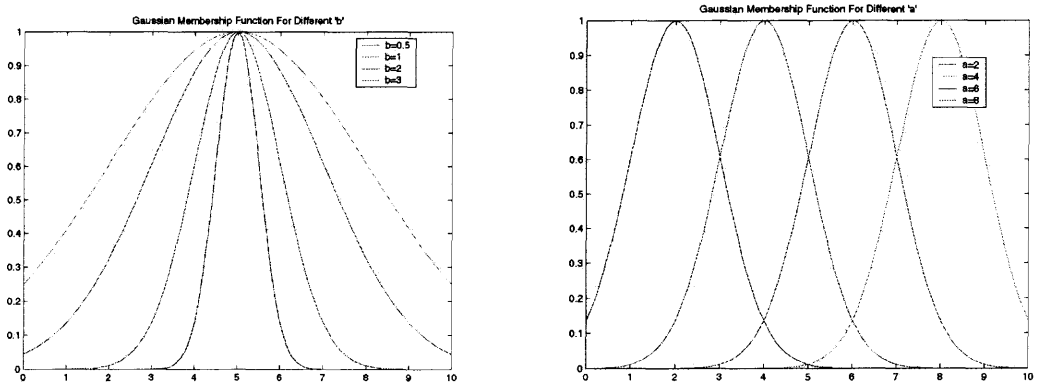

Figure 3.9 Gaussian Membership Function.

MF respectively. Parameter c decides the roll-off after the cutoff points. Figure 3.10 shows the variation of the Bell MF with respect to these parameters.

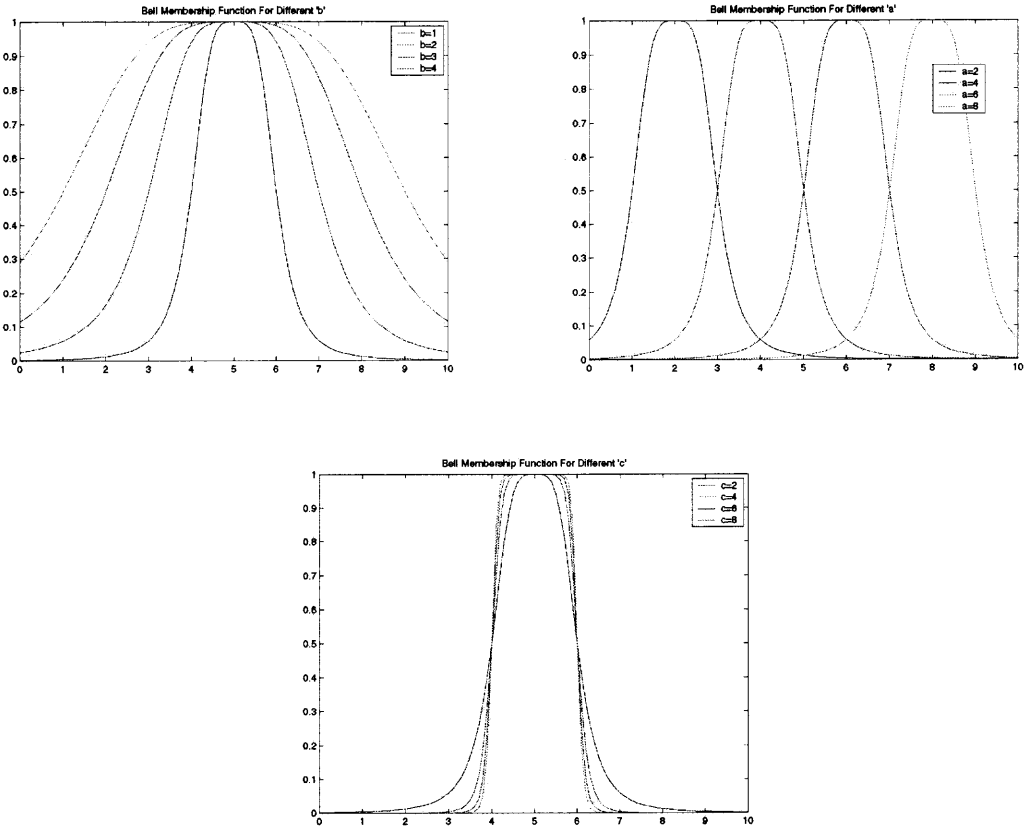

Figure 3.10 Bell Membership Function.

In order to handle the combined features obtained from the epi-illumination and multi-spectral trans-illumination images, the single dimensional Gaussian MF given in Equation (3.26) is extended to multi-dimensional Gaussian MF. Since all the features are correlated to each other, the formula for the probability density function of n jointly Gaussian random variables is used as the Gaussian MF. The membership function is calculated using the formula

$$\mu_A(x) = gaussian(X; M_A, K_A) = \exp\left\{-1/2(X - M_A)^T K_A^{-1}(X - M_A)\right\} \tag{3.28}$$

The same theory is extended to formulate a multi-dimensional Bell MF, which is given by

$$\mu_A(X) = bell(X; M_A, K_A, N_A) = 1/\left\{1 + \left[(X - M_A)^T K_A^{-1}(X - M_A)\right]^{N_A}\right\} \tag{3.29}$$

where subscript A represents different class or category and in our case it is Melanoma (m) or Dysplastic (d); the image category.

$X = [x_1, x_2, ...x_n]^T$ and $M = [m_1, m_2, ...m_n]^T = [E(x_1), E(x_2), ...E(x_n)]^T$. X is the feature vector and m_i is the mean value of feature x_i. K is covariance matrix of features x_i, which is defined as

$$K = \begin{bmatrix} \text{var}(x_1) & \text{cov}(x_1, x_2).... & \text{cov}(x_1, x_n) \\ \text{cov}(x_2, x_1) & \text{var}(x_2).... & \text{cov}(x_2, x_n) \\ \text{cov}(x_n, x_1) & \text{cov}(x_n, x_2).... & \text{var}(x_n) \end{bmatrix} \tag{3.30}$$

The third parameter, N_A, of the Bell MF is taken as a function of the difference between the values of the covariance determinants for the two image classes as given bellow

$$\begin{aligned} N_m &= S\{\,|K_m| - W(|K_m| - |K_d|)\} \\ N_d &= S\{\,|K_d| - W(|K_d| - |K_m|)\} \end{aligned} \tag{3.31}$$

where S and W are constants. S is the scaling factor so as to make N_A greater than or equal to two and W is the weighing factor chosen to keep the value of N_A positive. Thus

the shape of the Bell MF for the two classes will be the same only if their covariance matrices are the same.

The values of the parameters defining the membership functions are calculated using the learning data set. These values are used in Equations (3.28) and (3.29) to formulate the Gaussian and the Bell membership functions respectively. The value of scaling constant S in Equation (3.31) was taken equal to 10^{23} and N_A was calculated for different discrete values of weighing constant W. During the classification phase, for a candidate image the feature vector X is obtained using wavelet decomposition and channel energy feature calculations. This X is then plugged in to Equations (3.28) and (3.29) respectively to calculate the membership function values for the melanoma and dysplastic nevus image class. The candidate image is then assigned to the image class with higher membership function value using the criteria 'winner takes all'.

CHAPTER 4

RESULTS AND DISCUSSION

4.1 Classification Of Skin Lesion Images

The diagnostic accuracy of a test is measured by the sensitivity and specificity of correct classification [101]. For the classification of skin lesions in this study, the sensitivity, or true positive fraction (TPF), indicates the fraction of melanoma lesions correctly classified as melanoma. The specificity, or true negative fraction (TNF), indicates the fraction of dysplastic or non-melanoma lesions correctly classified as non-melanoma. The relationship between sensitivity and specificity calculated for all possible threshold values of the discriminant function, or for this case the threshold constant, is represented graphically as the Receiver operating characteristic (ROC). The vertical axis of the graph represents the sensitivity or TPF, while the horizontal axis represents the false-positive fraction, FPF, which is 1-TNF [101]. Results obtained from the ADWAT classification method are presented and are then compared with those obtained using the method proposed by Chang and Kuo [34].

4.1.1 Results of the ADWAT Classification Method

For the tree structure development, 11 features were considered for each channel decomposed. From these features, threshold values were calculated for those features that segregated into bimodal distributions between lesion classes. If more than one feature within a particular channel segregated between lesion classes, then the feature for which the separation between the mean values of the two classes was maximum compared to the variance of each class was used in the analysis. The feature set and threshold values used

in the development of the tree structure are summarized in Table 4.1. For channels 1 and 4, all features generated unimodal distributions and were not decomposed further or used for classification.

Table 4.1 Features Obtained for the ADWAT Classification Method

Channel	Energy feature	Distribution type Separable/bimodal	Threshold for decomposition
2	e2/e1	Bimodal	> 0.0366
3	e3/e1	Bimodal	> 0.043
2.1	e2.1/(e2.2+e2.3+e2.4)	linearly separable	> 0.34
3.1	e3.1/(e3.2+e3.3+e3.4)	linearly separable	> 0.315
2.1.4	e2.1.4/e2.1.1	linearly separable	< 0.837

1. Selected features obtained from a statistical analysis were either linearly separable or segregated bimodally between classes.
2. The channel, corresponding energy feature ratio, and the threshold values obtained for maximum separation of the two classes are given.

Feature data values used to generate the threshold values given in Table 4.1 are illustrated in Figure 4.1. Channels 2 and 3 had bimodal feature segregation, but the clusters were not linearly separable. Thresholds were obtained for these channels by averaging the means of the features for the two lesion classes. This method of threshold selection is illustrated for channels 2 and 3 in Figure 4.1 a-b. For channels 2.1, 3.1, and 2.1.4, the feature data between the melanoma and dysplastic nevus classes segregated into linearly separable classes. These data are illustrated in Figure 4.1 c-e. Thresholds for these data were selected by averaging the highest value from the lower valued class with the lowest value from the higher valued class.

No features from channel 1 or channel 4 and any of their sub-images segregated into bimodal distributions between the image classes. Since these features contained no

discrimination value, further decomposition of these channels was stopped. For classification of candidate images, decomposition of each channel was determined based on the value of a specific feature and the feature threshold value given in Table 4.1. The resulting tree structure signatures of melanoma and dysplastic nevus are shown in Figure 4.2. Note that for melanoma, only channels 0, 2, 3, 2.1, 3.1 and 2.1.4 are decomposed.

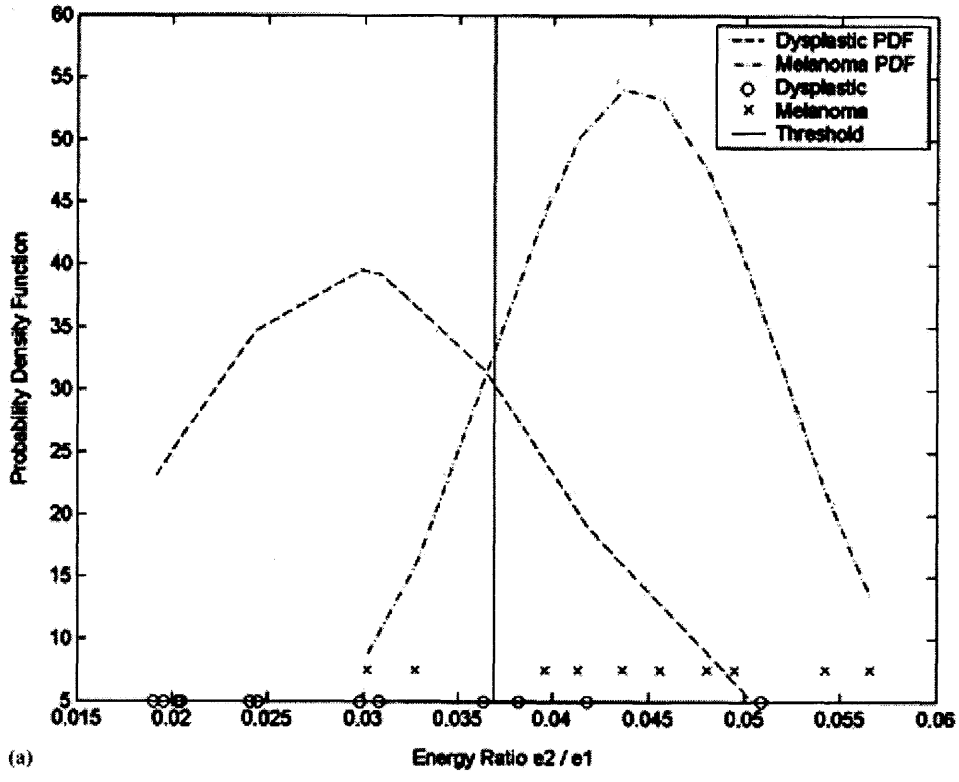

(a)

Figure 4.1 Feature data values for dysplastic and melanoma training data. Scatter plots and thresholds are shown for features selected for channels: (a) 2, (b) 3, (c) 2.1, (d) 3.1, and (e) 2.1.4. Threshold values used to separate classes are shown as a dotted vertical line in (a)-(b) and as dotted horizontal lines in (c)-(e).

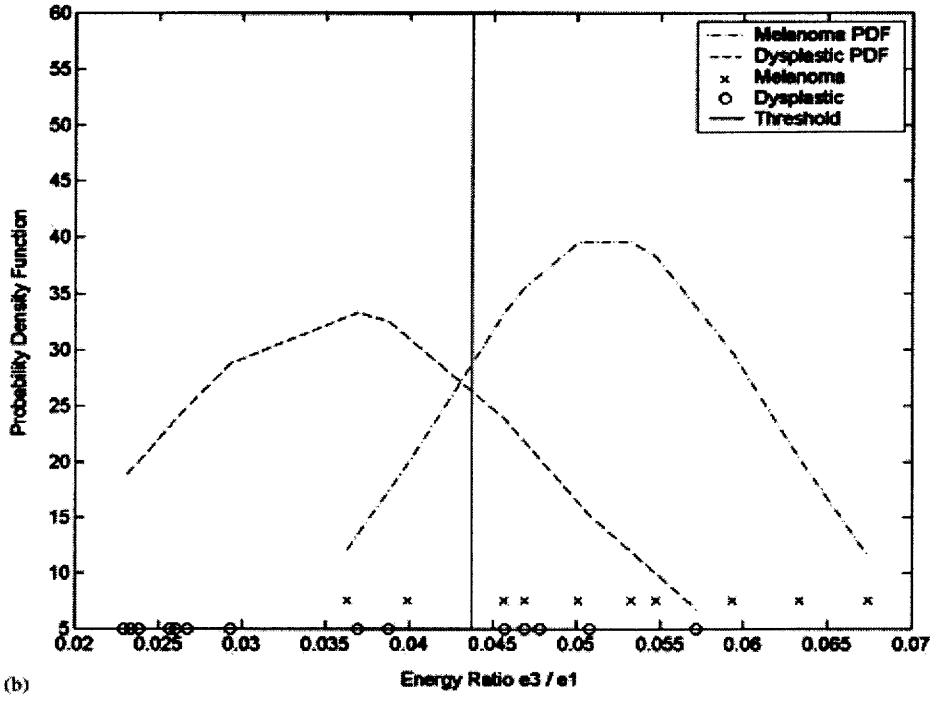

(b)

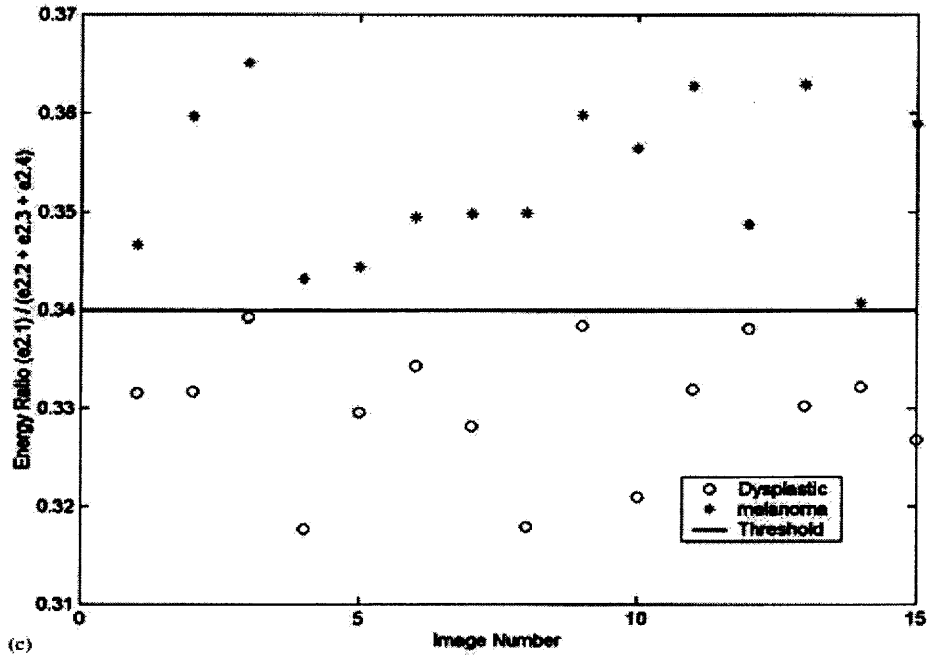

(c)

Figure 4.1 (Continued)

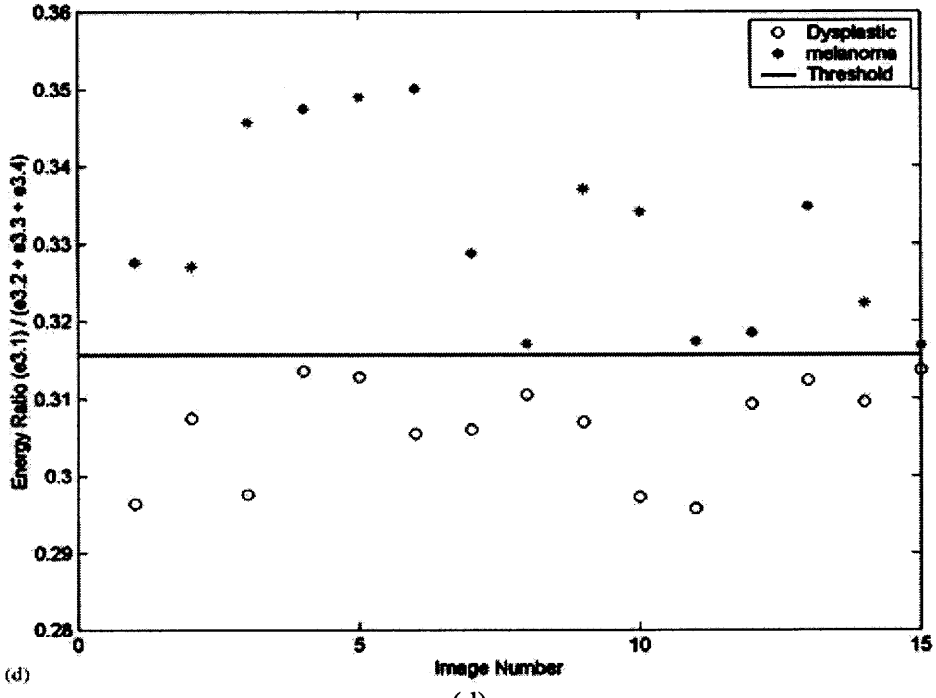

(d)

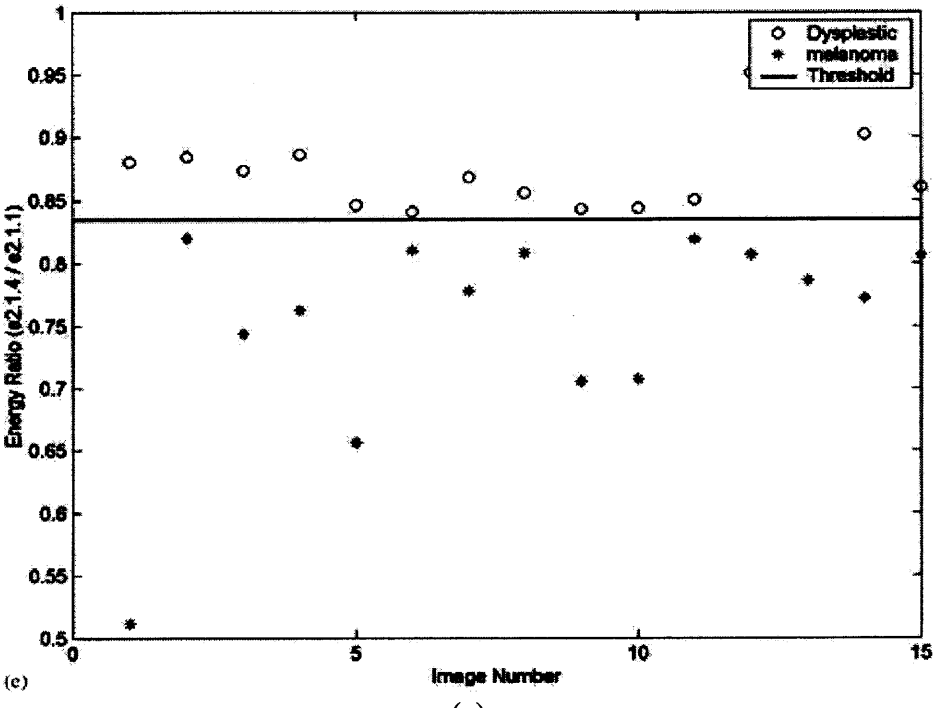

(e)

Figure 4.1 (Continued)

The decomposition of all the other channels was stopped since these features produced unimodal distributions between the lesion classes. Also note that due to the selection of the thresholds, the algorithm does not decompose dysplastic nevus images beyond the first level. A dysplastic nevus will thus generate a tree structure with only one level of decomposition as shown in Figure 4.2 b.

The results of the classification of the test data using the ADWAT method are summarized in Table 4.2. For the ten images of melanoma used during the classification phase, the algorithm was able to correctly classify nine images to the melanoma nevus class. Histological evaluation had confirmed that all of these ten lesions were melanoma.

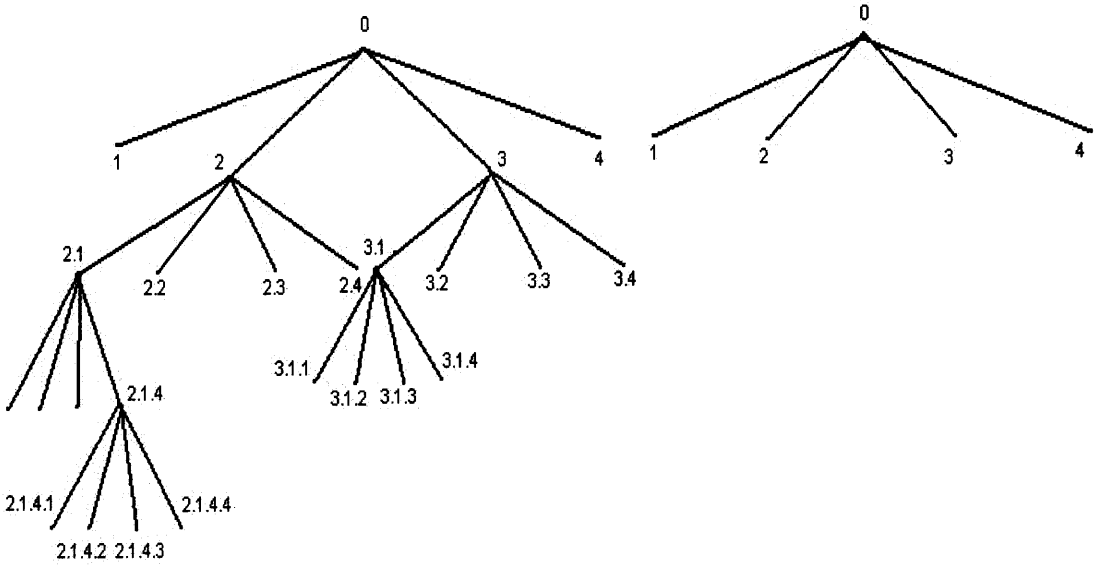

Figure 4.2 Tree structure signatures: (a) melanoma and (b) dysplastic nevus. Based on the threshold values given in Table 3.3, several channels are decomposed for the melanoma creating a distinct tree structure. The dysplastic nevus is not decomposed beyond the first level because of the selection of the threshold values.

For the 20 images of dysplastic nevus, 18 were correctly classified to the dysplastic nevus class while two images were incorrectly classified to the melanoma nevus class. The resulting true positive fraction (TPF) obtained for this classifier was 90% with a false positive fraction (FPF) of 10%.

4.1.2 Classification Results By Constant Threshold Method

The results from this classification method are summarized in Table 4.3. The number of melanoma and dysplastic nevus correctly classified and the resulting TPF and FPF are given. The resulting ROC curve obtained for the tree structure wavelet transform analysis method is shown in Figure 4.3. This tree structure method gives a maximum true positive value of 70% and a false positive value of 20% for a threshold constant value of 0.026.

Table 4.2 Summary of the Test Data Classified Using the ADWAT Method

Lesion type	Number classified	CV	Classification	Channel decomposition error
Melanoma	8	6	Melanoma	---
Melanoma	1	5	Melanoma	no decomposition of 3.1
Melanoma	1	1	Dysplastic	no decomposition of 2, 3
Dysplastic	18	1	Dysplastic	---
Dysplastic	2	2	Melanoma	decomposition of 2

Note: The lesions with a value of the classification variable (CV) greater than 1 are classified as melanoma; those with CV equal to 1 are classified as dysplastic nevus. The resulting TPF is 90% with a FPF of 10%.

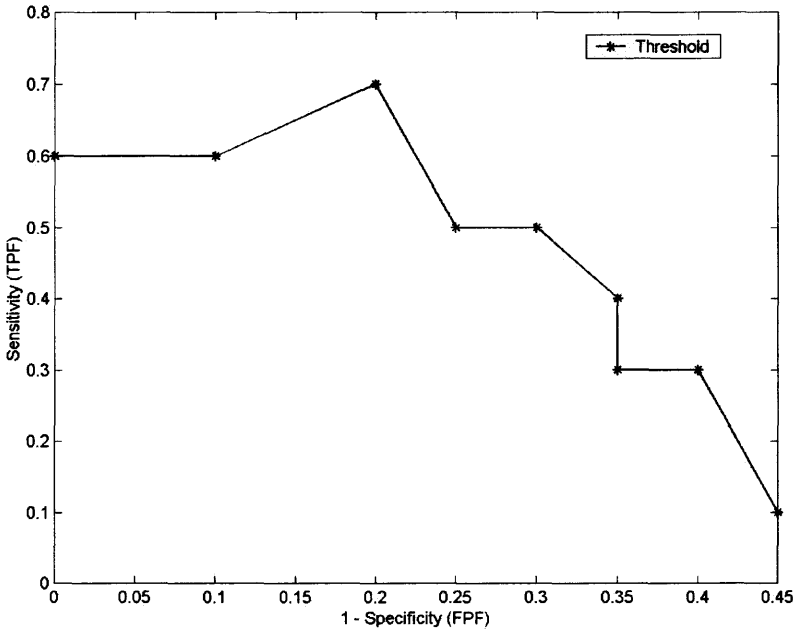

Figure 4.3 ROC curve for the classification using constant threshold method. The maximum sensitivity of 70% correct diagnosis of melanoma occurs with a false diagnosis of melanoma of 20%. Each data point represents a different value of the threshold constant.

The different threshold constant values selected dictated the number of channels that were decomposed. For high values of the threshold constant only the channel 1 energy ratio was high enough to meet the energy ratio criteria for decomposition. However, as the threshold constant value was decreased, other channel energy ratios satisfied the threshold and were decomposed. Increasing the number of decomposed channels does not necessarily add useful information to the discrimination, as the dominant energy channels may remain the same. As shown in Figure 4.3, the ROC curve shows a peak in sensitivity for an intermediate value of the threshold constant and number of channels decomposed. This method with a constant threshold value has both a smaller sensitivity and a smaller specificity than the ADWAT method presented in the

previous section. Thus, by adaptively selecting the threshold based on the discrimination content of the data, a better classification can be achieved with the same data.

4.1.3 Result Analysis and Discussion

In this section, the advantage of adaptively selecting the threshold values for image decomposition is discussed in relation to the energy distribution and the information within the channels. Result analysis and interpretation are also presented followed by pointing out the potential applications of the ADWAT method.

4.1.3.1 Threshold Selection. For the epiluminesence images used in this study, the energy is non-uniformly distributed among the channels. At the first level of decomposition, the image total energy is distributed with about 82-87% in channel 1, 3-4% in channel 2, 4-5% in channel 3 and 4-11% in channel 4. The energy in channel 1, the low-low frequency channel, primarily corresponds to the skin surrounding the lesion and is of no significance in the lesion classification. Channels 2 and channel 3, the mid frequency channels, correspond to the nevus-skin boundary and some portions of the nevus itself. These two channels are important from the classification point of view as they contain most of the information that would allow discrimination between lesions according to the ABCD rule. The energy in channel 4, the high-high frequency channel, corresponds to portions of the lesion boundary where the boundary is well defined and also to regions of uneven reflection from the surface due to air gaps and skin layering.

In the method proposed by Chang and Kuo [34], a threshold value is selected and the ratio of channel energy to maximum channel energy within a decomposition level is calculated. The decomposition of channels 2 and 3, which contain most of the relevant discrimination information, is dependent on the value of the threshold constant. Selecting

a threshold constant value higher than the average e2/e1 or e3/e1 energy ratio for a lesion class will thus result in a loss of this information. For the test images, an e3/e1 ratio of 0.043 and an e2/e1 ratio of 0.0366 optimally segregate the melanoma and dysplastic nevus classes. For a threshold value greater than this e3/e1 ratio value, the tree structure developed for many candidate melanoma images results in decomposition of only the low-low frequency channel. This method will thus produce identical tree structure and energy maps for the melanoma and dysplastic image classes, resulting in nearly all the images from the data set being classified as dysplastic. For values of the threshold constant below 0.043, the tree structure and the energy maps are highly dependent on the value of the threshold constant. Hence, rather than randomly selecting a threshold value without any criterion, this classification could be improved by using an adaptive method for selecting the threshold value.

Obtaining the threshold values from a statistical analysis of the channel energies and their ratios provides the required adaptivity to the tree structure development. Statistical selection of the thresholds at each level of decomposition makes the ADWAT method more robust and a good candidate method for surface characterization and texture representation. It should be noted that since the thresholds were obtained from bimodal distributions, reversing the inequalities on the thresholds would reverse the tree structure signatures developed for the two classes. The dysplastic nevus was a logical choice as a basis for classification instead of the melanoma since more dysplastic nevus data was available. The number of images used during the learning phase is the same for both the classes, although the number of dysplastic nevus images used in the classification phase

is more. Also the natural population of dysplastic nevus class is very large compared to melanoma, hence no risk of obtaining any bias is seen.

4.1.3.2 Analysis of ADWAT Classification. In the ADWAT method, it is necessary for either channel 2 or channel 3 to be decomposed in order to generate a value of CV > 1 and to classify a lesion as melanoma. A summary of the decomposition of the test images is given in Table 4.3. Among the nine images classified as melanoma, eight images developed the complete tree structure signature of melanoma with the value of CV equal to 6. The remaining image correctly classified as melanoma produced a value of CV equal to 5, failing to decompose channel 3.1. The melanoma image that was misclassified as non-melanoma is shown in Figure 4.4. This lesion is a late stage melanoma that was easily diagnosed by the physician. As can be seen in the image, a significant amount of reflection is contained in the image as a result of flaking skin on the lesion and skin surface. As a result, more energy was distributed in channel 4, while the energy in channels 2 and 3 decreased below the threshold values needed for decomposition. The algorithm failed in this case due to this change in the energy distribution. The imaging artifact resulting from non-uniform reflection can be minimized by use of a polarizing filter or by applying a lotion to the skin prior to imaging to minimize refractive index mismatch.

The two images of dysplastic nevi that were incorrectly classified as melanoma were decomposed beyond the first level. For both of these images, channel 2 was decomposed one level. These images produced a value of CV equal to 2 and were thus classified as melanoma. The tree structure developed for these two images is different

from the tree structure signature of melanoma since channels 2.1, 2.1.4, 3, and 3.1 were not decomposed.

Table 4.3 Classification Using the Constant Threshold Method. The results obtained from the tree structure wavelet transform analysis method are given for a range of threshold constant values. The highest correct classification of melanoma occurs for a threshold constant of 0.026.

Threshold constant	Melanoma correctly identified, TP (n=10)	Dysplastic nevus correctly identified, TN (n=20)	TPF	FPF
0.018	6	20	60	0
0.022	6	18	60	10
0.026	7	16	70	20
0.030	5	15	50	25
0.034	5	14	50	30
0.038	4	13	40	35
0.042	3	13	30	35
0.046	3	12	30	40
0.050	1	10	10	50

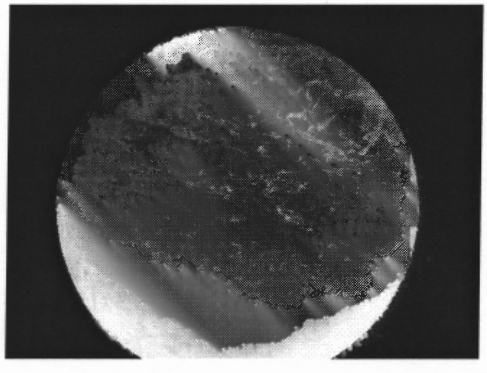

Figure 4.4 Melanoma image misclassified as a dysplastic nevus. Note the light areas in the upper right quadrant of the image that represent reflection from flaking skin.

This misclassification can be interpreted in two primary ways. One level of decomposition beyond the main level is a result of the closely valued features between the melanoma and dysplastic in channel 2. As a result, it may be worthwhile to reconsider the definition of the classification variable or to increase the classification variable to a value greater than 1 to delineate the melanoma and dysplastic nevus class boundary. An alternate interpretation of the misclassification of these dysplastic nevi may be that these two nevi are in the early stages of malignant transformation, but are not showing any visible features to be identified as melanoma by a physician. Since none of the lesions visually diagnosed as dysplastic nevus were biopsied, these two lesions could potentially be at the very early stage of melanoma. This possibility deserves further consideration as it may show that the ADWAT method is more sensitive than the ABCD rule in making diagnosis of early melanoma. Further investigation and patient follow-up is needed before this hypothesis can be confirmed or disproved.

The ADWAT classification method requires approximately 15-20 seconds for image decomposition, computing the feature values and making a decision about the image class of the unknown. The method suggested by Chang and Kuo [34] requires more time due to the distance calculations involved in the classification phase.

The same set of features used during the training phase of the ADWAT classification method were used to train a three layer feed-forward neural network with back-propagation training algorithm [102-103]. The back-propagation training algorithm is an iterative gradient algorithm designed to minimize the mean square error between the actual outputs of a multiplayer feed forward perceptron and the desired output. The first and second hidden layers of the network had ten and six neurons respectively while the

output layer had one neuron. The two hidden layers had a nonlinear log-sigmoid transfer function while the output layer had a linear transfer function. It required 957 cycles of iterations through the training set for the error to go below 0.00001. The feature set used in the classification phase of the ADWAT classification method was then presented to this trained network. It produced a true positive fraction (TPF) of 90% with a false positive fraction (FPF) of 25%.

The sensitivity of the ADWAT classification method is better then the sensitivity of the ABCD rule [4-7]. The TPF and FPF values are much improved as compared to the method suggested by Chang and Kuo [34]. Compared to the neural network backpropagation method [102-103], the ADWAT classification method has better specificity. Also the physicians find more information in the epiluminesence images obtained using the Nevoscope [14-15] than normal visual examination. But, more data needs to be analyzed before the ADWAT classification method can be used in a clinical setting.

4.1.3.3 Potential Applications. The ADWAT classification method is especially effective and fast as compared to that of Chang and Kuo [34] when images with different surface characteristics but similar dominant frequency channels are to be classified. Instead of measuring the distance between features and iteratively adding new features into the classification process, the images can be classified by using a semantic comparison of the tree structure signatures, making the classification process simpler. Although the ADWAT method has been illustrated here with two image classes, it can be adapted easily to accommodate more classes. Instead of using a single threshold, multiple thresholds and tree structures will be obtained, depending upon the number of classes.

However, the learning phase, especially the procedure for obtaining the threshold values may become tedious with an increase in the number of classes.

4.2 Monte Carlo Simulation Results

The calculations performed by the MCSVL algorithm for the photon transport within the tissue and its interaction with the tissue are verified by comparing the results with the simulation and experimental results reported.

4.2.1 Comparison with Published Simulation Results

Two voxel-based tissue models with same optical properties as used by Gardner [77] and Wang and Jacques [43] in their simulations were formed. Cubical voxels with all dimensions equal to 0.01cm and 0.02cm were used in these two models respectively, as described in Section 2.4. Both these models were simulated using a point source with 500,000 photons incident perpendicular to the skin surface for illumination along with a detector array placed at the top and bottom of the tissue block for collection. Gardner [77] and Wang and Jacques [43] have used the same optical geometry in their simulations. The total flux collected by the top and the bottom detector arrays was normalized using the total number of incident photons to obtain the values of diffused reflectance and transmittance respectively. Table 4.4 shows the comparison of the estimated values of the diffused reflectance and transmittance obtained using MCSVL with the results published by Gardner [77] and Wang and Jacques [43]. All results agree.

Two models with different voxel dimensions but similar optical properties were simulated in order to verify that the voxel dimensions have no effect on the light distribution within the tissue. For this, the energy absorbed by the three dimensional

material grid in both the models was analyzed using contour plots. Figure 4.5 and Figure 4.6 shows the contour plots of energy distribution within different voxel layers parallel to the skin surface for both the models. Contour plots of the energy distribution in the X-Z and Y-Z vertical planes under the point of incidence are also shown in these figures. For both the models, the contour plots show a symmetric diffusion of light within the tissue along both the X and Y directions, as expected in a homogenous tissue model.

Table 4.4 Verification of MCSVL program

Source	Number of Photons Simulated	Diffuse Reflectance	Transmittance
MCSVL with 0.01cm cubical voxel	500,000	0.2377	0.0971
MCSVL with 0.02cm cubical voxel	500,000	0.2379	0.0968
Gardner [77]	100,000	0.2381	0.0974
Wang and Jacques [43]	1,000,000	0.2375	0.0965

Changes in the beam profile and diffusion of light within the tissue were observed by changing the angle of incidence of the point source. The two tissue models mentioned above were simulated with the point source incident at 45 degrees with respect to the tissue normal (Z-axis) and the X-axis and at 90 degrees with respect to the Y-axis. Figure 4.7 shows the contour plots of the energy distribution within the tissue for the model using 0.01cm cubical voxels. Similar results were obtained for the model using cubical voxels with side equal to 0.02cm. The contour plots show an elliptical distribution with the major axis along the X direction and the minor axis along the Y direction.

4.2.2 Comparison with Experimental Data

A three layer, wavelength-dependent voxel-based tissue model of the medium pigmented or the Asian skin color type was developed. This model was simulated using the optical geometry of the spectroanalyser system [98]. Zeng et al [97-98] have used the spectroanalyser system for diffuse reflectance measurements on Asian volunteers. In the spectroanalyser system the light is incident at an angle of 5 degrees with respect to the tissue normal and the collection angle is 30 degrees. This optical geometry was setup in the simulations as explained in Section 3.2.4. White and black skin color type models were also developed and simulated using the same optical geometry. For all these models, diffuse reflectance was estimated for optical wavelengths with an interval of 5nm over the range of 350-700nm. Results were obtained by taking an average value of the diffuse reflectance obtained from three independent runs using 100,000 photons each. Figure 4.8 shows the diffuse reflectance spectra obtained by direct measurement at different body locations using the spectroanalyser system [97-98]. Figure 4.9 shows the diffuse reflectance spectra obtained using MCSVL for the three skin color type models. All the spectra show the two characteristic oxy-hemoglobin absorption valleys between 520nm and 600nm. The characteristic oxy-hemoglobin absorption valleys become less prominent as the level of pigmentation in the skin increases. This reduction in the characteristic oxy-hemoglobin absorption valleys from the lightly pigmented to highly pigmented skin type spectra can be attributed to the absorption due to melanin becoming more prominent than the oxy-hemoglobin absorption. Comparing the three diffuse reflectance spectra in Figure 4.9, one can observe a drop in the diffuse reflectance values

as the skin pigmentation level increases. This signifies an increase in the tissue absorption with an increase in the skin pigmentation level.

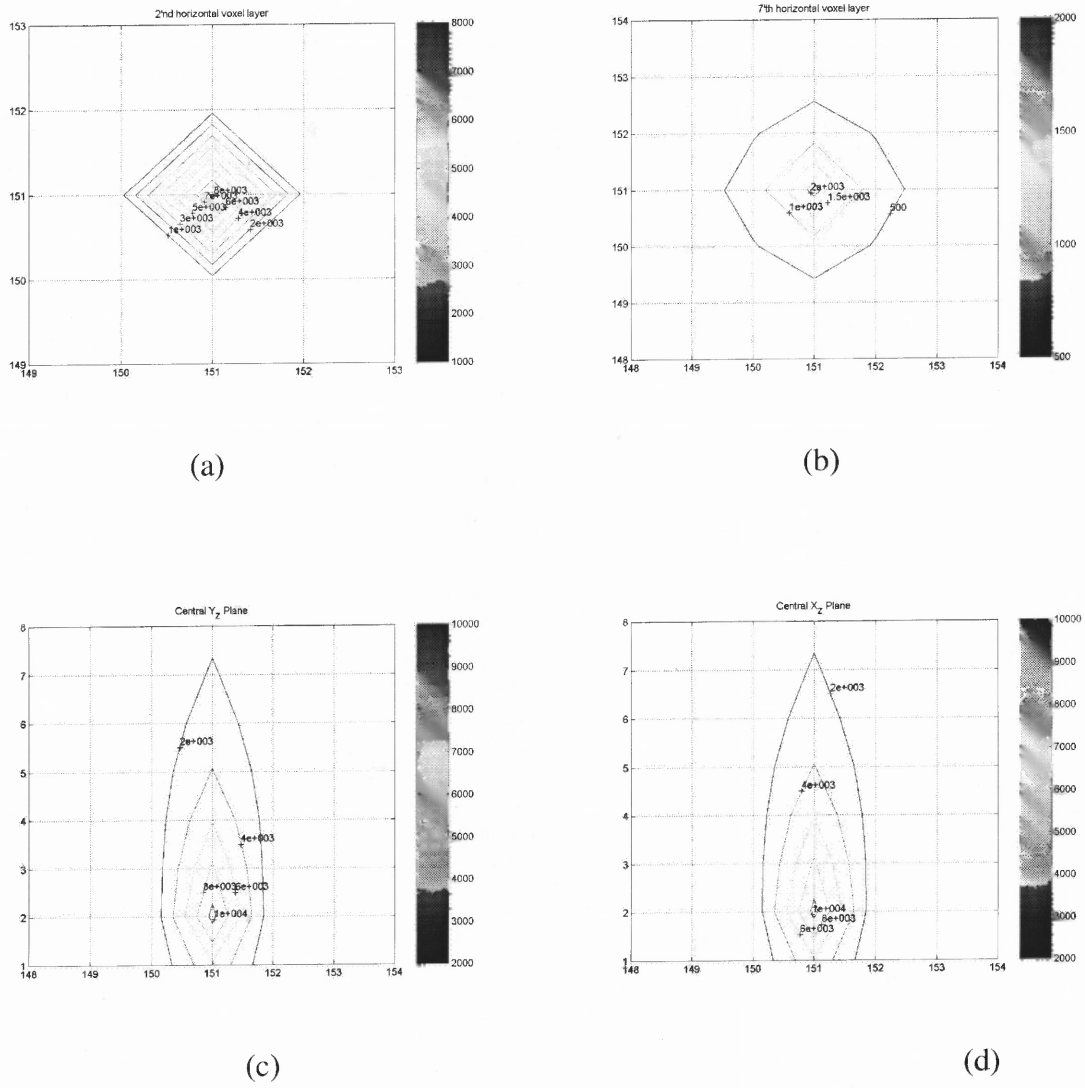

Figure 4.5 Contour plots for tissue model with 0.01cm cubical voxels: (a-b) for the 2nd and 7th voxel layer parallel to the tissue surface, (c) For the Y-Z plane passing through the point of incidence and (d) For the X-Z plane passing through the point of incidence.

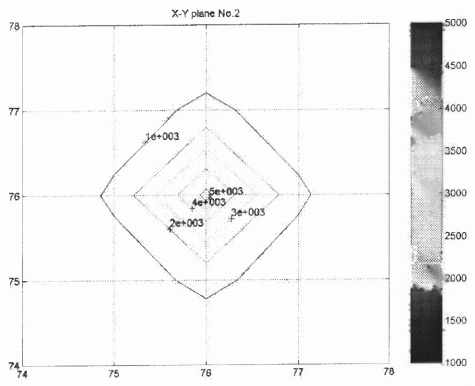

(a)

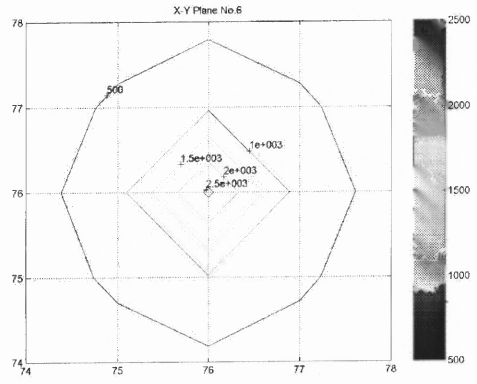

(b)

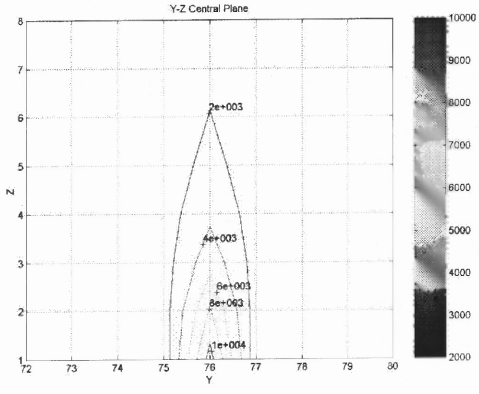

(c)

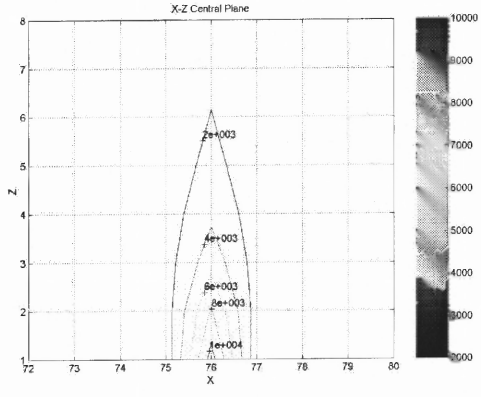

(d)

Figure 4.6 Contour plots for tissue model with 0.02cm cubical voxels: (a-b) for the 2nd and 5th voxel layer parallel to the tissue surface, (c) For the Y-Z plane passing through the point of incidence and (d) For the X-Z plane passing through the point of incidence.

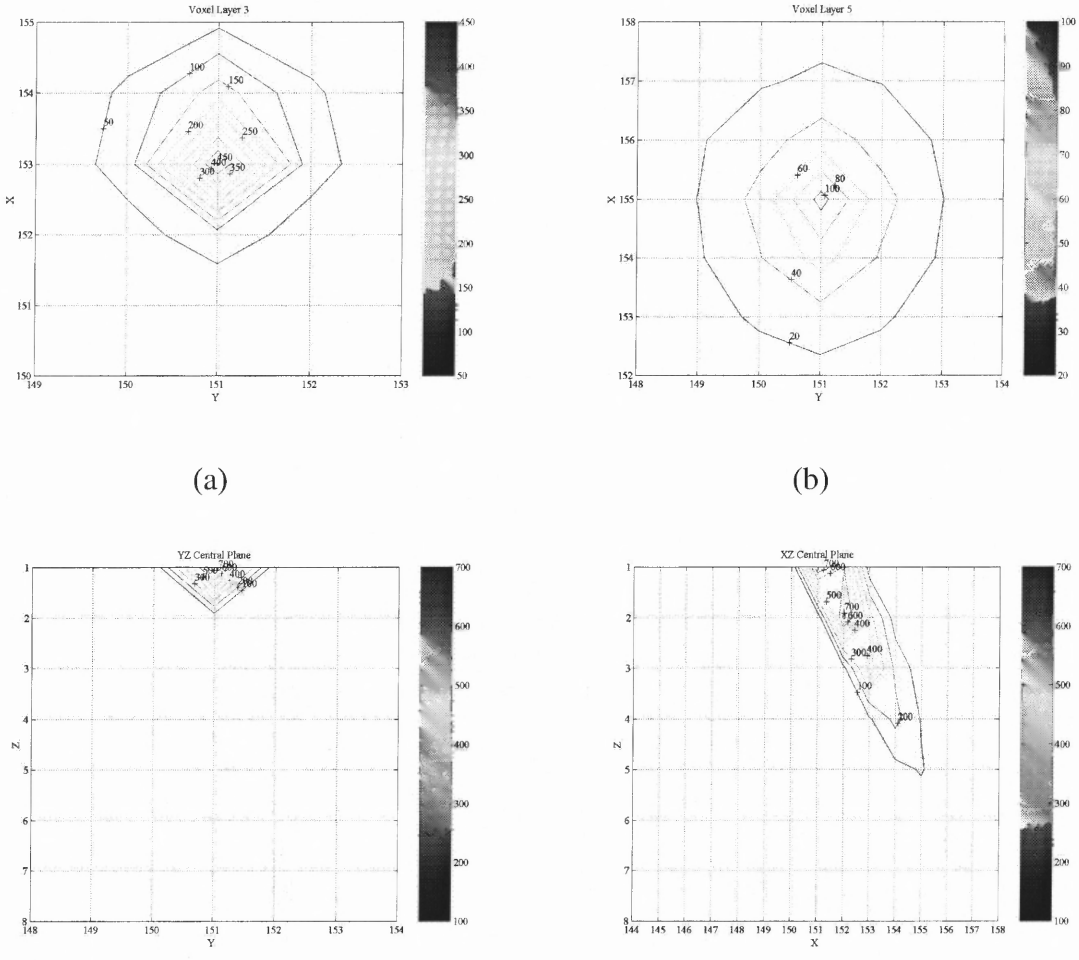

Figure 4.7 Contour plots with the light source incident at 45 degrees: (a-b) for the 3rd and 5th voxel layer parallel to the tissue surface, (c) For the Y-Z plane passing through the point of incidence and (d) For the X-Z plane passing through the point of incidence.

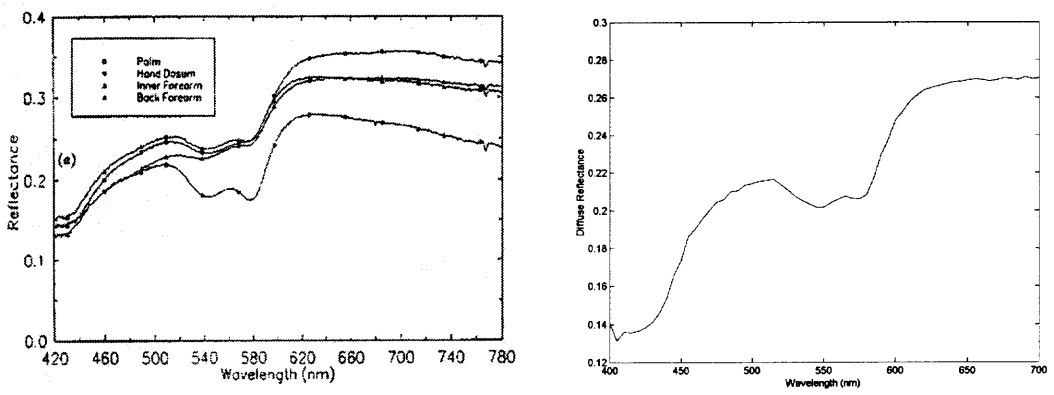

Figure 4.8 Diffuse reflectance spectra obtained using the spectroanalyser system. Results reproduced from the data reported by Zeng, MacAulay, Palcic and McLean [97-98].

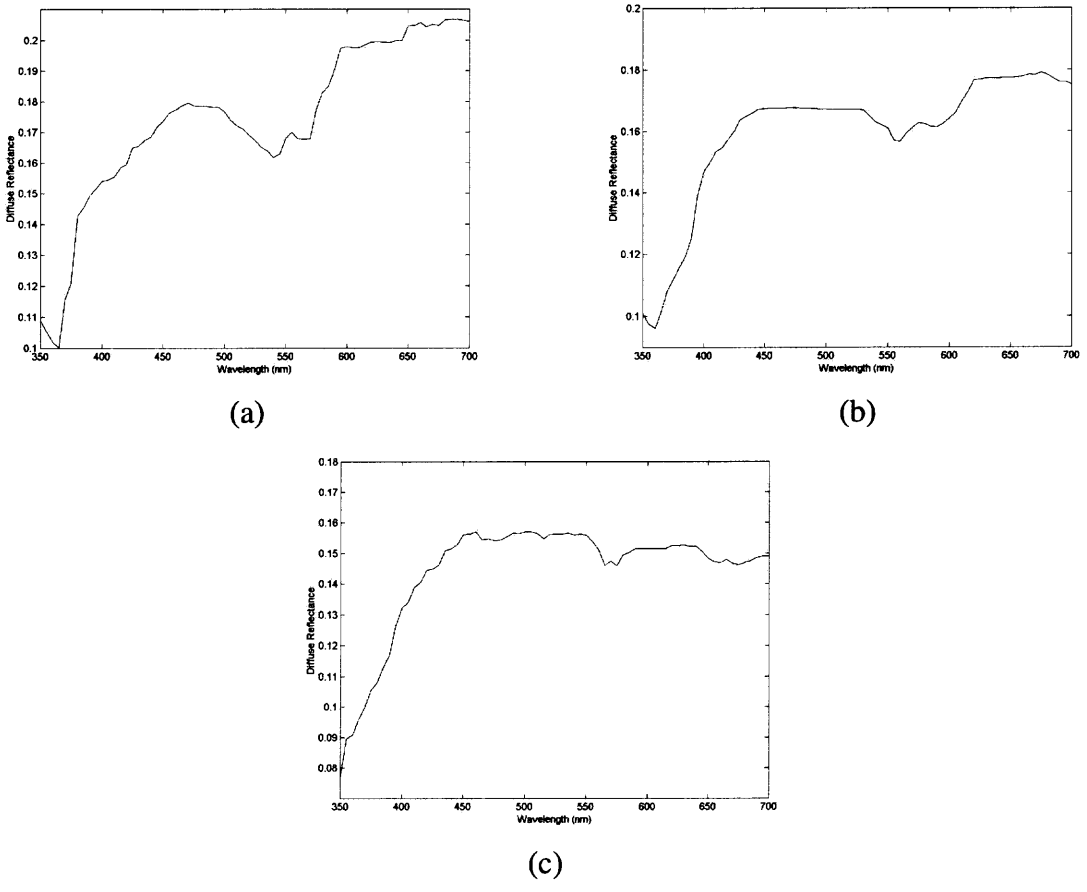

Figure 4.9 Diffuse reflectance spectra estimated using MCSVL: (a) lightly pigmented skin model, (b) medium pigmented skin model and (c) highly pigmented skin model.

Although the diffuse reflectance spectra obtained using the MCSVL code has similar characteristics to those measured experimentally using the spectroanalyser system, the values differ. This is attributed to the difference in the method of normalization and the difference between the measurement set-up used in the simulations and actual measurements. A point light source is used in the MCSVL simulations where as the spectroanalyser system uses a 1mm core diameter fused silica fiber for illumination. The method of normalizing the collected flux to obtain the values of the diffuse reflectance is different in our simulations from the method used by Zeng et al [97-98]. For the spectroanalyser system measurements, the diffuse reflectance spectrum obtained using a standard disc with constant reflectance, independent of wavelength, was used as a reference. This spectrum was used to normalize the measured skin spectrum. For MCSVL estimates, the diffuse reflectance values were normalized by dividing the collected flux by the number of photons used in the simulation.

The diffuse reflectance spectra from different body locations of the Asian Volunteer are different in details except for the two characteristic oxy-hemoglobin absorption valleys. This signifies that the diffuse reflectance values vary with the skin thickness and the concentration of the chromophores associated with it. The classification of skin is based on the volume fraction of the epidermis occupied by melanosomes, fmel, which for white color skin is equal to 1.3-6.3%, 11-16% for brown/olive color skin and 18-43% for black color skin, according to Jacques [81]. The average values of these fmel ranges were used in calculating the epidermal absorption coefficient for the three skin color type models.

4.2.3 Results Obtained With Nevoscope Optical Geometry

The simulation results obtained using the Nevoscope optical geometry are presented and analyzed in this section. The results are also compared with those obtained using the spectroanalyser system optical geometry.

4.2.3.1 Diffuse Reflectance Spectra. Figure 4.10 shows the diffuse reflectance spectra obtained for the three skin types based on their melanin concentration measured by the detector placed parallel to the skin surface in the Nevoscope setup. All the diffuse reflectance spectra show the two characteristic oxy-hemoglobin absorption valleys between 520nm and 600nm. These diffuse reflectance spectra are very similar to those obtained using the spectroanalyser system geometry [97-98]. (Please refer to Figure 4.8 for the spectra obtained using the spectroanalyser system geometry). Comparing the spectra obtained using the Nevoscope and spectroanalyser system geometry, one can see that the characteristic oxy-hemoglobin absorption valleys for the highly pigmented skin type are more prominent when measured using the Nevoscope.

4.2.3.2 Optical Wavelengths for Trans-illumination Imaging. From the skin lesion model simulations, correlation coefficients between the lesion depths and the diffuse reflectance were calculated. Wavelengths that produced the absolute value of the correlation coefficient greater than 0.7 and were common for both the 5mm and 3mm diameter skin lesion models simulated with the 2cm diameter ring light source were selected for skin lesion imaging. Table 4.5 shows these wavelengths and their corresponding values of the correlation coefficients for both the skin lesion models. The correlation coefficients are positive except for 360nm and 580nm. A positive correlation coefficient indicates an increase in diffuse reflectance as the nevus depth increases. This

is significant from the imaging point of view for a better characterization of the nevus depth. At 360nm the absorption of light due to melanin is very high, also the scattering by the superficial skin layers (Stratum corneum) would be high at this wavelength, preventing it form penetrating any deeper. Due to this 360nm light will not be able to sample nevus depths effectively resulting in a negative correlation coefficient value. 580nm would sample the nevus depths more effectively than 360nm due to more penetration in the tissue. But, at this wavelength the absorption due to hemoglobin would be very high. This may have resulted into a negative correlation coefficient value at this

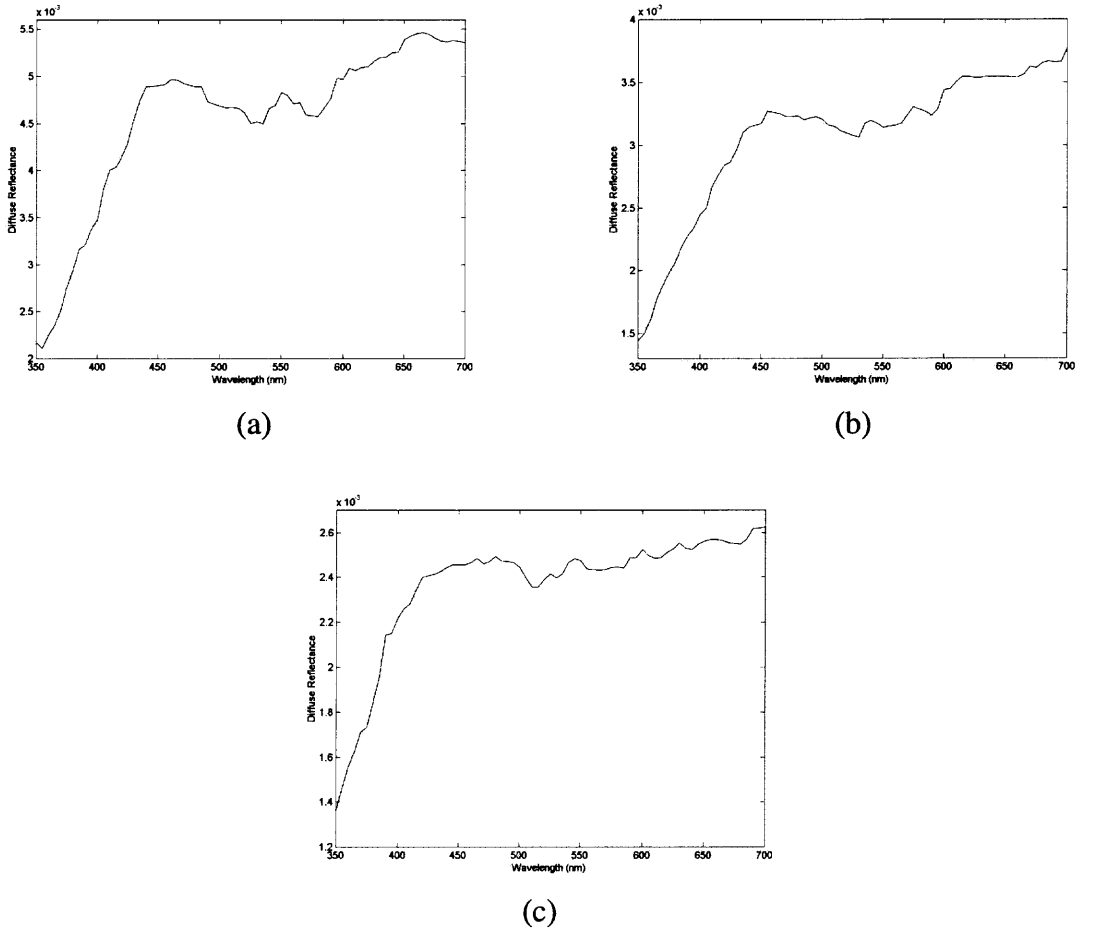

Figure 4.10 Diffuse reflectance spectra with detector parallel to the skin surface: (a) lightly pigmented, (b) medium pigmented and (c) highly pigmented.

wavelength. For the 5mm and 3mm nevus models simulated with a 1.8cm ring light source, the wavelengths for which the absolute values of the correlation coefficient are greater than CT are shown in Table 4.6. The correlation coefficient values for wavelengths given in Table 4.5 obtained from these models are also given in Table 4.6. It can be seen from Table 4.6 that the absolute value of the correlation coefficient is nearly equal to or more than CT for almost all the wavelengths selected in Table 4.5. It should be remembered that the value of CT equal to 0.7 was chosen arbitrary and has no specific significance. Comparing Table 4.5 and Table 4.6, a slight shift in the wavelengths with maximum correlation coefficients is observed with change in the ring light diameter.

Table 4.5 Wavelengths and Correlation Coefficients with 2cm Ring Light Source

3mm nevus, 2cm Ring light		**5mm nevus, 2cm Ring light**	
Wavelength (nm)	**Correlation Coeff.**	**Wavelength (nm)**	**Correlation Coeff.**
360	-0.8605	360	-0.72
495	0.782	495	0.9036
580	-0.7507	580	-0.9188
615	0.7285	615	0.8846
660	0.8092	660	0.7888
680	0.7505	680	0.8786

*Wavelengths were selected based on the absolute value of the correlation coefficient greater than 0.7 and common to both the models.

Table 4.6 Wavelengths and Correlation Coefficients with 1.8cm Ring Light Source.

3mm nevus, 1.8cm Ring light		**5mm nevus, 1.8cm Ring light**	
Wavelength (nm)	**Correlation Coeff.**	**Wavelength (nm)**	**Correlation Coeff.**
360*	-0.6478	355	-0.7677
380	0.7036	360*	-0.7026
495*	0.7253	490	0.7513
575	-0.87	495*	0.7103
580*	-0.6885	580*	-0.7418
615*	0.6920	590	-0.9526
660*	0.7362	615*	0.7454
680*	0.8138	655	0.8627
		660*	0.5836
		680*	0.7721
		695	0.9216

*Wavelengths that also appear in Table 4.5.

This shift is observed more in the simulation results of 5mm diameter nevus than the 3mm diameter nevus. This could be attributed to the fact that the ring light source is more close to the nevus periphery in the 5mm diameter nevus model with 1.8cm ring light diameter than in any other simulation. A maximum shift of 10nm is observed from 580nm to 590nm in this simulation while a maximum shift of 20nm is observed from 360nm to 380nm in the 3mm diameter nevus simulation. Both 360nm and 580nm wavelengths have a negative correlation coefficients, as was pointed out earlier. Overall,

lesser shift in wavelength and a better correlation between the nevus depths and the diffuse reflectance is obtained for wavelengths above 600nm. This is the region where the absorption due to both melanin and hemoglobin is less and also the scattering of light in the epidermal and dermal layers is less.

From the results, it can be said that optical wavelengths of 495, 580, 615, 660 and 680nm can be used for multi-spectral imaging and characterization of the skin lesions using the Nevoscope. For wavelength below ~450nm there would be secondary emissions from natural fluorophores inside the skin due to auto-fluorescence [23] which is not taken in to account in the simulations performed. A certain amount of uncertainty is involved in selecting the wavelength for multi-spectral imaging of the skin lesions due to auto-fluorescence.

4.3 Classification Using Multi-spectral Images

The ADWAT classification method uses the epi-illuminance images of the skin lesion obtained using a white light source. These images contain the superficial skin lesion features that are used by a physician for diagnosis using the ABCD rule. The ADWAT classification method uses the spatial-frequency information in these images that correspond to these superficial skin lesion features. The suspicious skin lesions are removed and analyzed in the histo-pathology lab where the information about the lesion depth and architecture is obtained. Based on this information a case of melanoma is confirmed.

Multi-spectral trans-illuminance images of the skin lesion give information about the lesion depth and architecture, hence analysis of these images would improve the

sensitivity of melanoma diagnosis. In this section classification results obtained using the Extended ADWAT method and Fuzzy Membership functions are presented and discussed.

4.3.1 Results of the Extended ADWAT Classification Method

The multi-spectral images obtained using 580nm and 610nm were analyzed using the technique described in the ADWAT classification method. Statistical analysis of the channel energy and energy ratio features of these images was used to obtain features that segregated into bimodal distributions between lesion classes. Threshold values were calculated for these features to obtain maximum separation between the two image classes. The feature set and their corresponding threshold values obtained from the multi-spectral images are summarized in Table 4.7. Feature set and threshold values obtained from the epi-illuminance images are also given in Table 4.7 to present the combined feature set. Feature data values used to generate the threshold values given in Table 4.7 are illustrated in Figure 4.11. All the features obtained from the multi-spectral images had bimodal feature segregation. Thresholds were obtained for these channels by averaging the means of the features for the two lesion classes. Figure 4.11 a-e illustrate the features for the 580nm wavelength image and Figure 4.11 f-h illustrate the features for the 610nm wavelength image.

In the first step of the classification decision about the image class is taken based on the value of CV_1, which counts the number of channels in the epi-illuminance image that satisfy the threshold criteria and are decomposed further. If CV_1 is equal to 1 then the image is assigned to the dysplastic nevus class; for $CV_1 = 6$ the image is assigned to the melanoma class and for any other value of CV_1 the image is assigned to the suspicious

lesion class. Out of the 15 melanoma and 45 dysplastic nevus images used in the classification phase 16 images were tagged as suspicious. 10 images of melanoma and 34 dysplastic nevus images were correctly classified in Step 1.

Table 4.7 Combined Features Set Obtained from the Skin Lesion Images.

Image Type	Channel	Energy feature	Distribution type Separable/bimodal	Threshold for decomposition
Epi-illuminance image with white light source	2	e2/e1	Bimodal	> 0.0366
	3	e3/e1	Bimodal	> 0.043
	2.1	e2.1/(e2.2+e2.3+e2.4)	linearly separable	> 0.34
	3.1	e3.1/(e3.2+e3.3+e3.4)	linearly separable	> 0.315
	2.1.4	e2.1.4/e2.1.1	linearly separable	< 0.837
Trans-illuminance image with 580nm wavelength	1	e1	Bimodal	< 67.8980
	2	e2/e1	Bimodal	< 0.0287
	1.1	e1.1	Bimodal	< 133.3732
	1.4	e1.4/e1.1	Bimodal	>0.0148
	1.1.1	e1.1.1	Bimodal	< 130.1408
Trans-illuminance image with 610nm wavelength	1	e1	Bimodal	< 91.1113
	1.1	e1.1	Bimodal	< 186.0038
	1.1.1	e1.1.1	Bimodal	< 181.3693

1. Selected features obtained from a statistical analysis were either linearly separable or segregated bimodally between classes.
2. The channel, corresponding energy feature ratio, and the threshold values obtained for maximum separation of the two classes are given.

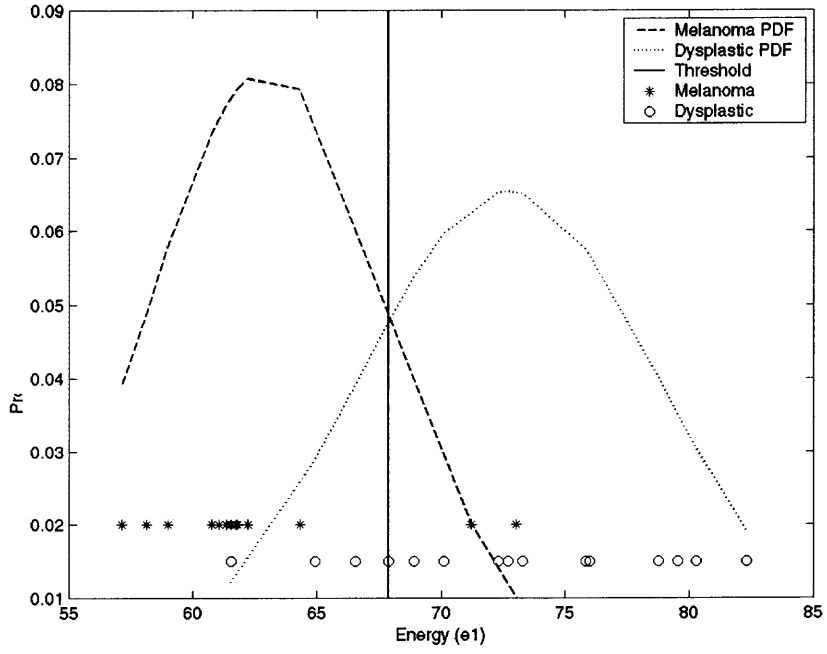

(a)

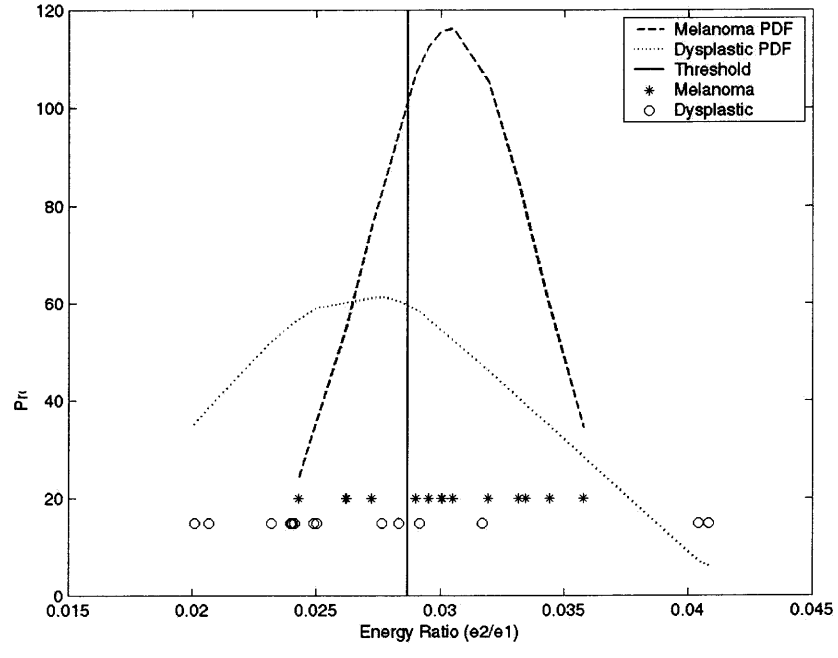

(b)

Figure 4.11 Feature data values for multi-spectral image training data

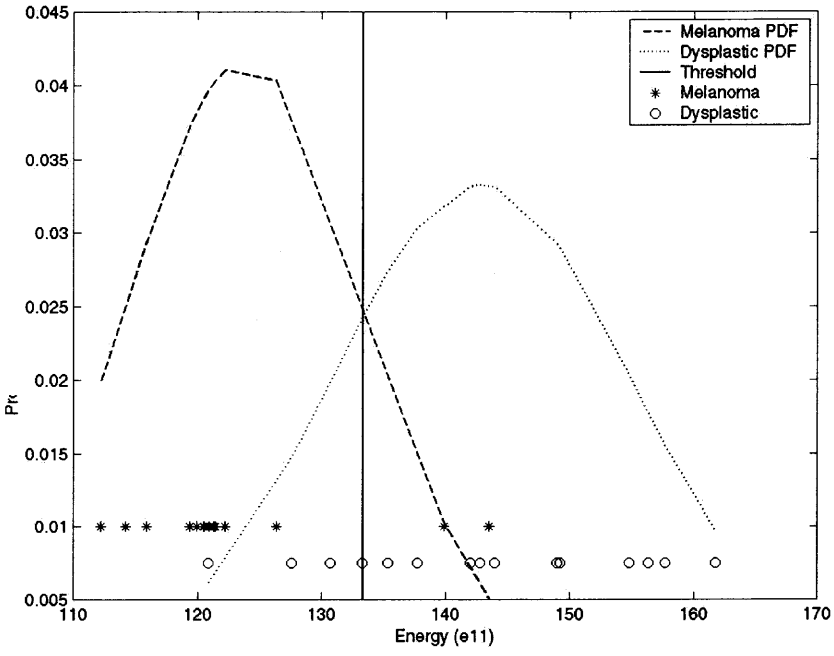

(c)

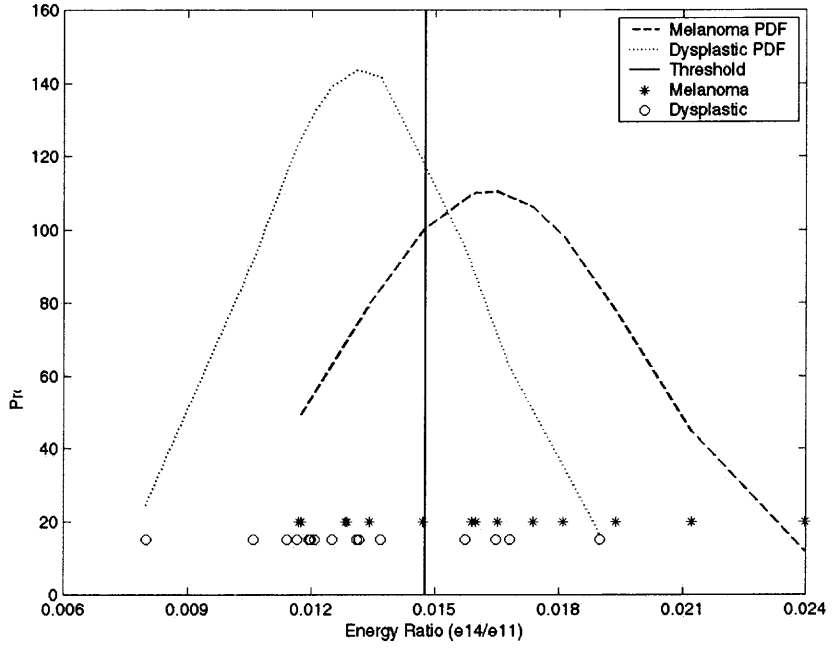

(d)

Figure 4.11 (Continued)

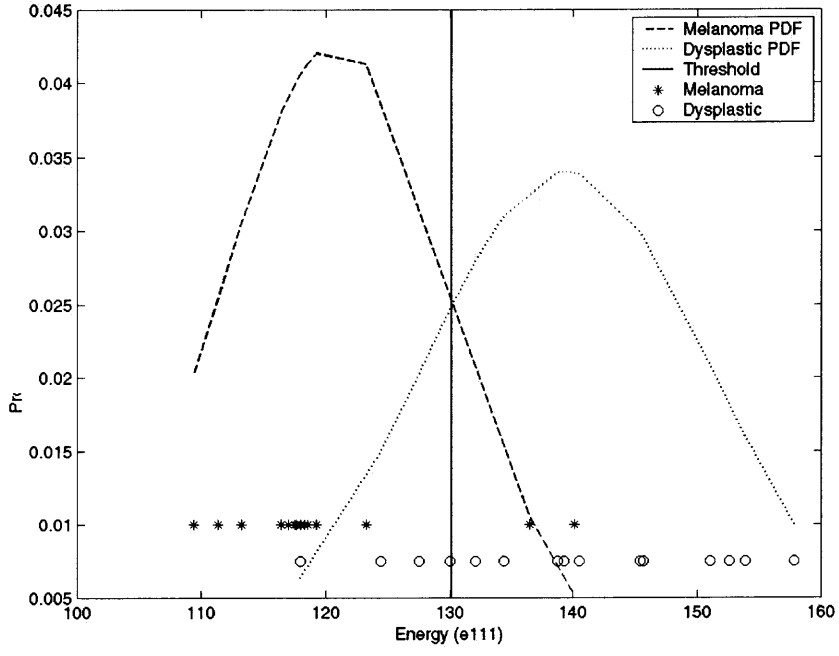

(e)

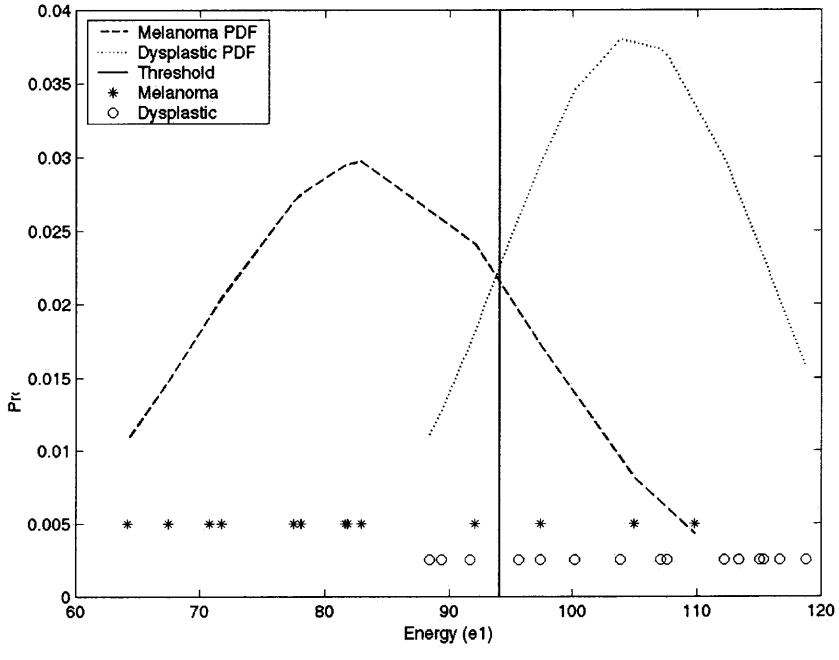

(f)

Figure 4.11 (Continued)

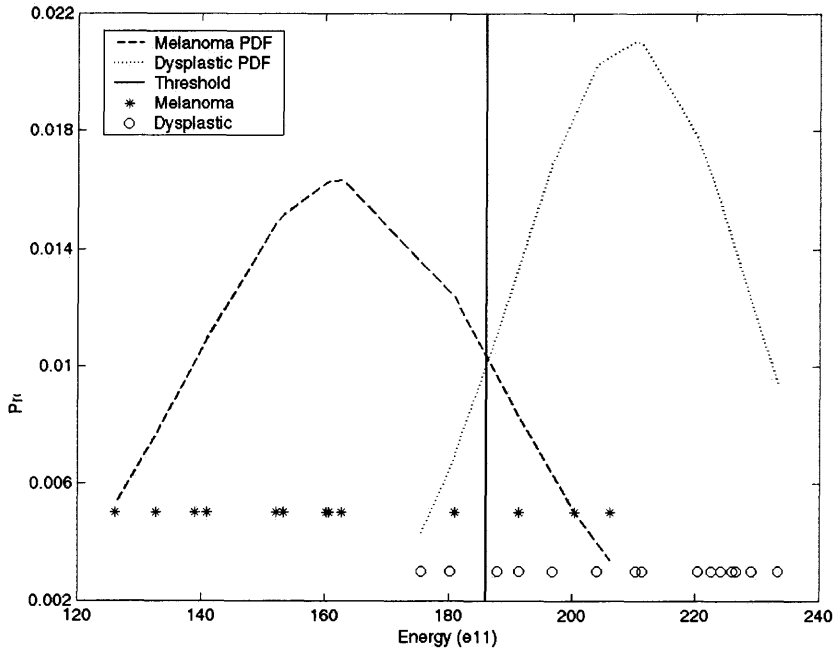

(g)

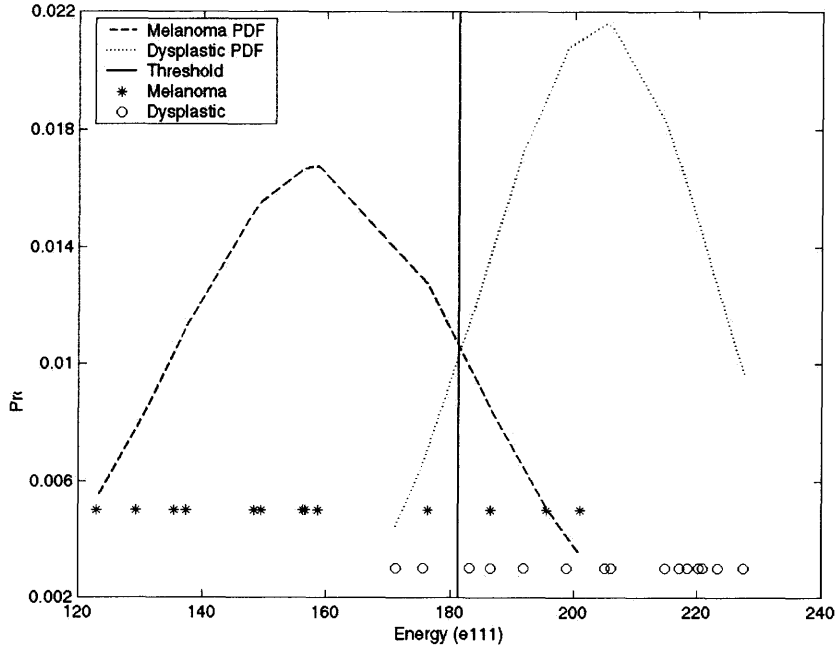

(h)

Figure 4.11 (Continued)

The multi-spectral images of the lesions that were assigned to the suspicious lesion class were analyzed in the second step of the classification process as explained in Section 3.3. Classification results were obtained using different values of the Melanoma Probability Threshold (MPT). The best classification results were obtained for a value of MPT equal to 0.7. For this MPT, out of the 16 cases that were tagged as suspicious at the first step of classification, 11 cases were correctly classified during the second step of the classification process. 1 melanoma case and 4 dysplastic nevus cases were misclassified. The resulting true positive fraction (TPF) obtained for this classifier was 93.33% with a false positive fraction (FPF) of 8.88%.

The features used in the ADWAT classification method are dependent on the superficial skin lesion features that are used in the ABCD rule. During early stages of melanoma it is very difficult to differentiate between a melanoma and dysplastic nevus based on these features. Most of these features would be hardly visible during the early stages of melanoma. Since epi-illuminance images obtained using white light source are used in the analysis, the success of this method is dependent on the placement of the Nevoscope around the skin lesion. Any gap between the Nevoscope and the skin surface would cause uneven surface reflection. Also, in some cases flaking of the skin is observed to occur which may cause uneven surface reflection. All these factors will decide the channel energy values in the wavelet transform decomposition and hence decide the success of the ADWAT method.

The extended ADWAT method uses combined features from the epi-illuminance images obtained using white light source and the multi-spectral trans-illuminance images using specific wavelength light sources. Suspicious melanoma cases from the ADWAT

classification method due to less developed superficial features of uneven surface reflection are taken to the next step of analysis. Multi-spectral trans-illuminance images are analyzed in this step. These images give information related to the nevus architecture and depth and are less affected from the uneven surface reflection. Hence the extended ADWAT method will give more accurate results and the variance in the overall success of this method will be less compared to the ADWAT method.

4.3.2 Classification Results Using Fuzzy Membership Functions

Bimodal features were obtained from the epi-illumination images and the multi-spectral trans-illumination images using wavelet decomposition and statistical analysis of the channel energy and energy ratios for the Extended ADWAT classification method. All these features were combined to form a composite feature set. In this composite feature set the dynamic range of the channel energy ratio features is far less compared to the dynamic range of the channel energy features. For classification it is necessary to normalize the feature set so that all the features have similar dynamic range. In the Extended ADWAT method each feature was compared with the corresponding feature value of the candidate images independently and hence normalization was not necessary. Using linear transformations all the features in the composite feature set were normalized so that they have a dynamic range between zero and one. Using the values of M_A, K_A and N_A that were calculated from the learning data set, the values of the dysplastic and melanoma membership functions were calculated for the unknown image sets using Equations (3.28) and (3.29). Decision as to whether the unknown image set belongs to the melanoma or dysplastic nevus class was taken based on the "winner takes all"

criteria. The unknown image set was assigned to the class with maximum membership function value.

Out of the 60 unknown images (15 melanoma and 45 dysplastic nevus cases) used in the classification phase, 52 cases were correctly classified using the Gaussian membership function. All the cases of melanoma and 37 cases of dysplastic nevus were identified giving a true positive fraction of 100% with a false positive fraction of 17.77%. For the eight dysplastic nevus cases that were misclassified the values of both the melanoma and dysplastic nevus membership functions were equal to zero. These cases were assigned to the melanoma category since no decision about the class can be taken if both the membership function values are the same.

Classification results were obtained for the Bell membership function using different values of the weighing constant W. The results are summarized in Table 4.8. Out of all the values of W used, best classification results are obtained for a value of 0.6 with a true positive fraction of 100% with a false positive fraction of 4.44%.

Table 4.8 Results Obtained Using Bell Membership Function.

W	Melanoma Misclassified M (15)	Dysplastic Misclassified D (45)	True Positive (%)	False Positive (%)
0.1	12	0	20	0
0.2	6	0	60	0
0.3	3	0	80	0
0.4	2	0	86.66	0
0.5	1	0	93.33	0
0.6	0	2	100	4.44
0.7	0	5	100	11.11
0.8	0	5	100	11.11
0.9	0	30	100	66.66
1.0	0	38	100	84.44

*S is taken equal to 10^{23}

4.4 Summary of the Classification Results

The skin lesion images obtained using the Nevoscope were classified using different techniques into two classes, melanoma and dysplastic nevus. The epi-illuminance images obtained using a white light source were classified using the Constant Threshold Method, Neural Network with back-propagation training algorithm and ADWAT method. The results presented in Section 4.1 were obtained using 10 melanoma images and 20 dysplastic nevus images as candidate images for classification.

The combined set of epi-illuminance and multi-spectral trans-illuminance images was classified using the Extended ADWAT method and the Fuzzy Membership Functions Method. 15 melanoma images and 45 dysplastic nevus images were used as candidate images for classification. The epi-illuminance images from this data set were also classified using the classification methods applied on epi-illuminance image data alone. The results obtained from all these classification techniques are summarized in Table 4.9. By comparing the classification results it can be said that combining the information obtained from the multi-spectral trans-illuminance images with the information obtained from the epi-illuminance images, improves the classification of the skin lesions.

Table 4.9 Summary of the Classification Results.

Type of Images Used	Method	Images Correctly Classified		True Positive	False Positive
		Melanoma	Dysplastic		
Epi-illuminance Images	Constant Threshold	11/15	36/45	73.33%	20%
	Neural Network	13/15	34/45	86.66%	24.44%
	ADWAT	13/15	40/45	86.66%	11.11%
Multi-spectral and Epi-illuminance Images	Extended ADWAT	14/15	41/45	93.33%	8.88%
	Gaussian Membership Functions	15/15	37/45	100%	17.77%
	Bell Membership Functions	15/15	43/45	100%	4.44%

CHAPTER 5

CONCLUSIONS AND FUTURE WORK

The first objective of this study was to analyze the epi-illuminance images of the skin lesion, extract features and classify the images into melanoma and dysplastic nevus image classes. For this an adaptive wavelet transform based tree structure classification method (ADWAT) was proposed. In this method tree structure signatures of the different image classes are formed using statistical analysis of the feature set. Semantic comparison of the tree structure produced by the unknown image with the signatures of the different image classes is then used for classification. The ADWAT method using the mean energy ratios with statistically selected threshold values is effective and simple for classification of the images based on their spatial and frequency information. The tree structure model developed by using this method is more robust than the one employing a fixed threshold of the maximum energy ratio. This work also shows that the epi-illuminance images of the skin lesions obtained using the Nevoscope capture the features used in the ABCD rule effectively and hence are promising in the early diagnosis of melanoma.

The second objective of this study was to find optimal optical wavelengths in the visible range which when used in the trans-illumination imaging could give information for characterizing melanoma depth and architecture. A Monte Carlo simulation program (MCSVL) was developed to simulate the tissue models built using a voxel library. Verification of the algorithm shows that MCSVL can give results that agree with the reported experimental and simulation data. Also, with some modifications in the photon launching and detection subroutines more complicated illumination and detection

geometries for estimation and characterization of tissue optical properties can be handled using the MCSVL program. The voxel-based approach offers flexibility in developing complex non-homogeneous tissue models. Also the use of voxel library in generating these models offers the flexibility of updating the physical and optical properties of the voxel corresponding to a medium or adding new media types into the models as new experimental results are reported.

Skin lesion models of different depths and diameters were formed and simulated using the Nevoscope optical geometry. Correlation analysis was used to find optimal optical wavelengths for multi-spectral imaging of the skin lesions. The simulation results indicate that combining the wavelength dependent penetration of monochromatic light in the trans-illumination imaging using the Nevoscope, the skin lesion depth and architectural information can be characterized.

To collect multi-spectral images of the skin lesions using the selected optical wavelengths and to analyze them for the diagnosis of melanoma was the last objective of this study. Skin lesion data is being collected using the selected wavelengths with high correlation coefficient values between the lesion depth and the diffuse reflectance. The multi-spectral trans-illumination images were analyzed for feature extraction. Derived features giving spatial / frequency and textural information were obtained using wavelet decomposition and statistical analysis. The combined feature set obtained from the epi-illuminance and multi-spectral trans-illuminance images was used in the classification. Two different classification techniques namely, Extended ADWAT method and Fuzzy Membership Functions method were applied and the results were compared. The results obtained from these two methods are better than those obtained using ADWAT method

with features from the epi-illuminance images alone. The Fuzzy Membership Function method gives much better results than the Extended-ADWAT method since it dose not use crisp partitions to separate the two image classes that have overlapping features. Results indicate that the multi-spectral trans-illuminance images add more information in the diagnosis of melanoma and hence improve its sensitivity and specificity. Although promising results were obtained from this analysis, more data needs to be collected and analyzed before the classification methods can be employed in a clinical setup.

Although six different wavelengths were selected from the correlation analysis for multi-spectral imaging, data was collected only using three of them. Wavelengths above 650nm may give more information related to the lesion architecture due to more penetration power. For smaller wavelengths around 510nm the ring light illumination of the skin lesion is non-uniform thus forming a dark spot at the center of the image. It is due to this reason that the images obtained using the blue wavelength were not used in the multi-spectral analysis. A radial enhancement function can be calculated using the intensity variation measurements along the ring light diameter. Monte Carlo simulations can also be used for this purpose to obtain the diffuse reflectance and photon detection probability profile along the ring light diameter.

The simulations have shown a slight variation in the wavelengths with maximum correlation coefficients as the ring light diameter is changed. This effect should be studied further. Perhaps a variable diameter ring light source should be used for collecting the skin lesion images. Smaller ring light diameters at lower wavelengths would make the lesion illumination more uniform and eliminate the dark spot at the image center.

The possibility of three-dimensional reconstruction of the skin lesion using the multi-spectral images should be explored. Based on Monte Carlo simulations the optical penetration depths of different wavelengths can be estimated. This information can be coupled with the multi-spectral images for 3D reconstruction. A time correlation study to compare the various stages of melanoma development can also be useful in improving the diagnosis. Overall it can be said that the Nevoscope has an immense potential as an optical modality for imaging and analyzing skin lesions. Mass screening for melanoma using the Nevoscope and computer aided diagnosis for early detection and treatment would soon be possible.

REFERENCES

[1] A. Kopf, D. Rigel and R. Friedman, The rising incidence and mortality rates of malignant melanoma, J. Dermatol. Surg. Oncol., vol. 8, pp. 760-761, 1982.

[2] A. Kopf, T. Saloopek, J. Slade, A. Marghood and R. Bart, Techniques of cutaneous examination for the detection of skin cancer, Cancer Supplement, vol. 75 (2), pp. 684-690, 1994.

[3] H. Koh, R. Lew and M. Prout, Screening for melanoma/skin cancer: Theoretical and practical considerations, J. Am. Acad. Dermatol., vol. 20, pp. 159-172, 1989.

[4] W. F. Dial, ABCD rule aids in preoperative diagnosis of malignant melanoma, Cosmetic Dermatol., vol. 8(3), pp. 32-34, 1995.

[5] D. S. Rigel and R.J. Friedman, The rationale of the ABCDs of early melanoma, J. Am.Acad. Dermatol., vol. 29(6), pp. 1060-1061, 1993.

[6] J. S. Lederman, T. B. Fitzpatrick and A. J. Sober, Skin markings in the diagnosis and prognosis of cutaneous melanoma, Arch. Dermatol., vol. 120, pp. 1449-1452, 1984.

[7] M. M. Wick, A. J. Sober, T. B. Fitzpatrick, M. C. Mihm, A. W. Kopf, W. H. Clark and M. S. Blois, Clinical characteristics of early cutaneous melanoma, Cancer, vol. 45, pp. 2684-2686, 1980.

[8] Stolz, ABCD Rule, Euro. J Dermatol, http://www.dermoscopy.org, 1994.

[9] R. J. Friedman, D. S. Rigel and A. W. Kopf, Early detection of malignant melanoma: the role of physician examination and self-examination of the skin, CA Cancer J. Clin., vol. 35(3), pp. 130-151, 1985.

[10] C. Grin, A. Kopf, B. Welkovich, R. Bart, M. Levenstein, Accuracy in the clinical diagnosis of melanoma, Arch Dermatol., vol. 126, pp. 763-766, 1990.

[11] T. Dougherty, J. Kaufman, A. Goldfarb, K. Weishaupt, D. Boyle and A. Mittlemn, Photoradiation therapy for the treatment of malignant tumors, Cancer Res., vol. 38, pp. 2628-2635, 1978.

[12] K. Arndt and J. Noe, Cutaneous Laser Therapy, S. Rosen, Ed. London: Wiley, 1983.

[13] R. Bonner, T. Clem, P. Bowen, R. Bowman, Laser-Doppler continuous real-time monitor of pulsatile and mean blood flow in tissue microcirculation, Scattering Techniques Appiles to Supramolecular and Non-Equilibrium Systems, S. Chen, B. Chu and R. Nossal, Ed. New York : Plenum, 1981, pp. 685-702.

[14] A. P. Dhawan, Early detection of cutaneous malignant melanoma by three dimensional nevoscopy, Computer Methods and Programs in Biomedicine, vol. 21, pp. 59-68, 1985.

[15] A. P. Dhawan, R. Gordon and R. M. Rangayyan, Nevoscopy: three-dimensional computed tomography of nevi and melanomas in situ by transillumination, IEEE Trans. Med. Imag., vol. 3(2), pp. 54-61, June 1984.

[16] P. Kini and A. P. Dhawan, Three-Dimensional Imaging and Reconstruction of Skin-Lesions, Computerized Medical Imaging and Graphics, vol. 16(3), pp. 153-162, 1992.

[17] L. Xu, M. Jackowski, A. Goshtasby, C. Yu, D. Roseman, A. P. Dhawan, and S. Bines, Segmentation of Skin Cancer Images, Image and Vision Computing, vol. 17, pp. 65-74, 1999.

[18] A. P. Dhawan and A. Sicsu, Segmentation of images of skin-lesions using color and surface pigmentation, Computerized Medical Imaging and Graphics, vol. 16(3) pp. 163-177, 1992.

[19] P. Kini and A. P. Dhawan, Non-invasive imaging and analysis of skin lesions for early detection of cutaneous malignant melanoma, Biomedical Instrumentation and Technology, vol. 28, pp. 209-219, 1994.

[20] A. P. Dhawan, An expert system for early detection of malignant melanoma using the knowledge-based image analysis, International Journal on Analytical and Quantitative Cytology and Histology, vol. 10(6), pp. 405-416, 1988.

[21] R. Chellappa, Two-dimensional discrete Gaussian Markov random field models for image processing, Pattern Recognition, vol. 2, pp. 79-122, 1985.

[22] G. R. Cross and A. K. Jain, Markov random field texture models, IEEE Trans. Pattern Anal. And Machine Intell., vol. 5, pp. 25-39, Jan. 1983.

[23] J. W. Woods, S. Dravida and R. Mediavilla, Image estimation using doubly stochastic Gaussian random field models, IEEE Trans. Pattern Anal. And Machine Intell., vol. 9, pp. 245-253, Mar. 1987.

[24] H. Derin, Segmentation of textured images using Gibbs random fields, Computer, Vision, Graphics and Image Processing, vol. 35, pp. 72-98, 1986.

[25] H. Derin and H. Elliott, Modeling and segmentation of noisy and textured images using Gibbs random fields, IEEE Trans. Pattern Anal. And Machine Intell., vol. 9, pp. 39-55, Jan. 1987.

[26] I. Daubechies, Orthonormal bases of compactly supported wavelets, Communications on Pure and Applied Mathematics, vol. 41, pp. 909-996, Nov. 1988.

[27] I. Daubechies, The wavelet transform, time-frequency localization and signal analysis, IEEE Trans. Info. Theory, vol. 36, pp. 961-1005, Sept. 1990.

[28] C. E. Heil and D. F. Walnut, Continuous and discrete wavelet transforms, SIAM Review, vol. 31, pp. 628-666, Dec. 1989.

[29] S. G Mallat, A theory for multi-resolution signal decomposition: the wavelet representation, IEEE Trans. Pattern Anal. And Machine Intell., vol. 11, pp.674-693, July 1989.

[30] T. R. Reed and H. Wechsler, Segmentation of textured images and Gestalt organization using spatial/spatial-frequency representations, IEEE Trans. Pattern Anal. And Machine Intell., vol. 12, pp. 1-12, Jan. 1990.

[31] A. C. Bovik, Analysis of multichannel narrow band filters for image texture segmentation, IEEE Trans. Signal Processing, vol. 39, pp. 2025-2043, Sept. 1991.

[32] A. C. Bovik, M. Clark and W. S. Geisler, Multichannel texture analysis using localized spatial filters, IEEE Trans. Pattern Anal. And Machine Intell., vol. 12, pp. 55-73, Jan. 1990.

[33] R. R. Coifman and M. V. Wickerhauser, Entropy based algorithms for best basis selection, IEEE Trans. Info. Theory, vol. 38, pp. 713-718, Mar. 1992.

[34] Tianhorng Chang and C. C. Jay Kuo, Texture analysis and classification with tree-structured wavelet transform, IEEE Trans. Image processing, vol. 2, No. 4, pp. 429-441, Oct. 1993.

[35] J. M. Schmitt, G. X. Zhou and E. C. Walker, Multilayer model of photon diffusion in skin, J. Opt. Soc. Am. A, vol. 7, No. 11, pp. 2141-2153, 1990.

[36] S. Wan, R. Anderson and J. Parrish, Analytical Modeling for the Optical Properties of Skin with in Vitro and in Vivo Applications, Photochem. Photobiol., vol. 34, pp. 493-499, 1981.

[37] S. Chandrasekhar, Radiative Transfer, New York Dover, 1960.

[38] A. Ishimaru, Wave Propagation andScattering in Random Media, vol. 1, New York: Academic, 1978.

[39] B. Kim, S. Jacques, S. Rastegar, S. Thomsen and M. Motamedi, The Role of Dynamic Changes in Blood Perfusion and Optical Properties in Thermal Coagulation of the Prostate, Proc. SPIE, vol. 2391, pp. 443-450, 1995.

[40] B. Anvari, S. Rastegar and M. Motamedi, Modeling of Intraluminal Heating of Biological Tissue : Implications for Treatment of Benign Prostatic Hyperplasia, IEEE Trans. Biomed. Eng., vol. 41, No. 9, pp. 854-864, 1994.

[41] A. Sagi, A Shitzer, A. Katzir and S. Akselrod, Heating of Biological Tissue by Laser Irradiation : Theoretical Model, Optical Eng., vol. 31, No. 7, pp. 1417-1424, 1992.

[42] R. Hemenger, Optical Properties of Turbid Media with Specularly Reflecting Boundaries : Applications to Biological Problems, Appl. Optics, vol. 16, pp. 2007-2012, 1977.

[43] L. Wang and S. Jacques, Monte Carlo Modeling of Light Transport in Multi-layered Tissues in standard C, Univ. Texas, M.D. Anderson Cancer Center, 1992.

[44] M. Keijzer, S. Jacques, A. Prahl, and A. Welch, Light Distributions in Artery Tissue : Monte Carlo Simulations for Finite-diameter Laser Beams, Laser Surg. Med., vol. 9, pp. 148-154, 1989.

[45] IEEE Standard 610.4-1990, IEEE Standard Glossary of Image Processing and Pattern Recognition Terminology, New York: IEEE press, 1990.

[46] A. K. Jain, Fundamentals of Digital Image Processing, Englewood Cliffs, NJ: Prentice Hall, 1989.

[47] J. Sklansky, Image segmentation and feature extraction, IEEE. Trans. Syst. Man. Cybern., vol. 8, pp. 237-247, 1978.

[48] R. M. Haralick, Statistical and structural approaches to texture, Proc. IEEE, vol. 67, No. 5, pp. 768-804, 1979.

[49] S. Mallat, A Theory for Multisolution Signal Decomposition: The Wavelet Representation, IEEE Trans. Pattern Anal. And Machine Intell., vol. 11, pp. 674-693, July 1989.

[50] A. Laine and J. Fan, Texture classification by wavelet packet signatures, IEEE Trans. Pattern Anal. And Machine Intell., vol. 15(11), pp. 1186-1191, 1993.

[51] M. Unser, Texture classification and segmentation using wavelet frames, IEEE Trans. Image Processing., vol. 4(11), pp. 1549-1560, 1993.

[52] R. Porter and N. Canagarajah, A robust automatic clustering scheme for image segmentation using wavelets, IEEE Trans. Image Processing., vol. 5(4), pp. 662-665, 1996.

[53] H. I. Choi and W. J. Williams, Improved time-frequency representation of multicomponent signals using exponential kernels, IEEE Trans. Acoust., Speech, and Signal Processing, vol. 37, pp. 862-871, June 1989.

[54] L. Cohen, Time-frequency distributions – a review, Proc. IEEE, vol. 77, pp. 941-981, July 1989.

[55] M. Kadiyala and V. DeBrunner, Effect of wavelet bases in texture classification using a tree-structured wavelet transform, Conference Record of the Thirty-Third Asilomar Conference on Signals, Systems, and Computers, vol. 2, pp. 1292-1296, 1999.

[56] A. Mojsilovic, M. V. Popovic and D. M.Rackov, On the selection of an optimal wavelet basis for texture characterization, IEEE Trans. Image Processing, vol. 9, No. 12, pp. 2043-2050, 2000.

[57] T. Dougherty, J. Kaufman, A. Goldfarb, K. Weishaupt, D. Boyle and A. Mittlemn, Photoradiation therapy for the treatment of malignant tumors, Cancer Res., vol. 38, pp. 2628-2635, 1978.

[58] K. Arndt and J. Noe, Cutaneous Laser Therapy, S. Rosen, Ed. London: Wiley, 1983.

[59] R. Bonner, T. Clem, P. Bowen, R. Bowman, Laser-Doppler continuous real-time monitor of pulsatile and mean blood flow in tissue microcirculation, Scattering Techniques Appiles to Supramolecular and Non-Equilibrium Systems, S. Chen, B. Chu and R. Nossal, Ed. New York : Plenum, 1981, pp. 685-702.

[60] K. Tremper and S. Barker, Pulse Oximetry, Anesthesiology, vol. 70, pp. 98-109, 1989.

[61] A. Ishimaru, Wave propagation and scattering in random media: single scattering and Transport theory, Academic press, New York, 1978.

[62] M. Van Gemert, S. Jacques, H. Sterenborg and W. Star, Skin Optics, IEEE Trans. Biomed. Eng., vol. 36, No. 12, pp. 1146-1154, 1989.

[63] Laser, photonics and electro-optics, edt. A. J. Welch and M. J. C. van Gemert, Plenum Press, New York, 1995.

[64] R. A. J. Groenhuis, H. A. Ferwerda and J. J. Ten Bosch, Scattering and absorption of turbid materials determined from reflection measurements I: theory, App. Opt., vol. 22, No. 16, pp. 2456-2462, 1983.

[65] L. Reynolds, C. Johnson and A. Ishimaru, Diffuse Reflectance from a Finite Blood Medium : Applications to Modeling of Fiber Optic Catheters, Appl. Optics, vol. 15, pp. 2059-2067, 1976.

[66] P. Kubelka and F. Munk, Ein Beitrag zur optik der farbanstriche, Z. Technichse Physik, vol. 12, pp. 593-601, 1931.

[67] P. Kubelka, New contributions to the optics of intensely light scattering materials part I, J. Opt. Soc. Am., vol. 38, pp. 448-457, 1948.

[68] P. Kubelka, New contributions to the optics of intensely light scattering materials part II: non-homogeneous layers, J. Opt. Soc. Am., vol. 44, pp. 330-335, 1954.

[69] S. T. Flock, M. S. Patterson, B. C. Wilson and D. R. Wyman, Monte Carlo modeling of light propagation in highly scattering tissue-I: Model predictions and comparison with diffusion theory, IEEE Trans. Biomed. Eng., vol. 36, pp. 1162-1168, 1989.

[70] H. C van de Hulst, Multiple Light Scattering Tables, Formulas and Applications, New York: Academic, 1980.

[71] I. Miller and A. Veitch, Optical Modeling of Light Distributions in Skin Tissue Following Laser Radiation, Laser Surg. Med., vol. 13, pp. 565-571, 1993.

[72] M. vanGemert, A. Welch, J. Pickering, O. Tan and G. Gijsbers, Wavelengths of Laser Treatment of Port Wine Stains and Telangiectasia, Laser Surg. Med., vol. 16, pp. 147-155, 1995.

[73] D. Smithies and P. Butler, Modeling the Distribution of Laser Light in Port Wine Stains with Monte Carlo Method, Phys. Med. Biol., vol. 40, pp. 701-731, 1995.

[74] G. Lucassen, W. Verkruysse, M. Keijzer and M. vanGemert, Light Distributions in Port Wine Stains Model Containing Multiple Cylindrical and Curved Blood Vessels, Laser Surg. Med., vol. 18, pp. 345-357, 1996.

[75] L. Wang, S. Jacques and L. Zheng, MCML - Monte Carlo Modeling of Light Transport in Multi-layered Tissues, Compu. Metd. And Prog. in Biomed., vol. 47, pp. 131-146, 1995.

[76] S. Prahl, M. Keijzer, S. Jacques and A. Welch, A Monte Carlo Model of Light Propagation in Tissue, Proc. SPIE, vol. 5, pp. 102-111, 1989.

[77] C. Gardner and A. Welch, Monte Carlo Simulation of Light Transport in Tissue: unscattered absorption events, Appl. Opt., vol. 33, pp. 2743-2745, 1994.

[78] T. J. Pfefer, J. K. Barton, M. T. Ducros, T.E. Milner, J. S. Nelson and A. J. Welch, Adaptable three-dimensional Monte Carlo modeling of imaged blood vessels in skin, SPIE Proc., vol. 2975, pp. 2-13, 1997.

[79] W. Snyder, M. Ford, G. Warnerand H. Fisher, Estimates of absorbed fractions for Monoenergetic Photon Sources Uniformly Distributed in Various Organs of a Hetrogeneous Phantom, J. Nucl. Med., pp. 5-52, 1969.

[80] I. Zubal and C. Harrell, Voxel based Monte Carlo Calculations of Nuclear Medicine Images and Applied Variance Reduction Techniques, Inf. Proc. In Med. Ima. Proc., 12th Int. Conf., pp. 23-33, 1991.

[81] S. Jacques, Skin Optics Summary, Oregon Medical Laser Center News, Jan 1998.

[82] J. W. Wang, C. H. Chen, W. M. Chien and C. M. Tsai, Texture classification using non-separable two-dimensional wavelets, Pattern Recognition Letters, vol. 19, pp. 1225-1234, 1998.

[83] R. C. Gonzalez and R. E. Woods, Digital image processing, pp.443-458, Addison-Wesley publishing company, 1992.

[84] L. Henyey and J. Greenstein, Diffuse radiation in the Galaxy, Astrophys. J., vol. 93, pp. 70-83, 1941.

[85] J. Hendricks and T. Booth, MCNP Variance Reduction Overview, Lect. Notes Phys. vol. 240, pp. 83-92, 1985.

[86] L. Carter and E. Cashwell, Particle-Transport Simulation With Monte Carlo Method, USERDA Tech. Info. Center, Oak Ridge, TN, 1975.

[87] M. Born and E. Wolf, Principles of Optics: Electromagnetic Theory of Propagation, Interference and Diffraction of Light, 6th ed., Pergamon Press, 1986.

[88] E. Hecht, Optics, 2nd ed., Addison & Wesley Publishing Company, Inc., 1987.

[89] S. Tokiko and K. Ogawa, New Accelerating Method for Photon Transport in Monte Carlo Simulation, IEEE Trans. Nucl. Sc., vol. 46, No. 6, pp. 2197-2201, 1999.

[90] F. Bolin, L. Preuss, R. Taylor and R. Ference, Refractive Index of Some Mammalian Tissues Using a Fiber Optic Cladding Method, App. Optics, vol. 28, No. 12, pp. 2297-2302, 1989.

[91] H. Zeng, C. MacAulay, D. McLean and B. Palcic, Reconstruction of in Vivo Skin Autofluorescence Spectrum from Microscopic Properties by Monte Carlo Simulation, Photochem. Photobiol., vol. 38, pp. 234-240, 1997.

[92] M. Everett, E. Yeargers, R. Sayre, and R. Olsen, Penetration of Epidermis by Ultraviolet Rays, Photochem. Photobiol., vol. 5, pp. 533-542, 1966.

[93] W. Bruls and J van der Leun, Forward Scattering Propertiec of Human Epidermal Layers, Photochem. Photobiol., vol. 40, pp. 231-242, 1984.

[94] R. Anderson and J. Parrish, Optical Properties of Human Skin, The Science of Photomedicine, J. Regan and J. Parrish Ed., New York: Plenum, 1982, pp. 147-194.

[95] S. Jacques, C. Alter and S. Prahl, Angular Dependence of He-Ne Laser Light Scattering by Human Dermis, Laser Life Sci., vol. 1, pp. 309-333, 1987.

[96] W. Cui, L. Ostrander and B. Lee, In Vivo Reflectance of Blood and Tissue as a Function of Light Wavelength, IEEE Trans. Biomed. Eng., vol. 37, No. 6, pp. 632-639, 1990.

[97] H. Zeng, C. MacAulay, D. McLean and B. Palcic, Spectroscopic and Microscopic Characteristics of Human Skin Autofluorescence Emission, Photochem. Photobiol., vol. 61, No. 6, pp. 639-645, 1995.

[98] H. Zeng, C. MacAulay, B. Palcic and D. McLean, A Computerized Autofluorescence and Diffuse Reflectance Spectroanalyser System for in Vivo Skin Studies, Phys. Med. Biol., vol. 38, pp. 231-240, 1993.

[99] S. L. Jacques and S. A. Prahl, Collection by an optical fiber, Oregon Graduate Instititute, http://omlc.ogi.edu/classroom/ece532/class1/collect_fiber.html, 1998.

[100] Alberto Leon-Garcia, Probability and random processes for electrical engineering, 2nd ed., Addison-Wesley Publishing Company, Inc., pp. 233-234, 1994.

[101] A. R. van Erkel and P. M. Th. Pattynama, Receiver operating characteristic (ROC) analysis: Basic principles and applications in radiology, European Journal of Radiology, vol. 27, pp. 88-94, 1998.

[102] R. P. Lippmann, An introduction to computing with neural nets, IEEE ASSP Magazine, pp. 4-22, April 1987.

[103] B. Widrow and M. A. Lehr, 30 years of adaptive neural networks: Perceptron, Madaline, and backpropagation, Proc. IEEE, vol. 78, No. 9, pp. 1415-1442, Sept. 1990.

[104] Shuangshuang Dai and Atam P. Dhawan, PC-based Fuzzy Classification of Turbine Blade Damage, 40th AIAA/ASME/SEE/ASEE Joint Conference, Florida, 2004, submitted.